MAGNETOELECTRIC EFFECT IN FERROELECTRIC-FERROMAGNETIC HETEROSTRUCTURES

Zhiguang Wang

Dissertation submitted to the faculty of the
Virginia Polytechnic Institute and State University
in partial fulfillment of the requirements for the degree of

Doctor of Philosophy

In

Materials Science and Engineering

April 23, 2014

Blacksburg, VA 24061

Dwight D. Viehland, Chair

Jie-Fang Li

Alex O. Aning

Louis J. Guido

Keywords: Multiferroic, ferroelectric, ferromagnetic, piezoelectric, magnetostrictive, self-assemble, epitaxial, thin film, magnetic force microscopy

The Magnetoelectric Effect

in Ferroelectric-Ferromagnetic Heterostructures

ZhiguangWang

ABSTRACT

The magnetoelectric (ME) effect, a coupling effect between magnetic and electric orders, has been widely investigated, both from a fundamental science perspective and an applications point of view. Magnetoelectric composites with one piezoelectric phase and one magnetostrictive phase can be magneto-electrically coupled via elastic strain mediation. Bulk magnetoelectric composites have been intensively studied as magnetic sensors due their significant magnetic-to-electric signal transforming efficiency, which promises high magnetic field sensitivity. In contrast, electric field-controlled magnetization in magnetoelectric thin films is more attractive for information recording and novel electrically-tunable microwave magnetic devices.

For the present work, we prepared a series of magnetoelectric structures capable of modulating the magnetization with an electric field—all of which display unprecedented magnetic coercive field tunability. These structures show promise for a number of applications, including magnetic memory and spintronics. First, we generated self-assembled $BiFeO_3$-$CoFe_2O_4$ (BFO-CFO) nanostructures of varying architectural structures on differently-oriented perovskite substrates. We were able to control aspect ratio through both thickness control and by manipulating growth thermodynamics. The relationship between magnetic shape and strain anisotropy was systematically analyzed using both in-plane and out-of-plane magnetic easy axis data.

The BFO-CFO self-assembled structures may be useful for applications, including longitudinal and perpendicular magnetic memory; additionally they can serve as a prototype for analyzing the magnetoelectric effect-based magnetoresistive random-access memory. BFO-CFO grown on piezoelectric $Pb(Mg,Nb)O_3$-$PbTiO_3$ (PMN-PT) shows a large magnetoelectric coupling coeffcient.

Second, we sought to clarify the relationship between ferroelectric/ferroelastic phase transformation and the magnetoelectric effect in CFO films on PMN-PT heterostructures. Elastic strain is an essential component of electro-mechanical-magnetic coupling. Most prior studies that used piezoelectric materials as a strain source assumed that these materials shared a linear relationship (d_{31} or d_{33}) with the electric field, which is true only with small electric field signals. In contrast, the largest strain is produced during phase transformation in piezoelectric single crystals. In this work, we systematically investigated electric field induced phase transformation in PMN-PT single crystals with different compositions. A signficant finding that emerged from this study is that a large in-plane uniaxial strain can be controlled by an electric field, and this strain can be used to control the magnetic easy axis distribution in the in-plane. The electric field is along the out-of-plane direction, which is perpendicular to the uniaxial strain and the surface of the sample, and thus can be easily incorporated into real device design.

Finally, we identified very large magnetic coercive field tunability in the CFO/PMN-PT monolithic structures—in fact, more than ten times larger than previously reported magnetoelectric heterostructures. We used a <011> oriented PMN-PT substrate, where a large uniaxial strain can be induced by an electric field. Importantly, since the two in-plane directions have the same dimensions, the uniaxial strain can induce a significant magnetic anisotropy distribution change in the two

in-plane directions. A unprecedented magnetic coercive field change of up to 580 Oe has been observed, which shows great potential for applications in both magnetic memory and microwave magnetic devices.

DEDICATION

To my parents, grandmother and sisters

ACKNOWLEDGEMENTS

I would like to express my sincere appreciation and gratitude to my advisor, Professor Dwight D. Viehland for giving me the opportunity to work on this exciting project. I would like to thank him for his constant support, guidance and encouragement throughout my Ph.D. research. I have tremendous respect for Dr. Viehland's professional knowledge and research passion. I especially benefited from his "Structure Properties Materials" class, and especially our interesting discussions, his intelligent suggestions on my research, his patience on correcting my papers, and his valuable instruction on my presentations. His limitless enthusiasm and dedication to his research has influenced me greatly and will be very helpful in my future career.

Equally important, Professor Jiefang Li has given me great help and guidance in all the projects I have worked on during my Ph.D. research. Her insightful suggestions helped to expand my research and were essential for my experimental setup. I definitely would not have been successful in my doctoral studies without her help.

I would also like to thank my committee members, Professor Alex O. Aning and Professor Louis J. Guido, for their suggestions, support and inspiration.

I extend my thanks to Dr. Li Yan and Dr. Yaodong Yang, Dr. Jaydip Das and Dr. Ravindranath Viswan. Their generosity in sharing their knowledge and valuable experiences with the pulsed laser deposition technique and the preparation of epitaxial thin films made my research so much easier.

I am grateful to Dr. Haosu Luo from the Shanghai Institute of Ceramics for providing excellent piezoelectric single crystals—without his contributions this research would not have been impossible. He also provided valuable advice about paper writing.

I would like to thank both Dr. Yaojin Wang for his creative ideas about piezoelectric single crystals and magnetoelectric composites, as well as Dr. Wenwei Ge, whose impressive knowledge about the piezoelectric single crystals also contributed greatly to this enjoyable collaboration.

I would like to thank Dr. Jianjun Yao who freely shared his amazing knowledge of scanning probe microscopy. We came to Blacksburg together and through his focus on piezoelectric single crystals, he soon became a master of scanning probe microscopy. Dr. Yao was instrumental in helping me determine piezoelectric coefficient measurements and ferroelectric domain mapping. Without his input, it would have been very difficult for me to finish.

I would like to thank Yanxi Li and Yue Zhang for their great discussions of magnetoelectric materials and applications. I will always have wonderful memories of working with them.

I would also like to thank Dr. Junqi Gao, Ying Shen, Menghui Li and Chengtao Luo—all members of Dr. Viehland's research group. Through their own expertise in different research areas they helped to advance my research experience in significant ways.

I would also like to acknowledge Professor Vincent Harris and Bolin Hu at Northeastern University for their great help with the essential measurements for this study.

Finally, in addition to extending my gratitude to all my friends here in the U.S. who have made my stay here so enjoyable and memorable, I would above all like to express my deepest thanks to my wonderful family. I have to thank my grandmother (Zhang Da-Ping) and my parents (Wang Jin-Ping and Wang Shu-Jin) for their unconditional love and endless support over the years. I want to thank my sisters for such a joyful life we have shared together. I would never have achieved this milestone without their unwavering belief and support.

TABLE OF CONTENTS

LIST OF TABLES

LIST OF FIGURES

Chapter 1 INTRODUCTION

1.1 Multiferroics and the magnetoelectric effect

Multiferroics are defined as materials that exhibit more than one primary ferroic order parameter simultaneously (i.e. ferromagnetism, ferroelectricity, ferroelasticity, etc.).[1] Coupling between different ferroic orders has enabled the tunability of various electric and magnetic parameters—the most interesting of which is the coupling between ferroelectricity and ferromagnetism, known as the magnetoelectric (ME) effect.[2-7] A ferroelectric material exhibits dielectric polarization even in the absence of an external electric field, and the direction of the spontaneous polarization can be reversed by an external electric field. Conversely, ferromagnetism is a phenomenon by which a material exhibits spontaneous magnetization that can be switched by an external magnetic field. Ferroelasticity refers to a spontaneous deformation in response to an applied stress, as shown in Fig.1.1. The combination of ferroelectricity and ferroelasticity is known as *piezoelectricity,* which is important for a wide range of applications in transducers, actuators and sensors, and other automotive devices. Also important to note is that the coupling between ferromagnetism and ferroelasticity results in magnetostriction and the consequent application of piezomagnets as magneto-mechanical actuators.

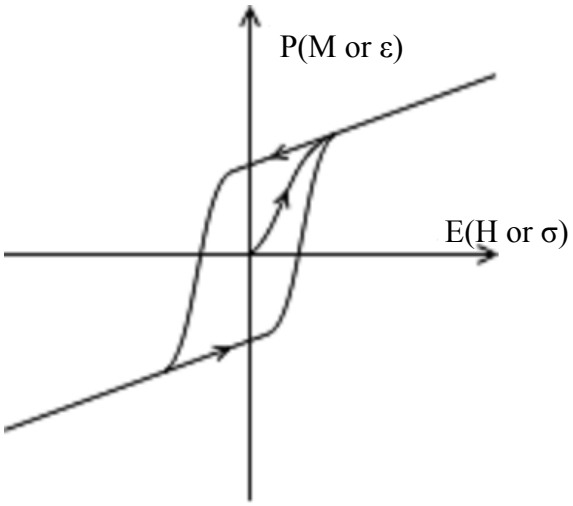

Figure 1.1. Switchable electric polarization P, magnetization M and strain ε under the external electric (E), magnetic (H) fields and stress σ in ferroelectric, ferromagnetic and ferroelastic materials, respectively.

ME materials exhibit either induced polarization under an external magnetic field, or induced magnetization under an external electric field, as shown in Fig.1.2. The concept of the ME effect was originally proposed by P. Curie[2] in 1894. In 1959, Dzyaloshinskii[3] predicted the existence of single phase ME substances that simultaneously have electric and magnetic dipole moments. He also pointed out that an electric field may induce both electric polarization and magnetization at the same time. The ME effect was first experimentally observed by Astrov[8] in an unoriented Cr_2O_3 crystal in 1960. Shortly thereafter, electric field-induced magnetization (i.e. the converse ME effect) in Cr_2O_3 was reported by Rado and Folen[7] in 1961. After an initial burst of interest, however, research in this area remained static for over 40 years. This changed in 2003 with the discovery of large ferroelectric polarization in epitaxially-grown $BiFeO_3$ thin films, as well as the discovery of strong magnetic and electric coupling in orthorhombic $TbMnO_3$ and $TbMn_2O_5$—both of which re-stimulated activity in the magnetoelectric effect.[5, 6]

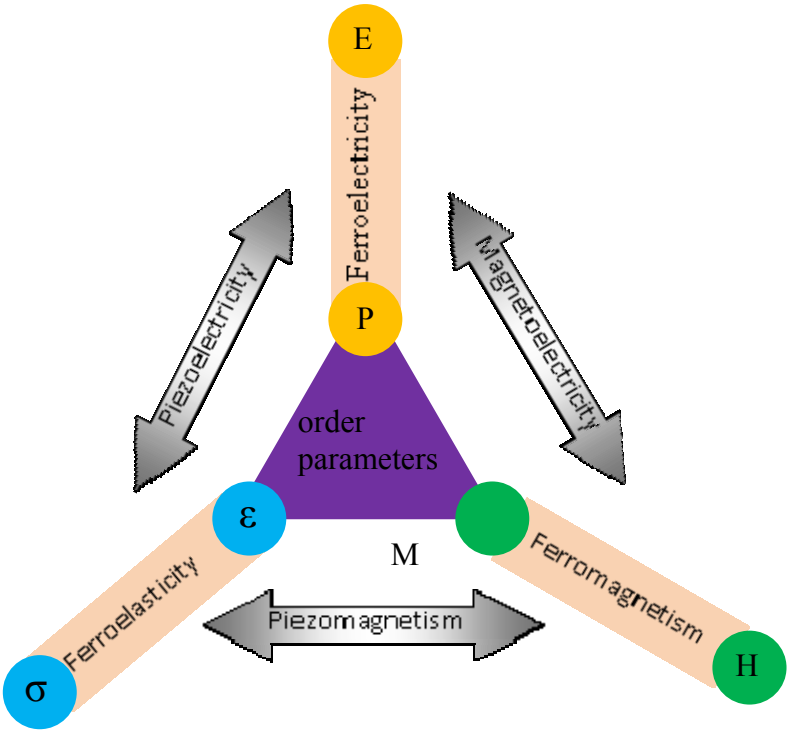

Figure 1.2. Coupling of ferroic orders in multiferroics. External electric field *E*, magnetic field *H*, and stress *σ* can control the electric polarization *P*, magnetization *M* and strain *ε*, respectively. The coupling between *P* and *M* results in magnetoelectricity.

1.2 Single phase magnetoelectric materials

The possible coexistence of spontaneous magnetization and polarization in single phase ME materials does not necessarily contradict the general criteria for the emergence of ferromagnetism and ferroelectricity taken separately: magnetic ordering is governed by the exchange interaction of the electron spins, while ferroelectric ordering is governed by the redistribution of charge density in the lattice.[4, 9] However, no material featuring the coexistence of strong ferroelectricity and ferromagnetism has been found in nature or synthesized in the laboratory. The fundamental physics behind the scarcity of single phase ME materials have been explored by Nicola A. Hill and C.

Ederer. In separate reports, these researchers found that, in general, the d electrons in transition metals, which are essential for magnetism, reduce the tendency for off-center ferroelectric distortion,[4, 9] as shown in Fig.1.3. Consequently, an additional electronic or structural driving force must be present for ferromagnetism and ferroelectricity to occur.

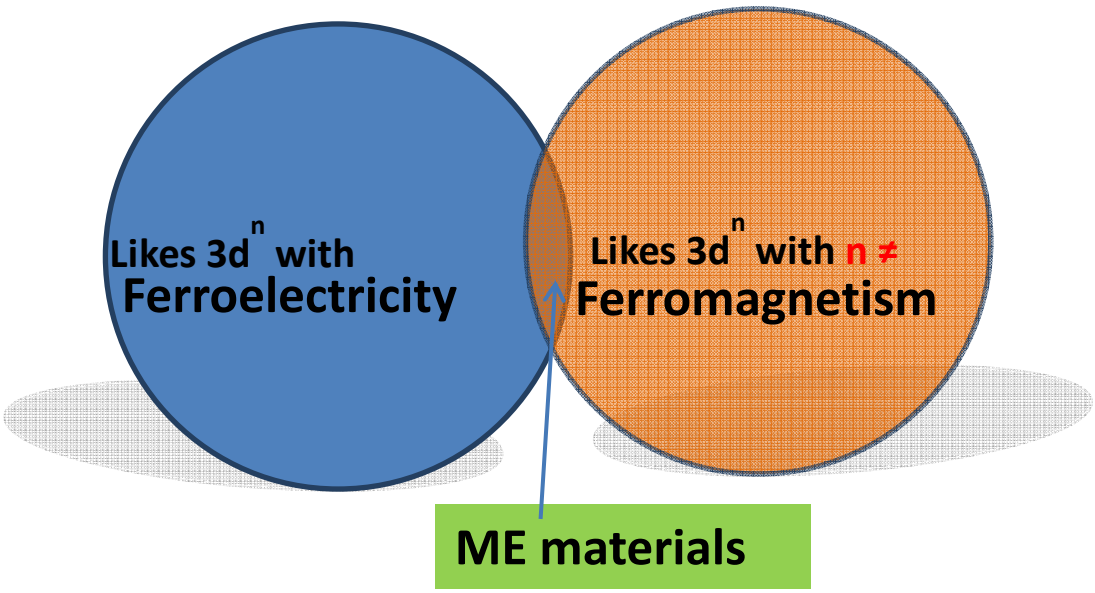

Figure 1.3. Electron configuration dilemma between the one favors ferroelectricity and the one favors ferromagnetism.

The first reported single-phase ME material was Cr2O3, which has a linear ME effect. Since then, many other single-phase ME material families have been described. However, the ME coupling of a single-phase material is very weak; moreover, the ME effect in most single-phase ME materials only exists at very low temperatures.[10, 11] Researchers have also reported that some can only be detected at extremely high magnetic fields of >20 Tesla (e.g., $BiFeO_3$[12]), while others can only be detected as a minute change in the dielectric constant at the Neel temperature or, correspondingly, as a small change in the magnetic permeability at the Curie temperature, such as $RMnO_3$[13] and $Pb(Fe_{1/2}Nb_{1/2})O_3$.[14] In short, no single-phase

material has yet been found that has a measurable ME coefficient at room temperature and at low magnetic field. The largest ME coefficient previously reported at either low temperature or high H was on the order of 10mV/cm-Oe., which is too small to be of practical use in devices. Prior studies were done primarily for scientific curiosity. Table 1.1 lists some of the single-phase ME materials.

Table 1.1. Single-phase ME materials with different crystal structures

Crystal structure	Compound formula
Perovskite	$BiFe_3$, $TbMnO_3$
Hexagonal	$RMnO_3$; R = Sc, Y, Ho-Lu
Boracites	$M_3B_3O_{13}X$; M = Cr, Mn, Fe ...; X = Cl, Br, I
Orthorhombic	$BaMF_4$; M = Mg, Mn, Fe, Co, Ni, Zn

1.3 Magnetoelectric effect in composite materials

To overcome the principal disadvantage of single-phase ME materials—namely that electron configurations that favor ferroelectricity are antagonistic to those that favor ferroelectricity—researchers have continued to investigate various ME composites. These materials consist of a ferroelectric phase (piezoelectric) and a ferromagnetic phase (magnetostrictive). Electric polarization and magnetization can couple through the interface strain between two different phases that responds to electric and magnetic fields, respectively. The piezoelectric effect is defined as the linear electromechanical interaction between the mechanical and the

electrical state in crystalline materials with no inversion symmetry. Meanwhile, magnetostriction is a property of a ferromagnetic material that causes it to change its shape or dimension during the process of magnetization. In ME composites, a magnetic field induces a distortion of the magnetostrictive phase; this, in turn, distorts the piezoelectric phase, which is where an electric field is generated (Fig.1.4). The composite is then considered to be a new material with multiferroic properties. Such physical properties are also known as "product properties," which refers to an effect in one of the phases or submaterials that then leads to a second effect in the subsequent phase. Linear ME coupling can be explained by the following equation:

$$P_i = \alpha_{ij} H_j$$
$$M_i = \alpha_{ij} E_j$$

where α_{ij} is the ME coupling coefficient.[15]

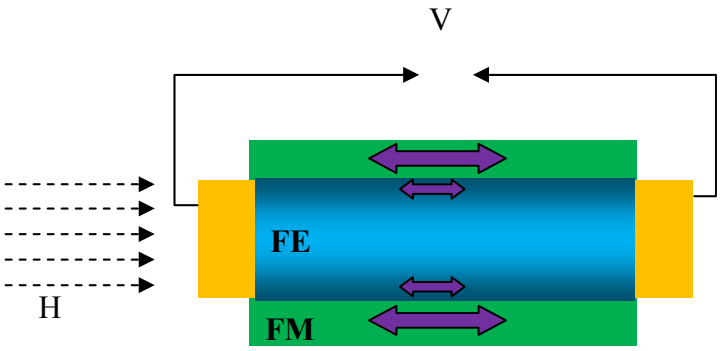

Figure 1.4. Magnetoelectric effect in ferroelectric and ferromagnetic composites: magnetic field-induced strain in a magnetostrictive component is transferred to the piezoelectric part, which then shows a voltage output.

1.3.1 Magnetoelectric effect in bulk materials

Since 2000, a sizeable ME effect has been achieved in ME bulk composite materials. In particular, laminate structures have proven to be the most successful design for obtaining accurate ME effect measurements[15]. There are two kinds of laminate ME structures based on the composition of the ferroelectric and ferromagnetic phases: all-ceramic ME laminated composites and ceramic/alloy ME composites.

All-ceramic ME structures can be achieved utilizing traditional fabrication technologies. An interface displaying good integrity between the piezoelectric and magnetostrictive phases can be ensured via the high temperature co-fire of the two-phase components. Srinivasan et al. published a study of bi- and multilayer composites of $Pb(Zr,Ti)O_3$ (PZT) and $NiFe_2O_4$ (NFO) thick films fabricated by tape casting, wherein a large ME coupling coefficient of α_{ME}=460 mV/cm-Oe was reported.[16]

Although ferrite/PZT laminates have shown considerable ME voltage coefficients, the limited magnetostriction of the ferrite phase has proven to be a bottleneck to developing composites with larger ME effects. Iron-based alloys with significant piezomagnetic coefficients, e.g. Terfenol-D, Fe-Ga and Metglas, have become an important solution to this bottleneck, thereby enabling the achievement of further enhancements in α_{ME}[17-20]. A thin layer of epoxy was used to bond the alloy and PZT together, since high temperature sintering will destroy the magnetic properties of alloys. Investigations of the ME voltage coefficient of Terfenol-D/PZT laminates have indicated a sizable ME coupling coefficient of α_{ME}= 4.6 V/cm-Oe, which is nearly an order of magnitude higher than the corresponding figure for ferrite / PZT laminates.

1.3.2 Magnetoelectric effect in thin-film structures

Composite thin-film multiferroic materials can generally be divided into three types: (i) a 0-3 structure, which is typically a magnetostrictive material embedded in a piezoelectric matrix (i.e., $CoFe_2O_4$ (CFO) nanoparticles in PZT matrix); (ii) a 2-2 structure, which is typically a multilayer thin film of magnetostrictive and piezoelectric materials; and (iii) a 1-3 structure, such as monolayer self-assembled nanostructures (i.e., CFO nanopillars in a $BiFeO_3$ (BFO) matrix). ME composites with a 0-3 phase interconnectivity have been fabricated by both sol-gel[21-23] and pulsed laser deposition (PLD).[24] Sol–gel is suitable for thicker film deposition, whereas PLD facilitates the generation of thin films with better quality. CFO or NFO are often used in the magnetostrictive phase in ME composites due to their high magnetoelastic coefficients, while PZT is utilized for the piezoelectric phase because of its high piezoelectric coefficient. Ren and Wuttig[25] modified this method using sol–gel to deposit CFO/Fe_3O_4 nanoparticles on $Pb(Mg_{1/3}Nb_{2/3})O_3$–$PbTiO_3$ (PMN-PT) single-crystal substrates, which served both as substrate and strain mediator. The ME coupling coefficient was measured, which was not found to be particularly high compared to bulk co-fired layered composites due to interaction between the two composite layers and the substrate (i.e., clamping). ME composites of a 2-2 or multilayer interconnectivity of ferroelectric and piezoelectric phases have been deposited heteroepitaxially as thin layers on single-crystal substrates by PLD[26-30] and sol–gel.[31, 32] The advantages of this 2-2 connectivity is that it is easy to manipulate and has great application potential—but again, substrate clamping effects present problems that must be overcome to achieve enhanced ME coupling coefficients. A number of studies have investigated the development of a high-resistance piezoelectric layer and subsequent integration with Si. Finally, as described by Zheng et al.,

research has focused on multiferroic monolayered self-assembled nanostructures.[33] These researchers deposited differently shaped BFO–CFO nanostructures on variously oriented $SrTiO_3$ (STO) substrates,[34] and successfully realized magnetization switching under electric field assistance.[35, 36] Similarly, Levin et al.[37, 38] also employed similar nanostructures in both theoretical and experimental studies to confirm that the epitaxial growth of two immiscible phases on a single-crystal substrate can occur due to elastic strain interaction between the two phases, which determines their growth dynamics and final morphology. Monolayer self-assembled structures are believed to have good interactions between the two constituent phases, thus enhancing the ME effect. In particular, vertically-aligned structures are credited with overcoming substrate clamping effects.

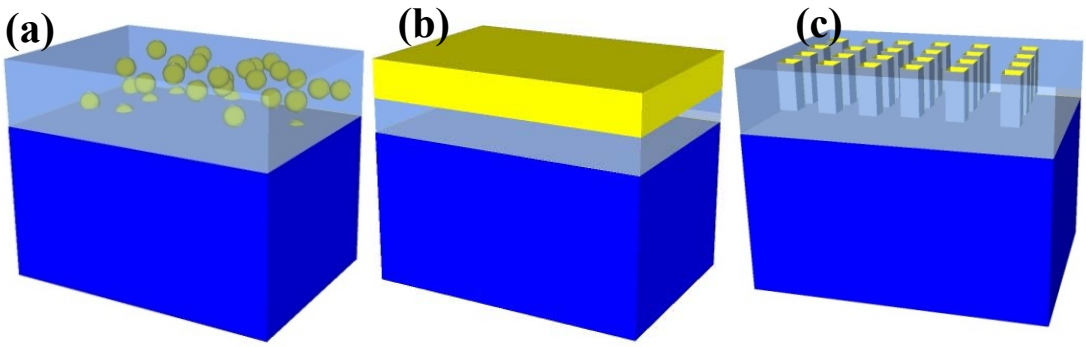

Figure 1.5. Thin film ME structures with three different connectivity: (a) 0-3, (b) 2-2, and (c) 1-3.

1.4 Converse magnetoelectric effect in thin films

ME coupling between magnetic and electrical properties has intriguing potential for a variety of applications. The two most promising ones are magnetic-field sensors that could replace low-temperature superconducting quantum interference devices, and electric-write/magnetic-read memory devices that combine the best of

ferroelectric and magnetic random-access memory. The former application requires a significant accumulation of magnetically-induced electrical charge that is proportional to the size of the structure. Thus, magnetic sensors based on bulk ME materials shows much higher sensitivity compared with ones based on thin films. The latter application requires electrically controllable magnetization, which is more difficult to achieve and rarely studied due to the more complex characterization methods for magnetic signals in comparison to methods used to characterize electrical signals. This change of magnetization due to an applied electric field is defined as the converse ME effect.

1.4.1 Converse magnetoelectric in single-phase materials

Most single-phase multiferroics—e.g., BFO and $YMnO_3$ (YMO)—exhibit antiferromagnetism and ferroelectricity at room temperature. It is well established that the antiferromagnetic easy axis plane in BFO is perpendicular to the electric polarization direction. Thus, it is possible to control the electron spin direction with an electric field. In fact, researchers proposed a new concept involving magnetoelectric random access memory (MERAM) in single-phase multiferroic $BiFeO_3$, where an electric field assistance of 180° magnetization switching was assumed.[39] Ferroelectric polarization and magnetic polarization are used to encode binary information in ferroelectric random access memory (FeRAM) and magnetic random access memory (MRAM), which enable four-state logic in a single device. Electrical control of magnetization via ME coupling offers an opportunity to take advantage of FeRAM and MRAM in the form of nonvolatile magnetic storage that is switched by an electrical field.

MERAM is comprised of a magnetic tunnel junction (MTJ) grown on a multiferroic layer featuring antiferromagnetic order. E-field control of antiferromagnetism in multiferroic layers can switch the magnetic order by 180° in the

bottom ferromagnetic layer through interfacial exchange coupling. The data is then read by the resistance measurement in the MTJ. In this way, nonvolatile memory is realized by combining ME coupling in single-phase multiferroics and interfacial exchange coupling between ferromagnetic and multiferroic materials. In fact, 180° magnetization switching is not only critical for MERAMs, but also of great fundamental importance in spintronic devices. Integrating ME effect with spintronics can enable the development of novel tunable spintronic devices.

The electric field-controlled magnetization switch is the most important procedure in the writing process for memory devices. However, controlling antiferromagnetism in single-phase multiferroics is challenging due to the complex interactions between the magnetic order and the electric order in multiferroics. In fact, only a few studies have been reported in this area. The Ramesh Group at UC Berkeley achieved electric control of the antiferromagnetic domain in single-phase multiferroic BiFeO3; specifically, the researchers discovered that exchange coupling mediated one-to-one mapping of the ferroelectric and ferromagnetic domains to manifest electrical control of magnetism in $Co_{0.9}Fe_{0.1}/BiFeO_3$.[39] A similar electric field-controlled antiferromagnetism and exchange bias effect was also reported in LSMO/BFO bilayers at 7K by the same group[40]. A few years earlier, Laukhin et al.[41] demonstrated successful electric field control of the antiferromagnetic order in the YMO phase, and subsequent bias of the ferromagnetic Py top layer, through an exchange bias effect at very low temperatures (5 to 20K). So far, the E-field control of antiferromagnetism in single-phase multiferroics exhibits weak tunability and low working-temperature requirements, which puts serious limitations on its potential for industrial applications.

1.4.2 Converse magnetoelectric in composite materials

The converse ME effect is very weak in single-phase ME materials: $\alpha = \Delta M/E \approx 4.1\times10^{-12}$ s m^{-1} in Cr_2O_3 near the Neel temperature of 307 K. ME composite structures provide more freedom in control of magnetization through strain from the piezoelectric phase. Single-crystal piezoelectric materials show significant reversible strain under external an electric field during the electrical polarization switching process, as shown in Fig.1.5(a). In order to apply a large strain in the magnetic phase, single-crystal piezoelectric substrates have been used for the growth of epitaxial magnetostrictive thin films on top to form monolithic ME structures, as shown in Fig.1.5(b). During the electrical polarization switching process, the piezoelectric single-crystal unit cell will experience a reversible strain due to the movement of the B site atoms in the perovskite ABO_3 structures. Then, this strain is transferred to the epitaxial ferromagnetic thin film where a magnetic strain anisotropy-controlled magnetic easy axis rotation will occur. Hu et al.[42] used the phase-field method to study the effect of a biaxial in-plane strain both magnetization switching and magnetic domain structures in epitaxial CFO films. The researchers concluded that magnetic domains can be switched from an initial in-plane to an out-of-plane direction under isotropic in-plane elastic strains. Abrupt magnetization switching has been observed for single-domain CFO films, in contrast to gradual magnetization switching for multi-domain CFO films. Eerenstein et al.[43] deposited epitaxial $La_{0.67}Sr_{0.33}MnO_3$ (LSMO) (40nm) thin films on BTO (0.5mm) single-crystal substrates and measured the magnetization as a function of temperature and electrical field. In the temperature range where magnetization was present, a step magnetization jump was observed at 200K, which coincided with a rhombohedral-to-orthorhombic phase transition. Another magnetization change inflection point occurred around 340K, when the BTO

substrate experienced depolarization during the ferroelectric tetragonal phase. The large change in the lattice constant during phase transition induced a sizeable strain in the upper ferromagnetic phase—the result of which was a dramatic magnetization change due to strain-induced magnetic anisotropy. Sharp and persistent magnetization change was also detected after applying an electric field of 10 kV/cm at room temperature. A ferroelectric domain rotation from the in-plane direction to the out-of-plane direction was confirmed by X-ray diffraction results. This domain rotation process will also apply a large strain in epitaxial LSMO thin films. A converse ME coupling coefficient of $\alpha = 2.3\times10^{-7}$ s m^{-1}, which is almost 50,000 times greater than in single-phase ME materials, was observed.

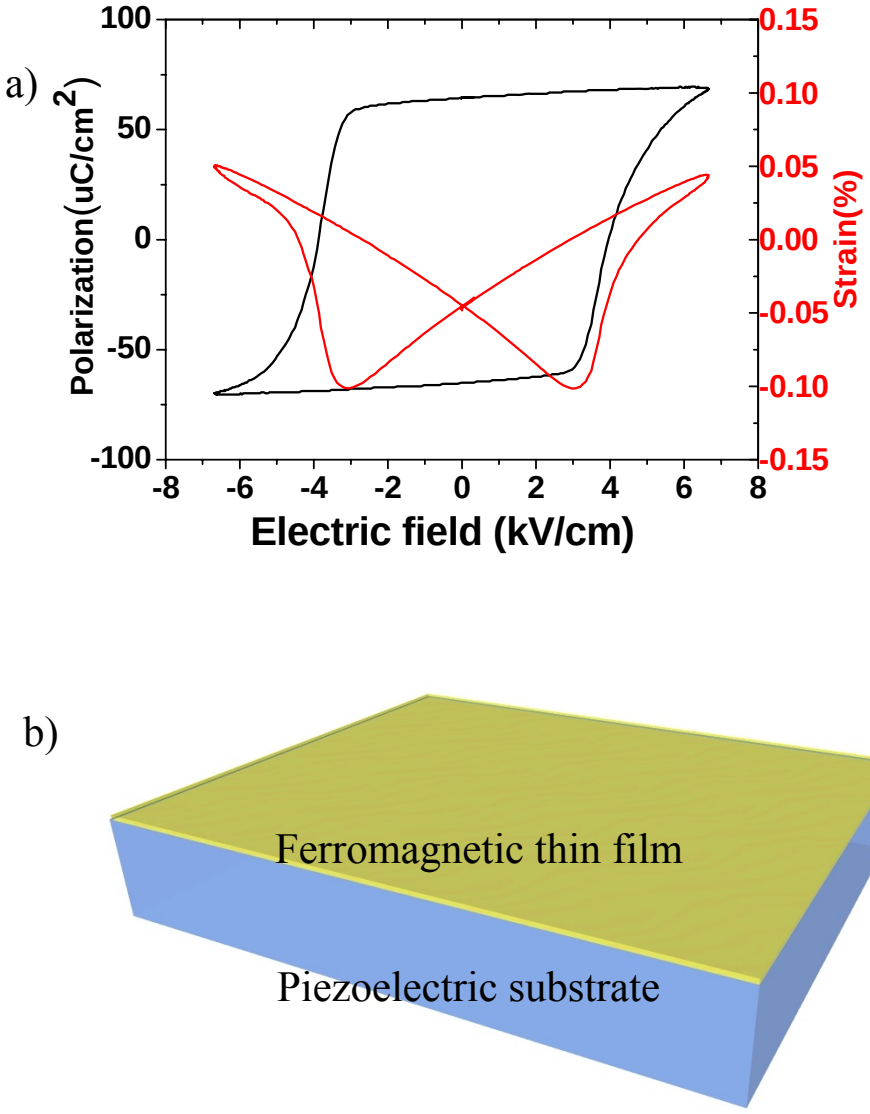

Figure 1.6. (a) Typical electrical polarization hysteresis loop as a function of external electric field in piezoelectric single-crystal (black curve) and corresponding strain hysteresis loop as a function of electric field in the same single-crystal piezoelectric substrate (red curve). (b) Schematic of epitaxial ferromagnetic thin film on single-crystal piezoelectric substrates.

Apart from the 2-2 type of ferrite/ferroelectric laminate structures, the 1-3 type of magnetic nanopillars embedded in ferroelectric matrix ME composite structures show a large converse ME effect. Zavaliche et al.[35] investigated 1-3 type CFO nanorods embedded in a BFO matrix 3-dimensional ME structure. A magnetic hysteresis loop was changed with electric poling of a part of the sample area, indicating an electric field-induced large magnetic anisotropy field. Researchers theoretically predicted that the 1-3 type of multiferroic heterostructures would deliver strong ME coupling due to a large interfacial area.[44] However, because the resistivity of the magnetic phase is typically smaller than that of ferroelectric phase, a large current leakage would be expected in applying an electric field on a 1-3 type or other nano-mixed composite multiferroic. Thus, the ferroelectric phase could not be poled and charged completely, making strong ME coupling hard to achieve in practice. Zavaliche also studied reversible magnetization in each CFO nano-rod by applying an electric field using a piezoelectric force microscopy (PFM) tip,[35] as shown in Fig.1.6. It is possible to pole a specific area in a BFO-CFO thin film due to the small size of the PFM tip (i.e., usually smaller than 40 nm). Through a scanning process, an electrical field is applied to the trace area. Therefore, the BFO component will switch its electrical polarization to be along the electric field direction. Subsequently, a the strain produced via the polarization switching process will then be transferred to the CFO nanorods. Magnetic force microscopy (MFM) was used to characterize the change in magnetic response for each CFO nanorod. A distinct difference in MFM images was observed in the poled and unpoled areas, demonstrating successful control of the magnetization through electric field application. Such strain-induced domain switching and magnetic easy axis rotation in magnetic thin films can facilitate electric

voltage-control of magnetization in artificial magnetic/ferroelectric multiferroic heterostructures through piezoelectrically controlled strains.

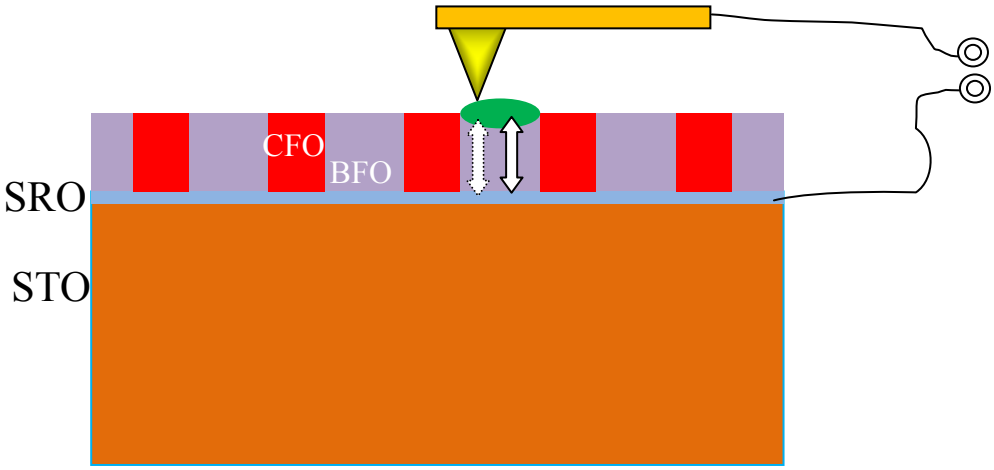

Figure 1.7. Converse ME effect in BFO-CFO 3D thin films: an electric field was applied between the SRO bottom electrode and the PFM tip as the top electrode to switch the electrical polarization in BFO ferroelectric components. The induced strain is then transferred to the CFO nanorods.

1.5 Self-assembled structures with enhanced properties and product multifunctionality

When Nobel laureate Herbert Kroemer coined the famous phrase that "the interface is the device," he was referring to the then astonishing success of devices based on thin semiconductor films for photonic and electronic applications that started more than 40 years ago. Since that time, however, complex oxides exhibit various functional properties far exceeding those of the semiconductors that are ubiquitous in our electronic world. Specifically, they out-perform the latter in areas of multiferroicity, high-temperature superconductivity, room-temperature magnetic semi-conductivity, colossal magnetoresistance, ferroelectricity, and ferromagnetism. The recent discovery of an even richer spectrum of possibilities for complex

oxides—namely unexpected interface effects—translates to even greater potential for field applications. As reported in the literature,[45-48] these interesting advantages include interface-induced high temperature superconductivity, hugely enhanced polarization at interfaces, enhanced interface magnetism, and large carrier concentrations at room temperature in 2D interface electron gases. These findings have opened up a whole new field of condensed matter physics with an amazing variety of potential applications.

Conventional interfacial structures appear as heteroepitaxial multilayers. For example, both $LaAlO_3$ and $SrTiO_3$ are electrical insulators; however, if one produces LAO thin films on TiO_2-terminated STO thin films, they form a highly-conducting, two-dimensional electron gas (2DEG) at their interface.[48] A more interesting interface exists in vertically aligned, self-assembled heteroepitaxial structures. Such 3D structures have powerful advantages over conventional multilayer structures—principally in aspects of interfacial area and large thickness strain applications. In a conventional multilayer, the interfacial area is fixed by the area of the specific sample. In contrast, in a vertically-aligned heterostructure, the interfacial area is related to the feature size of the separated phases, and can be tuned by manipulating thermodynamic parameters (temperature, composition, and bond energies). These features mean that it is possible to control the overall energy of a system in order to create desired structures with much larger interfacial area.

1.5.1 Spinodal decomposition

Spinodal decomposition is a mechanism by which a solution of two or more components can separate into distinct regions (or phases) with distinctly different chemical compositions and physical properties. This mechanism differs from classical nucleation in that phase separation due to spinodal decomposition is much more subtle,

and occurs uniformly throughout the material—i.e., not just at discrete nucleation sites.

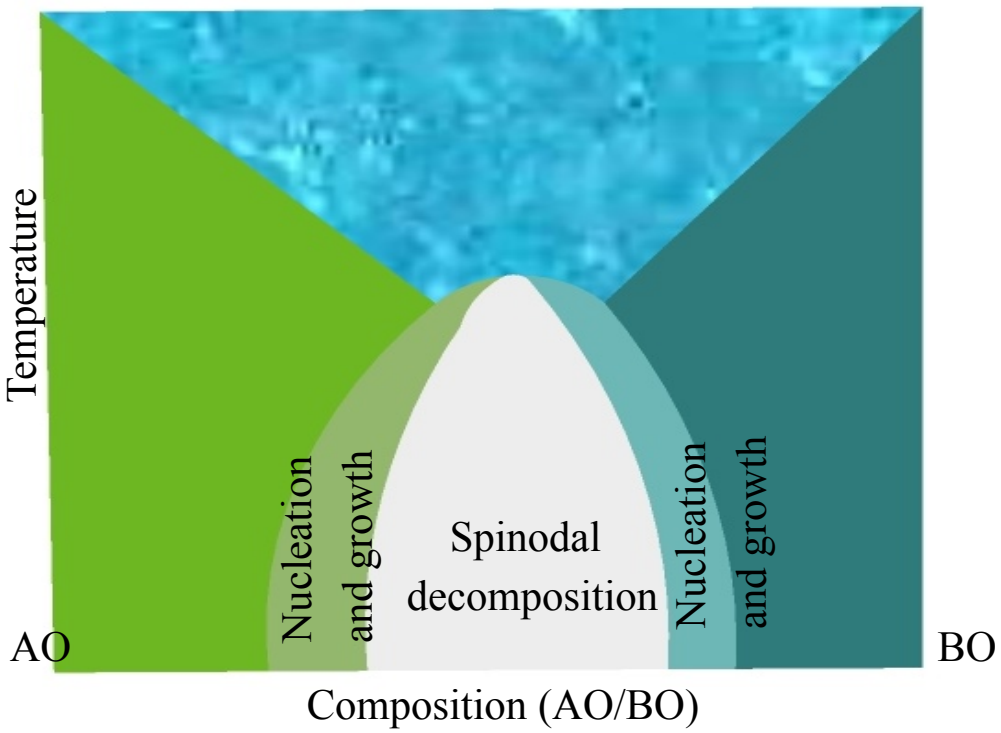

Figure 1.8. Spinodal decomposition mechanism and nucleation and growth regions formed for two different phases (AO and BO) with large miscibility at high temperature and immiscibility at low temperature.

The crucial challenge for growing self-assembled thin films is the search for functional oxides with moderate crystal lattice mismatch with each other and large immiscibility at low temperature. The compound, perovskite-spinel, is capable of forming self-assembled heteroepitaxial thin films. For example, BFO-CFO has been grown on differently-oriented STO substrates featuring different phase architectures, as shown in Figure 1.8(a). By carefully selecting materials with proper crystal lattice, it is possible to grow the highly periodic checkerboard structure, which is the optimal crystal lattice configuration, as described in the following equation:

$$\rho = \frac{2a_c + c_t + a_t}{4a_s} \to 1,$$

where a_c is the a axis constant for the thin film cubic phase, a_t and c_t are the a-axis and c-axis lattice constants for the thin film tetragonal phase, and a_s is the substrate a-axis constant for the substrate cubic phase. Successful checkerboard structures have been achieved in $ZnMnGaO_4$ (ZMGO) with periodic Mn-rich and Mn-poor regions and BFO-SmO composite thin films with separated BFO and SmO phases.[49, 50]

Since BFO is ferroelectric with a large piezoelectric constant, and CFO is ferromagnetic with large magnostriction, self-assembled BFO-CFO thin films are widely studied for their ME coupling effects. The use of BFO-SmO has proven to be effective in reducing the leakage problem associated with pure BFO thin films; additionally, a much larger dielectric constant can be achieved using BFO-SmO checkerboard thin films.

In summary, utilizing interfacial effects in thin films is a simple and effective way to tune the properties of complex oxides. Unfortunately, strain relaxation is a serious problem once thickness levels exceed tens of nanometers. Deposition of a multilayer structure can result in a larger strain in heterostructures, but it can also make the growth process more complex and difficult. In response, the incorporation of vertically-aligned, self-assembled heteroepitaxial structures provides more freedom to effectively tune properties due to controllable interfacial area through growth thermal dynamic engineering.

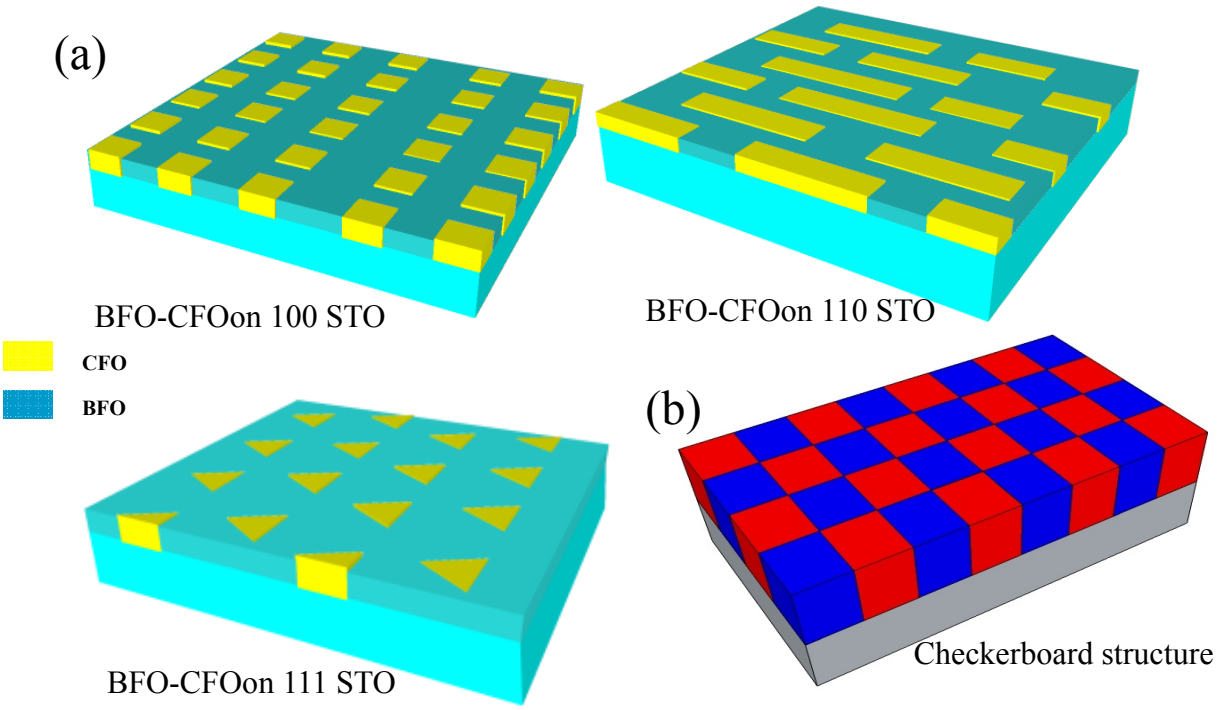

Figure 1.9. (a) BFO-CFO self-assembled thin film grown on (100), (110), (111) STO substrates with different phase architectures. (b) Schematic of checkerboard thin films.

1.6 Objectives and significance of the study

Magnetic and ferroelectric materials have been thoroughly investigated—both in terms of their fundamental properties as well as for their industrial/technological potential. For example, ferromagnetic materials with switchable magnetization driven by an external magnetic field are indispensable in data-storage industries; additionally, sensing industries rely heavily on ferroelectric materials with spontaneous reversible polarization with the application of an external electric field. Magnetoelectric multiferroics combine favorable properties of ferromagnetism and ferroelectricity, thereby opening a new window of opportunity for application usage. ME laminate

structures have been used as magnetic field sensors with sensitivity around 1 nano Tesla due to the significant ME coupling effect between the piezoelectric PZT layer and the magnetostrictive iron-based alloy layer.

However, ME effects in thin film structures are always difficult to predict and even perceive due to the clamping effect from the substrate and small volume of effective materials. The ME coupling effect occurs only when elastic strain is transferred from the piezoelectric layer to the magnetostrictive layer. Specific single-crystal substrates are necessary for the epitaxial growth of ME thin films, e.g., $SrTiO_3$. It should be noted that the thickness of a substrate is usually 500 μm, whereas the thickness of the ME thin film on top is usually less than 1 μm. This means that the effective strain effect should be only about 1/500 of that of the bulk ME structure. Moreover, the effective mass of the ME structure in thin films is even smaller. For a 1 μm-thick ME thin film with 50×50 μm electrodes, the effective mass is only 1/400000 of a 1mm×1mm×1mm ME bulk structure. Strain value is expressed in linear relation with the effective mass of an ME structure. Additionally, the real ME coupling signal of the ME thin film noted above is even smaller than 1/400000 in comparison to the small ME bulk sample due to the substrate clamping effect. Thus, it is difficult to determine the ME coupling coefficient by directly measuring the output voltage in ME thin films. To overcome the clamping effect from the substrate, a self-assembled, vertically-aligned ME structure has been proposed that allows the elastic strain to transfer perpendicularly. BFO-CFO is one typical self-assembled ME structure that has been well studied with respect to both its phase configuration and possible associated ME coupling effects. However, no conclusive answers have been found that detail the ME coupling mechanism in this specific structure.

Therefore, in an attempt to elucidate the magnetoelectric effect in ferroelectric-ferromagnetic heterostructures, this study addressed five fundamental questions (and associated sub-questions):

1. What are the specific phase architectures in BFO-CFO self-assembled thin films grown on variously-oriented STO substrate? How do these different architectures affect the magnetic domain distribution and magnetic anisotropy in CFO nanostructures? To what extent can the magnetization of the CFO component be tuned by the BFO matrix.
2. Is it possible to grow BFO-CFO self-assembled thin films on piezoelectric single-crystal PMN-PT substrates? What is the difference for the ME effects in pure CFO and BFO-CFO thin films on a PMN-PT substrate?
3. Is it possible to grow textured piezoelectric thin films on iron-based alloys with large piezomagnetic coefficients—and by association, is it possible to obtain a large ME coupling coefficient in this monolithic ME structure?
4. What other self-assembled structures can be developed with potential multifunctionality? Is it possible to control the morphology of each phase through selection of materials with different crystal structure and crystal lattice constants?
5. How can one control phase transformation in ferroelectric substrates, and therefore strain conditions in the epitaxial ferromagnetic thin films on top? Is it possible to build an irrefutable relationship between ferroelectric phase transformation and subsequent ME effects? What possible applications can be achieved with the various ME structures mentioned above?

Chapter 2 Experimental Techniques

2.1 Synthesis

All of the thin film samples discussed in this work were grown using pulsed laser deposition (PLD) methods. PLD is a very powerful technique for growing epitaxial and textured thin films with specific orientations, which can be directed by the interface atom layout of the single-crystal substrates. A PLD system is comprised of three basic components: a high-energy laser to eject plasma onto the substrate, a chamber assembled with a pumping system, and target/substrate holders with a heating system. For this study we utilized a Lambda 305. The gas used to excite the laser was KrF; the wavelength of the laser was 248nm; and the pulse width of the laser was around 30ns. The energy and frequency was set between 100mJ~500mJ and 1Hz~10Hz, respectively.

The working principle of our PLD system is illustrated in Figure 2.1. The global chamber is connected with the pumping system, which is comprised of both a mechanical pump and a turbo pump. A background vacuum pressure of 10^{-5}Torr was obtained after two hours of pumping, after which the chamber was filled with oxygen (20-150 mTorr) for the growth of the complex oxide compounds. The laser beam was directed to the target, which rotated during the entire deposition process, by several lenses with high reflectivity. The next step involved generating a plasma surface on top, when tends to move naturally toward the target. The substrates are then attached on a heater with silver paste. It should be noted that a minimum high temperature is essential for thin film growth due to thermal dynamic requirements for substrate thin film interface bonding and crystallization. When the ejected plasma meets the hot

substrate, the target material in formula stoichiometry will be absorbed by the substrate. A single-crystal in thin-film form is then grown on the substrate.

The advantage of PLD is that the high-power laser beam can evaporate various kinds of targets, from metals to oxides. Additionally, if the proper substrate is available, almost any type of thin film can be deposited. PLD is often used to grow epitaxial thin films on top of a single-crystal substrate, however, the lattice mismatch between target material and substrate should be lower than 7% for growth of high-quality thin films. The thickness of the thin film can vary from several nm to several μm, depending on deposition time and growth rate.

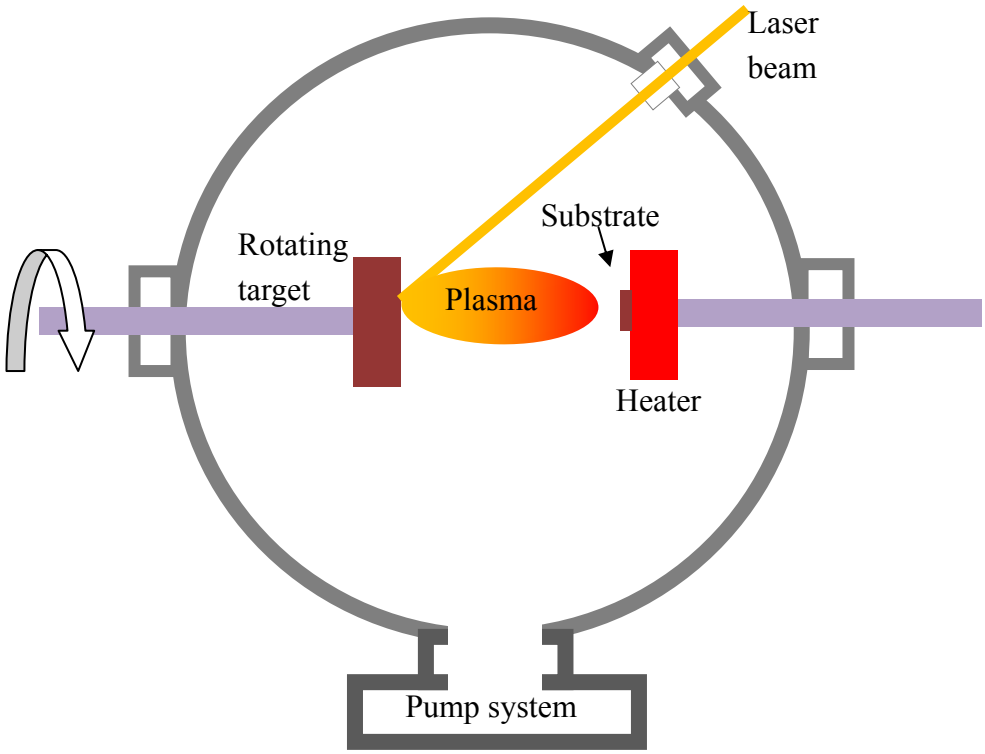

Figure 2.1. Schematic illustration of a PLD system.

2.2 Characterization methods

2.2.1 X-ray diffraction

X-ray diffraction (XRD) is a powerful tool for determining crystal structure, symmetry and lattice parameters. For this study, we utilized a Philips X'pert high-resolution XRD system equipped with a two-bounce hybrid monochromator and an open three-circle Eulerian cradle. The analyzer was a Ge (220) cut crystal with a 2θ-resolution of 0.0068°. The x-ray tube was operated at 45kV and 40mA with a wavelength of 1.5406Å (Cu Kα). During the measurement process, the sample could be tilted (Ψ) by ±90° or rotated (Φ) by 360° to locate the corresponding crystal faces. The lattice parameters of the sample was then calculated as follows:

$$n\lambda=2d\sin\theta$$

where n is an integer, λ is the x-ray wavelength, d is the lattice spacing, and θ is the diffraction angle. Line scans were obtained by scanning 2θ-ω with fixed values of Ψ and Φ, the results of which enabled us to determine the epitaxial structure and lattice parameter of the thin films. We obtained mesh scans from 2θ-ω line scans with changing ω covering a region of reciprocal space defined by 2θ-ω vs ω.

2.2.2 Ferroelectric and ferromagnetic property measurements

Ferroelectric properties were measured using a polarization measurement setup based on a Sawer-Tower circuit, including voltage amplifier, signal generator, oscillograph and reference capacitor, as shown in Fig. 2.2. AC voltage supplied by a signal generator and an amplifier was applied both to the thin films and to a reference capacitor. The capacitance of the reference capacitor was about 100x larger than that

of the thin films. Then, the voltage signal from the thin films, V_{film}, was measured via an oscilloscope in Channel 1, where $Z_{ref} << Z_{film}$. Based on the fact that $Q_{film}=Q_{ref}$ and $Q=C\times V$, we can conclude that $Q_{film}=C_{ref}\times V_{ref}$, where V_{ref} is the signal measured in Channel 2. For ferroelectric thin films, the relationship between Q_{film} and V_{film} is hysteresis.

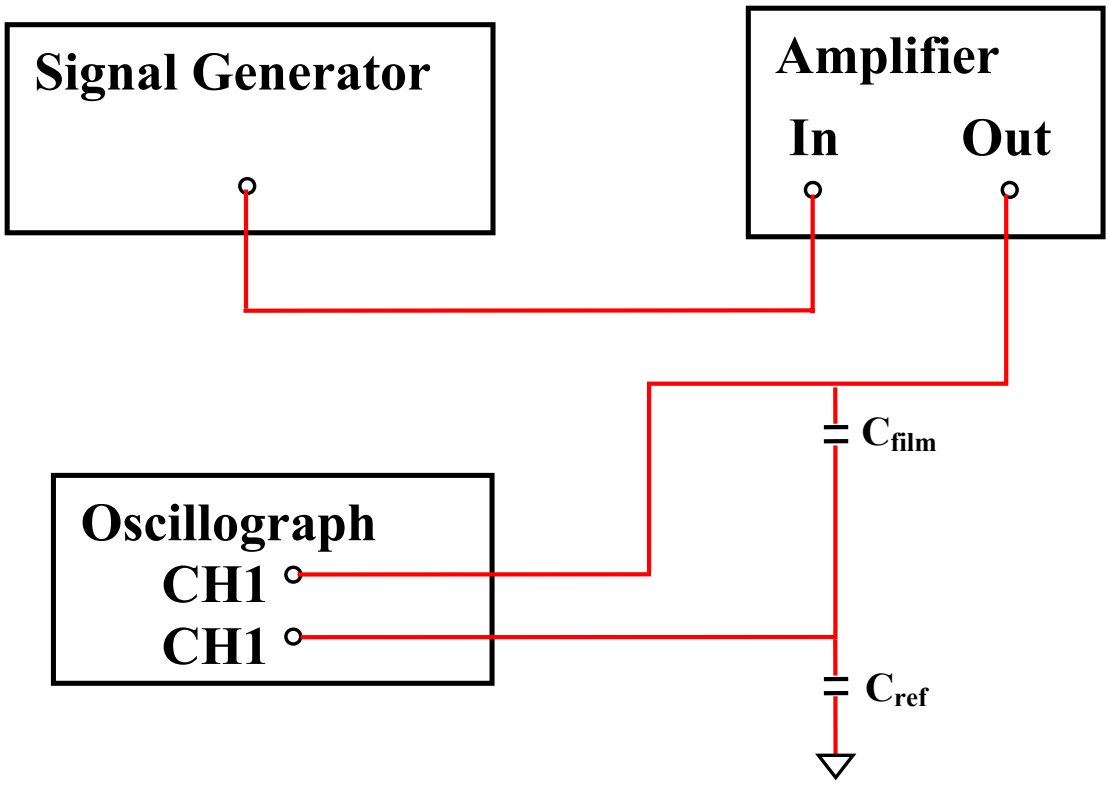

Figure 2.2. Schematic illustration of dielectric polarization measurement.

2.2.3 Vibrating sample magnetometer

Ferromagnetic properties were characterized using a vibrating sample magnetometer (VSM), whereby a sample is placed inside a uniform magnetic field to magnetize the sample. Once that occurs, it is physically vibrated sinusoidally, typically through the use of a piezoelectric material. This vibration induces a magnetic flux change, which subsequently induces voltage in the pick-up coils. In a typical setup, the induced voltage is measured through the use of a lock-in amplifier using the piezoelectric signal as

its reference signal. The magnetic moment determined by the VSM is related to the magnetization of the sample, as shown in Fig. 2.3.

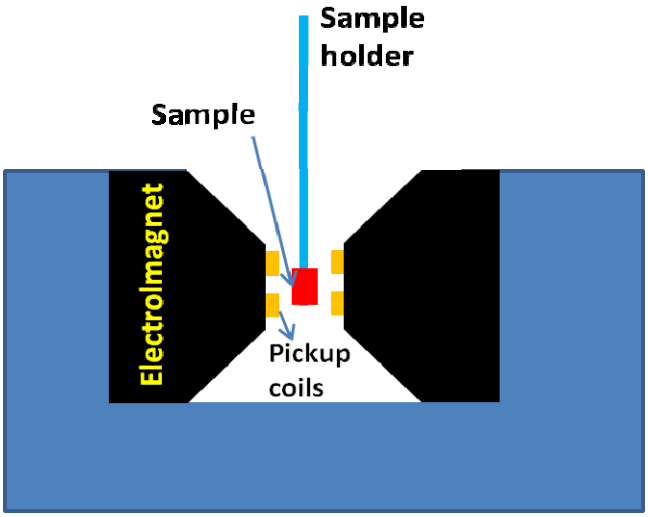

Figure 2.3. Schematic illustration of VSM measurement setup.

2.2.4 AFM, MFM and PFM measurements

Topography results for the thin-film samples were analyzed with atomic force microscopy (AFM), which is an essential tool for studying the top surface of thin films with nanoscale resolution. By changing the tip and scanning mode, various forces can be imaged, such as piezoresponse force microscopy (PFM) and magnetic force microscopy (MFM). These two techniques can be used to image ferroelectric and ferromagnetic domains, respectively.

The basic structure of our AFM head is shown in Fig. 2.4. In terms of operation, a cantilever with a sharp tip at the end is used to detect the top surface of the sample. This cantilever is is mounted at the end of a piezo-ceramic tube, which controls the position of the tip (x, y). The tube has two sets of electrodes, which are normal to each other. When an electric field is applied to the two electrode sets in the piezo-tube, the end of the tube is able to bend in the x or y direction. After careful calibration, the

position of the tip (x, y) can be read by the voltage applied to the tube. During the scan, the tip zigzags on top of the sample surface and the position is recorded in a data file. A laser beam is reflected by the back side of the cantilever to a position-sensitive photo-detector. When the laser dot is in the middle of the photo-detector, the voltage output of the photo-detector is 0V; when the laser dot is on the top of the upper portion of the photo-detector, the voltage output of the photo-detector is positive (+) or negative (-). When the tip is moved on a smooth surface, the reflected laser dot is at the center of the photo-detector; if the tip is on a small bump or pit, the end of the cantilever will bend up or down, thereby reflecting the laser spot up or down in the photo-detector. After calibration, it is possible to measure the height (z) of the defection from the photo-detector's voltage output. By combining the position (x, y) and the height (z) of the tip, a map of the top surface of the sample can be obtained.

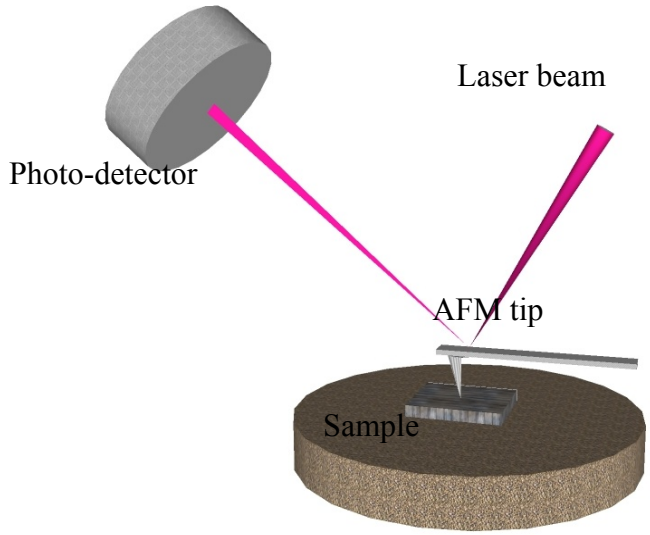

Figure 2.4. Schematic illustration of AFM measurement.

In addition to height, it is also important to determine a sample's phase information. To obtain this data, the tip is driven at the resonance frequency. If the surface of the sample is uniform and flat, the vibration of the tip is constant and stable.

If the tip encounters an uphill gradient or an elastically-stiffer region, the vibration period of the tip is decreased. If the tip encounters a downhill slope or a softer material, the vibration period of the tip is increased. The shift of the vibration period is given by phase. Because phase signals are sometimes stronger than height signals, phase maps of the top surface of a sample can provide important information.

There are three basic scanning modes for AFM: contact, tapping, and lift. In the contact mode, the tip is always touching the surface of the sample. In this mode, tips wear out quickly; additionally, the surface of the sample may become scratched. Despite these drawbacks, by always touching the sample surface, the tip can measure the friction between itself and the sample. Also, in AFM contact mode, the tip can apply an electric field to the sample, which can be used to obtain PFM measurements. In the tapping mode, the tip is tapped on the sample surface at the resonance frequency. In this mode, the tip wears out more slowly, but the risk of scratching the sample is reduced. This is the most widely-used mode for studying sample topography. In the lift mode, the tip is lifted about 10 to 100nm off the surface and never touches the sample. Obviously, tips do not wear out in lift mode, but the resolution of the map is decreased depending on the lift height of the tip. However, a magnetic cantilever can detect a magnetic signal in lift mode, thereby enabling an MFM image to be obtained.

The MFM measurement method is shown in Fig. 2.5. It works in an interleave mode, which means the tip initially scans the surface in tapping mode, after which it scans the same surface in lift mode. In tapping mode, the topography of the sample is recorded; in the lift mode, the topography information is subtracted from the data. Only the response of the magnetic tip to the magnetic signal is recorded in lift mode. If the magnetic tip is on top of a magnetic material, the vibrational frequency of the tip will be changed due to the magnetic force between the tip and sample. Accordingly,

the phase changes of the tip in lift mode reflect the magnetic signal of a given material. The phase map of the lift mode in interleave is used for MFM results.

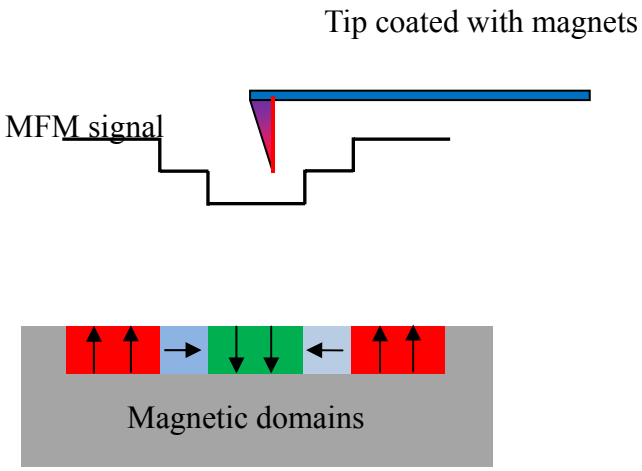

Figure 2.5. Schematic illustration of MFM measurement.

A basic vertical PFM measurement setup is shown in Fig. 2.6. PFM measurement works in piezo-response mode, which is based on contact. The bottom electrode of the sample is connected to the chuck, and the conductive tip is in contact with the top surface of the sample. When an AC or DC electrical field is applied to the tip (top) or sample (bottom), the piezoelectric materials generate a strain. The tip responds to both the height and piezo-response signals that are induced by the applied AC electrical field. However, these two signals operate at different frequencies; specifically, the frequency of the piezo-response signal is much lower in comparison to the height signal. By using two internal lock-in amplifiers, which work at two different frequencies, the height and piezo-response signals can be measured separately. Also, by applying a DC electrical field to the tip of sample, the polarization direction of the piezo material can be rotated. Similarly, lateral PFM results can be obtained by recording the rotation of the tip induced by the in-plane movement of the ferroelectric domains, instead of the height of the tip. In this way, we can map ferroelectric domains in the in-plane direction.

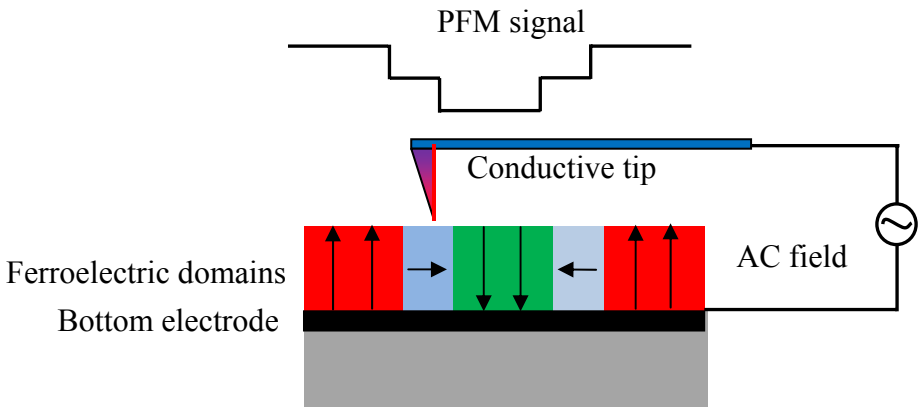

Figure 2.6. Schematic illustration of PFM measurement.

2.2.5 SEM and TEM measurements

An SEM (scanning electron microscope) utilizes a high-energy beam of electrons to scan the surface of a sample. When the electrons interact with the surface atoms of the sample, signals are produced. These signals include those from electrons emitted from the sample, which contain information about the sample's surface topography and local elemental ratio.

Unlike SEM, transmission electron microscopy (TEM) uses a beam of electrons transmitted through ultra-thin specimens. The electron beam interacts with the specimen as it passes through it, and an image is formed from the transmitted electrons on a CCD array detector. Areas that are thick will appear as dark on the array. Obtaining high-quality TEM images is dependent on an ultrathin specimen; thus, ion beam milling and focused ion beam lift out of small regions of a sample are necessary.

Chapter 3 ME Effect in Ferromagnetic Film on Ferroelectric Substrate

The magnetoelectric (ME) effect is a coupling effect between ferroelectric (FE) and ferromagnetic (FM) subsystems, which provides additional degrees of freedom to control either polarization or magnetization with the application of a magnetic field or an electric field, respectively. A sizable ME effect has been achieved in bulk PZT-alloy multilayer structures. However, achieving an ME coupling effect in ME composites in thin-film form is challenging due to the clamping effect from the paraelectric substrate which is much thicker than the thin films on top. Specifically, the substrate stops the movement of the epitaxial ferroelectric and ferromagnetic thin films, making it impossible for elastic strain to be transferred between the FE and FM layers. To solve the substrate clamping problem, single-crystal piezoelectric substrates have been used to deposit epitaxial ferromagnetic thin films, thereby enabling one to control the magnetic response of these films using the strain from the piezoelectric substrate thorough electromechanical coupling. Ferroelectric $Pb(Mg,Nb)O_3$-$PbTiO_3$ (PMN-PT) and ferromagnetic $CoFe_2O_4$ were selected as the ferroelectric and ferromagnetic phases owing to their excellent magnetomechanical and electromechanical performance.

3.1 E-field controlled magnetic anisotropy in Mn doped CFO on PMN-PT substrates

3.1.1 Introduction

The ability to tune magnetic anisotropy in ferromagnetic thin films by an electrical field-induced strain in ferroelectric substrates is an example of the converse magnetoelectric (CME) effect. A variety of studies have confirmed the importance of

CME in appplications that include electric-write magnetic memory and electrical field-tunable microwave devices.[43, 51, 52] Strong coupling between ferroelectric and ferromagnetic phases can be achieved across their inter-phase interfaces through elastic strain mediation in composite ME structures—providing that a ferroelectric phase with a high electromechanical coupling coefficient and a ferromagnetic phase with a high magnetomechanical coupling coefficient are brought together in composite form.[53-56] A phenomenological approach has been used to calculate strain-induced magnetic easy-axis reorientation in various ferromagnetic thin films under electrical fields that have been applied along different directions.[57-59] These studies have predicted the possible existence of a strain-mediated ME random access memory with ultra-high storage capacity, which in turn has stimulated extensive investigations on the growth of epitaxial ferromagnetic thin films on ferroelectric substrates.[60-65]

However, electric field-induced strain in ferroelectric materials is a complex phenomena, where electric polarization rotation and reorientation coexist, and where linear piezoelectric strains are tenable only for modest electric-field ranges.[66, 67] Non-180° domain reorientation and polarization rotation (i.e. monoclinic phase transitions) under an electric field can trigger a step change in the crystal lattice parameters, thereby inducing a large strain. Moreover, in view of the fact that strain is a tensor property, the question of how effective strain transfers between substrate and film must be kept in mind: this is because across the two-dimensional interface between film and substrate, in-plane strain can be transferred, but not the out-of-plane component. Prior studies have indicated that when an electric field is applied across the FM/FE heterostructure, <110>-oriented (1-x)Pb(Mg,Nb)O_3-x$PbTiO_3$ (PMN-PT) crystals with large transverse piezoelectric (d_{31}) coefficients, which have had FM thin

films deposited on top, have demonstrated significantly larger converse ME effects than <001>-oriented ones with a larger longitudinal piezoelectric (d_{33}) coefficient.[68, 69] A few previous studies about ME effects in FM/FE heterostructures have considered PMN-PT substrates, but only as a linear piezoelectric strain source. However, another important property of <110>-oriented PMN-PT crystals is the coexistence of both volatile and nonvolatile strains induced by electrically-controlled phase transformations.

The following section describes the growth of epitaxial Mn-doped $CoFe_2O_4$ (MCFO) thin films on <110>-oriented PMN-PT single-crystals with different $PbTiO_3$ content—thus exemplifying the particular case of substrates with different phase transition sequences. We then carreid out a systematic study of the reversible and irreversible electric field-induced strain effects on the tunable magnetic response of ferromagnetic thin films.

3.1.2 Epitaxial growth of Mn-doped CFO on PMN-PT

Mn (20at%)-doped CFO with a large saturation magnetization and high permeability was selected as the ferromagnetic phase. Although the saturation magnetostriction (λ) was slightly decreased compared to that of unsubstituted CFO, the steeper λ-H curves resulted in a larger piezomagnetic coefficient as a consequence of the higher magnetic permeability.[56, 70, 71] PMN-PT single crystals were selected as the ferroelectric substrate due to ultrahigh electromechanical properties in the vicinity of the morphotropic phase boundary (MPB), which is connected to polarization rotation within a flat free energy profile.[72, 73] Moreover, PMN-PT has a moderate crystal lattice mismatch with ferromagnetic ferrites. This feature makes it an ideal substrate for growing epitaxial ferromagnetic thin films where strain parameters can be effectively controlled by an electric field.

For this study, epitaxial MCFO thin films with a thickness of about 200 nm were deposited on <110>-oriented PMN-PT substrates by pulsed laser deposition. Film growth was carried out under an 90 mTorr oxygen pressure environment at 800°C using a laser frequency of 10 Hz.

3.1.3 E-field history dependence of phase evolution in PMN-PT

In an (1-x)PMN-xPT solid solution, a spectrum of structures with different spontaneous polarization (P_s) directions can be 'tuned' by $PbTiO_3$ content. Specifically, a rhomohedral (R) structure with P_s//<111> is stable for x<0.30, a monoclinic (M) is stable for 0.3<x<0.35, and a tetragonal (T) is stable for x>0.35.[74] In addition, phase transformation and polarization direction rotation are known to be induced by external electric fields, resulting in significant changes in the unit cell parameters. For example, a giant strain of up to 1.6% has been reported at a R→T transformation, where the polarization rotates from the <111> to <001> directions along which E was applied.[67] Furthermore, the electrically-induced strain due to polarization rotation can be volatile or nonvolatile, given that the intermediate M and orthorhombic (O) phases have different stabilities on removal of E for crystals with different compositions.[66] In the case of volatile polarization rotation, the polar domains rotate back to their initial direction and recover their original state after removal of E; whereas in nonvolatile polarization rotation, the induced strain state is metastable, wherein an energy barrier impedes the recovery of the original polarization direction on removal of E.

Figure 3.1 shows the evolution of the polarization direction with a field applied along <110> in the R phase PMN-PT substrate in out-of-plane. Initially, there are eight possible polarization directions along the four body diagonals in the pseudo-cubic crystal cell, as shown in Figure 3.1 (a). Next, an electric field (E_{up}) along

the out-of-plane (OP) <110> direction can degenerate these eight possible polarization directions into two acclivous ones with an inclined angle of ~35° from the poling field (Fig.3.1b). As E_{up} is increased, the two possible acclivous polarization orientations tilt further towards the direction of E_{up}, resulting in a mono-domain O phase, as shown in Figure 3.1 (c). Upon removal of E_{up} two situations may occur: (i) a metastable mono-domain O phase might remain with polarization along <110>; (ii) the polarization can rotate back to the <111> directions and recover the original R phase condition, as shown in Figure 3.1 (d) and (e). In the present investigation, PMN-PT substrates with three different PT contents of 28at%, 29.5at%, and 30at% (denoted as PMN-28PT, PMN-29.5PT, and PMN-30PT) were selected, which possessed varying degrees of volatile and nonvolatile strains.

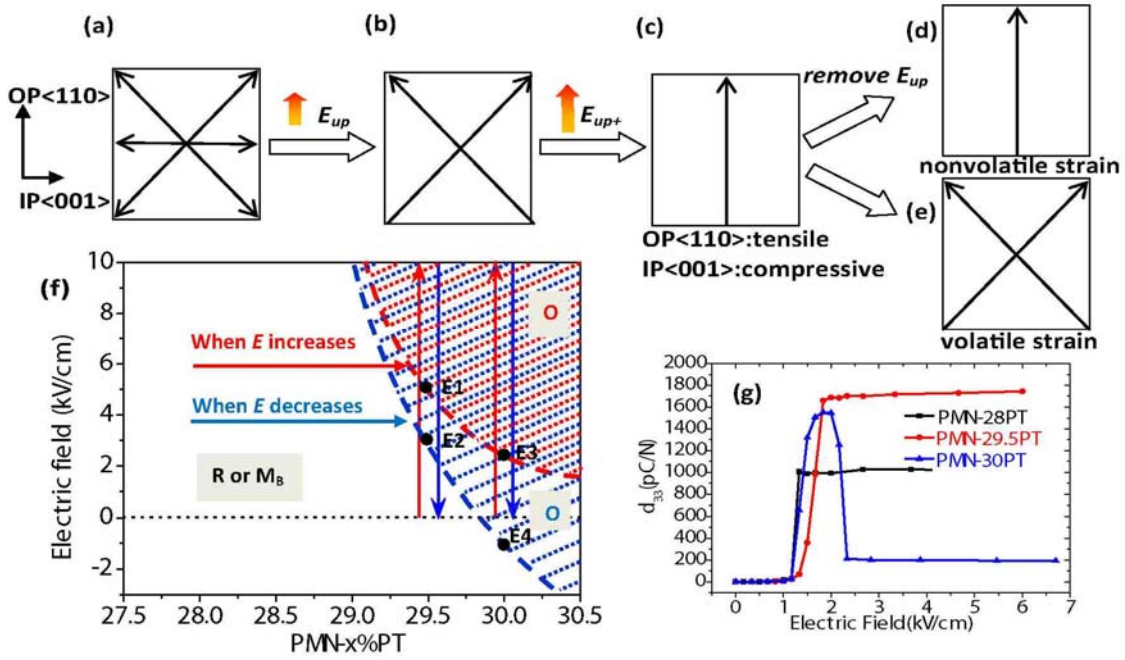

Figure 3.1. Schematic illustrations of polarization rotation of <110> oriented PMN-PT under different electric-field. (a) Projection of intrinsic eight possible *P* directions seen from IP<110> direction. (b) Two possible *P* directions degenerated by a upward electric field (E_{up}). (c) Further tiling of *P* directions towards the electric-field direction under an increasing electric field (E_{up+}) and formation of a mono-domain O-phase. (d), (e) Two possible remaining ferroelectric domain configurations after removal of external electric-field, resulting in O- and R-phases with nonvolatile and volatile strains, respectively. (f) Phase diagram of PMN-xPT at different electric-field. (g) Piezoelectric coefficient of PMN-PT crystals after different electric-field poling.

Figure 3.1(f) shows the phase diagram of PMN-xPT under different electric fields of -2≤ E ≤10 kV/cm. PMN-28PT remained within the R-phase stability range, possessing a linear strain-E relationship.[75] PMN-29.5PT exhibited a R→O transform at E1 as the electric field was increased, but recovered the original R-phase at E_2 as the electric field was subsequently decreased ($0 \le E_2 \le E_1$).[76] PMN-30PT transformed from R→O phases at E_3 as the field was increased, and then recovered the original R

phase at E_4 as a field of opposite sign was applied. ($E_4 \leq 0 \leq E_3$).[77] The relationship between the four threshold electric fields (E_1 to E_4) was determined by dielectric constant measurement as a function of temperature, as shown in Figure 3.2. To further confirm the phase stability of the PMN-PT crystals under different electric fields, we measured the piezoelectric coefficient of each sample after poling under different electric fields, as shown in Figure 3.1 (g). PMN-28PT and PMN-29.5PT exhibited a monotonically increasing value of d_{33} with step jumps near 1.2 and 1.5 kV/cm, respectively. However, the piezoelectric coefficient of PMN-30PT first experienced a rapid increasing range for $1.1 \leq E \leq 1.8$ kV/cm (d_{33}=1550pC/N @1.8kV/cm), and then a rapid decreasing one for $2 \leq E \leq 2.5$ kV/cm. A low value of $d_{33} \approx 200$ pC/N was found for E= 2.5 kV/cm. The piezoelectric coefficients were measured in real time, using a d_{33} meter after removal of the poling field and were not calculated from the strain-E curve. Each point represents the average value of three separate measurements. Accordingly, the low value of d_{33} as the poling field was increased can be only attributed to the formation and stabilization of a mono-domain O phase.

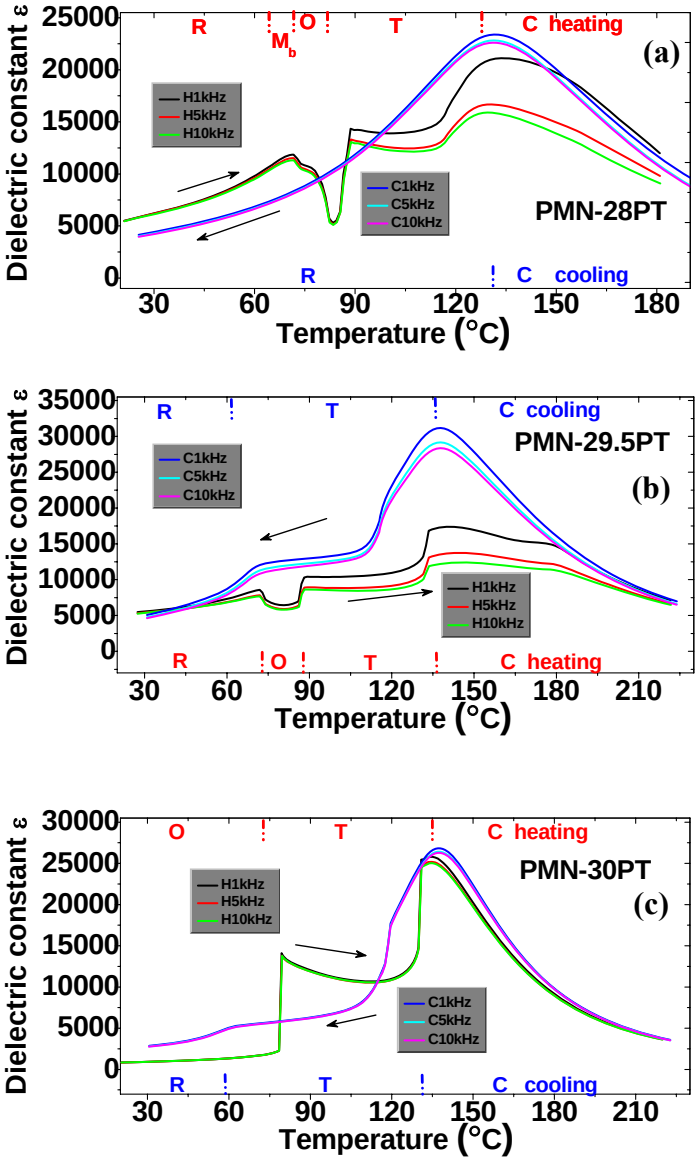

Figure 3.2. Dielectric constant as a function of temperature for PMN-28PT (a), PMN-29.5PT (b) and PMN-30PT (c) after 10kV/cm poling for both heating and cooling processes.

3.1.4 E-field-induced uniaxial strian modulation of magnetic response in MCFO film

Figure 3.3 shows the magnetization hysteresis loops (M-H) for an epitaxial MCFO thin film grown on PMN-28PT under various E values applied along the out-of-plane direction. Results showed that as the electric field increased, the

polarization orientation was tilted towards the out-of-plane direction, which resulted in a compressive strain along the <100> in-plane (IP) direction, and a tensile strain along the IP <110>. Figures 3.3 (a), (b) and (c) show variations in the M-H loops for data taken along <001> (IP), <110> (IP), and <110> (OP), respectively. Measurements were performed for 0≤ E≤ 10 kV/cm. The MCFO layer has a negative magnetostriction along both <100> and <110>, thus switching the magnetic domains along <001> (IP) will become increasingly difficult in the heterostructure with increasing E due to a compressive strain, resulting in increased remnant magnetization (M_r). Conversely, along the <110> (IP) and <110> (OP) directions, magnetic domain switching should become "softer" due to tensile strain, resulting in a decreased M_r. Figure 3.3 (d) shows the M_r/M_s ratio (R_M) as a function of E applied along these three directions. Initially, <110> (IP) was the easy axis with R_M ≈3.9, whereas the <001> (IP) was the harder axis with R_M ≈2.6. However, as the E applied out-of-plane was increased, a large anisotropic strain was induced in the MCFO film by the PMN-PT substrate. This trend resulted in a change in the magnetic response—namely, the <001> (IP) direction became the magnetic easy axis due to the compressive strain for E> 4 kV/cm. The <110> (OP) direction was consistently the hard axis due to the magnetic shape anisotropy. Note the linearity of the relationship between R_M and E along all the three orientations: $R_{M\text{-}ip<110>}$=3.9–0.014×E, $R_{M\text{-}ip<100>}$=2.6+0.014×E, and $R_{M\text{-}op<110>}$=1.15–0.001×E. The magnetic strain anisotropy energy (U_{strain}) can thus be estimated to be linear with E since the R-phase is more stable in PMN-28PT.[78-81] However, the specific relationship between R_M and U_{strain} is difficult to deduce, and first principle calculations or micro-magnetic simulations are needed to develop a more detailed understanding. Interestingly, a similar linear relationship has previously been reported in Ni/PMN-PT heterostructures.[59] Therefore, it is reasonable to presume

that the R_M of ferromagnetic films will change in proportion to the strain applied by the piezoelectric substrate. The complete recovery of the magnetic anisotropy indicates that the polarization rotates back to the original <111> direction (R-phase) on removal of E.

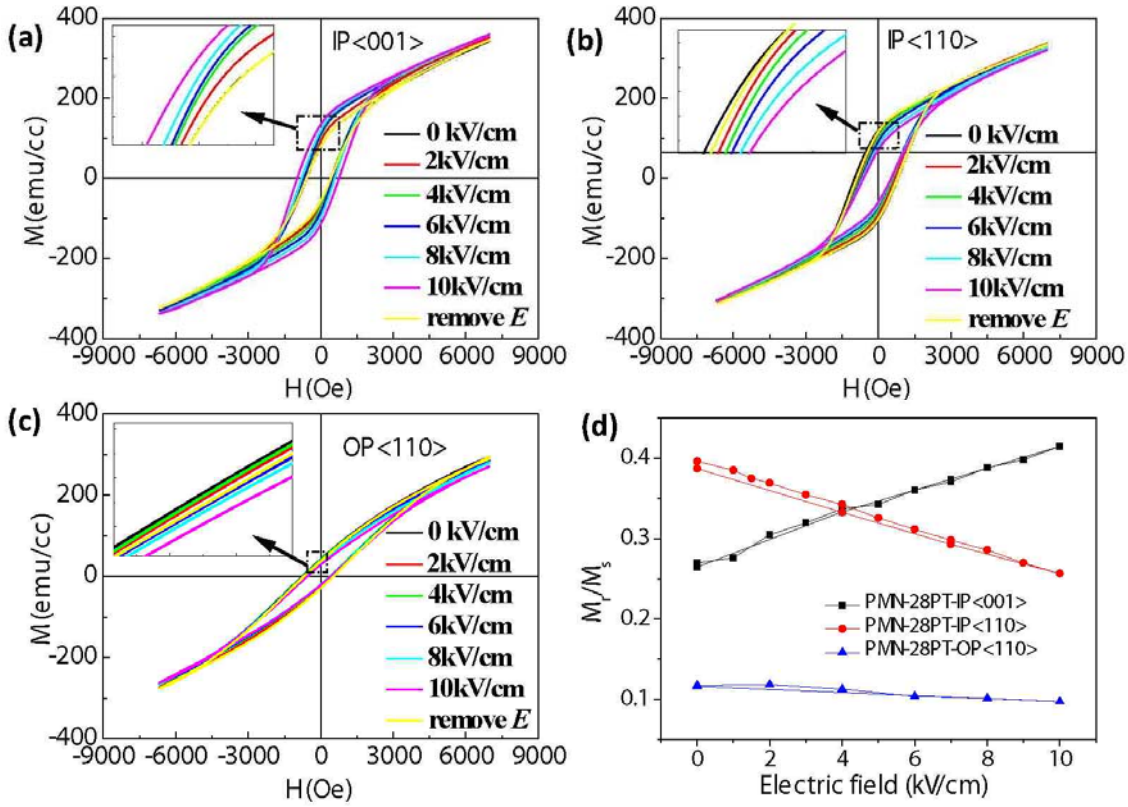

Figure 3.3. M-H loops of MCFO/PMN-28PT along <001> (IP) (a), <110> (IP) (b) and <110> (OP) (c) directions under different electric-field. (d) M_r/M_s ratio as a function of applied electric-field.

Figure 3.4 shows analogous magnetic property measurements for a MCFO thin film on PMN-29.5PT. Again, along <100> (IP), the magnetic domains became "harder_ due to an E-induced compressive strain; whereas those along <110> (IP) and <110> (OP) became "softer" due to tensile strains. Figure 3.4 (d) shows the relationship between $R_M=M_r/M_s$ and E. For PMN-29.5PT, E can induce a R→O phase transition by rotating the polarization from <111> to <110> (OP). Therefore,

remnant magnetization will experience an electric field-sensitive initial stage for 0<E<5 kV/cm, which is associated with the large electromechanical coupling coefficient in the polarization rotation process. The value of M_r/M_s will then become relatively stable for E>5.5 kV/cm due to a complete R→O phase transformation. Moreover, a jump of the R_M value in the field range of 5<E<5.5 kV/cm for all three directions was trigged by approaching the threshold of the R→O phase transformation,[75] similar to the strain increase induced by the R→T phase transition in <001> oriented PMN-PT crystals.[67]

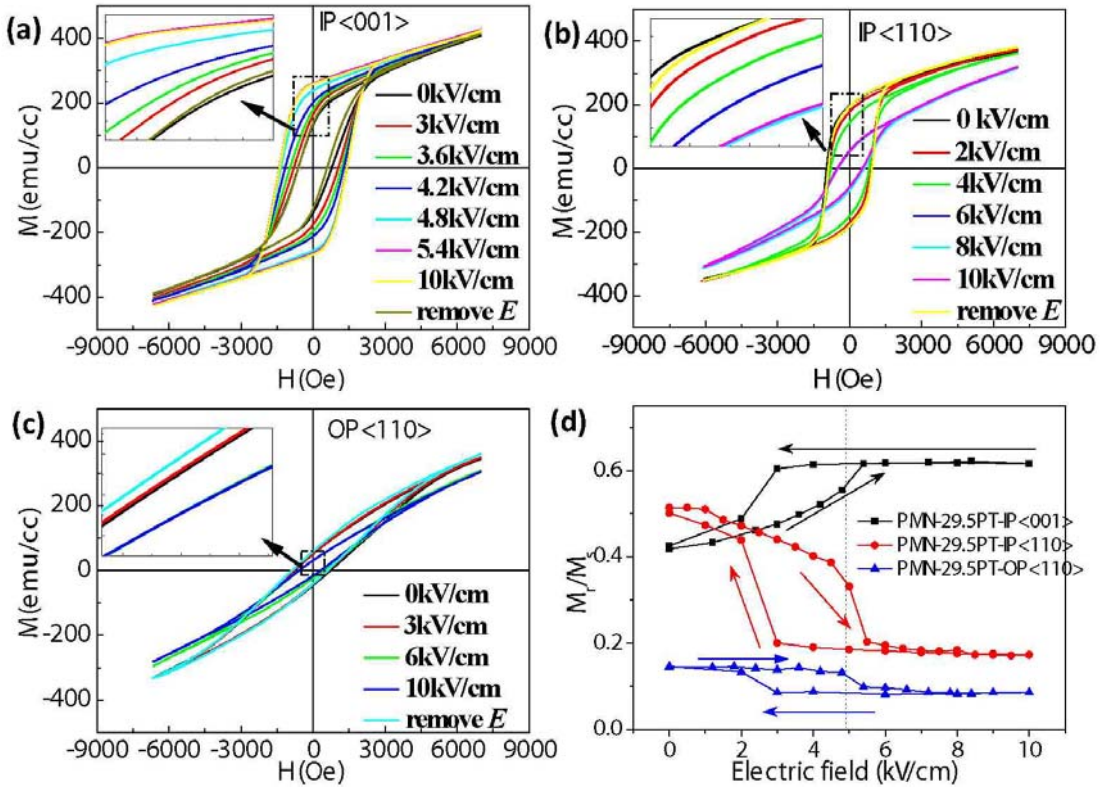

Figure 3.4. M-H loops of MCFO/PMN-29.5PT along <001> (IP) (a), <110> (IP) (b) and <110> (OP) (c) directions under different electric-field. (d) M_r/M_s ratio as a function of applied electric-field.

Table 3.1 summarizes a comparison of R_M with E for MCFO films grown on PMN-28PT and PMN-29.5PT. The value of R_M exhibited a linear relationship with E

for the MCFO thin films on PMN-28PT due to the linearity of the piezoelectric coefficient d_{31} with the electric field range of 0<E<10 kV/cm. In comparison, R_M changed three times faster for the MCFO thin films on PMN-29.5PT in the initial field range of 0<E<5 kV/cm; in contrast, for E>5.5 kV/cm, R_M was nearly independent of E as the R→O transition was complete. In addition, the R_M-E curve for MCFO on PMN-29.5PT exhibited hysteresis in the field range of 3-5 kV/cm with a stepping increase at E≈5 kV/cm with increasing E and a step decrease at E≈3 kV/cm with decreasing E, in agreement with feature changes in the strain loops.[75] Overall, the MCFO on PMN-29.5PT exhibited a larger nonlinear converse ME effect due to the R→O phase transformation—whereas the MCFO on PMN-28PT revealed a smaller linear converse ME effect over a wider field range of 0<E<10 kV/cm.

Table 3.1. Magnetization remanence (R_M) difference in different electric-field ranges in three feature directions.

$\frac{\Delta(M_r/M_s)}{\Delta H}$ (Oe)	PMN-28PT (0→10kV/cm)	PMN-29.5PT (0→5kV/cm)	PMN-29.5PT (5→5.5kV/cm)	PMN-29.5PT (5.5→10kV/cm)
IP<100>	15	40	130	0
IP<110>	-14	-53	-267	0
OP<110>	-2	-9	-59	-2

Figure 3.5 shows M-H loops for a MCFO film on PMN-30PT under various electric fields. The value of M_r along <100> (IP) increased slowly at low fields, after which a dramatic increase was found near 2kV/cm due to the compressive strain induced by the R→O transformation (Fig.3.5a). At this point, the PMN-30PT experienced stable mono-domain O state, resulting in constant M_r and M_s values after removal of E. Dramatic changes in M_r values were also found along the <110> (IP) and <110> (OP) directions near 2 kV/cm. It is important to emphasize that the

field-induced strains in PMN-30PT are stable upon removal of E in the absence of another driving force. Overall, a stable field-induced mono-domain O state in the PMN-30PT substrates resulted in a non-volatile converse ME effect in the MCFO films. Both reversible and irreversible converse ME effects have been detected due to the volatile and nonvolatile strains induced by electric fields applied across PMN-PT crystals with different compositions.

Next, we investigated how magnetic anisotropy is affected by variable strain. The magnetic anisotropy energy (E_{ani}) in a ferromagnetic thin film can be expressed as:

$$U_{ani}=U_{mc}+U_{ex}+U_{shape}+U_{strain};$$

where U_{mc} is the magneto-crystalline anisotropy energy, U_{ex} is the magneto-exchange anisotropy energy, U_{shape} is the magneto-static anisotropy energy, and U_{strain} is the magneto-elastic anisotropy energy.[57] U_{mc} and U_{ex} are related to the intrinsic crystal structure and specific distribution of the magnetic domains in thin films that are difficult to manipulate—and are beyond the scope of this research.[82] In contrast, U_{strain} can be easily controlled for ferromagnetic thin films on piezoelectric substrates via the application of an electric field.

The PMN-PT substrates used in this investigation had a typical dimension of $5\times5\times0.5$ mm^3, as shown in Figure 3.6 (a). Because U_{shape} is determined by the specific dimensions of a magnetic thin film, the magnetic easy axes is along the length direction due to U_{shape}, as shown in Figure 3.6 (b). After applying an electric field along the out-of-plane direction, the MCFO film will elongate along <110> (IP) and shrink along <001> (IP), as shown in Figure 3.6 (c). Although the U_{shape} associated with this dimension change has a tendency to rotate the magnetic easy axis to the

elongated direction (IP<110>), this effect is negligible due to the small aspect ratio difference compared with the large U_{strain} induced by electromechanical coupling.

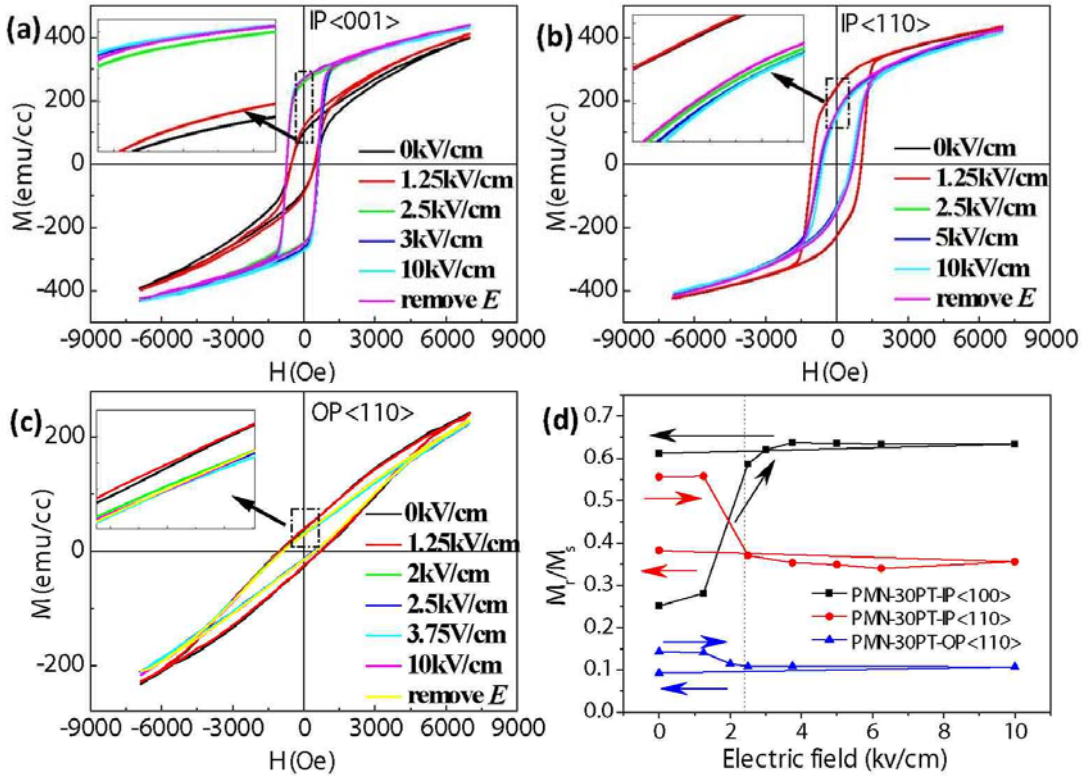

Figure 3.5. M-H loops of MCFO/PMN-30PT along <001> (IP) (a), <110> (IP) (b) and <110> (OP) (c) directions under different electric-field. (d) M_r/M_s ratio as a function of applied electric field.

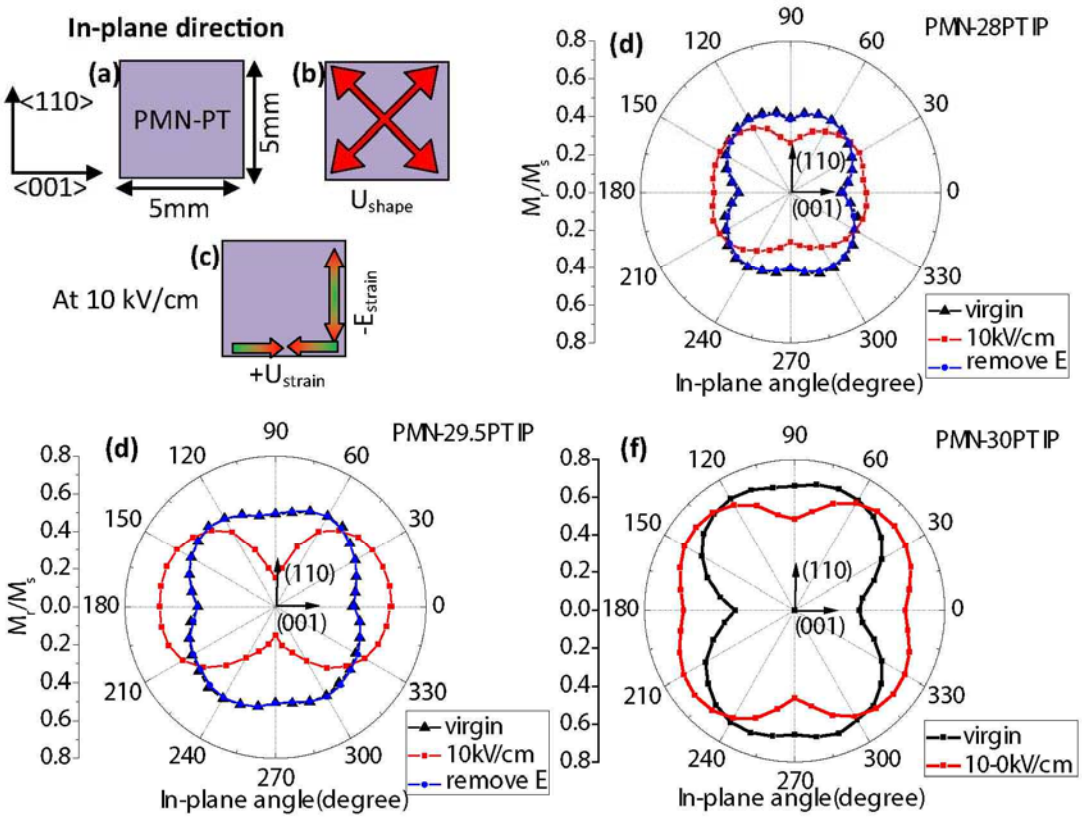

Figure 3.6. (a) In-plane dimension of PMN-PT crystals. (b) Schematic of magnetic shape anisotropy induced easy axis. (c) Schematic of electric field-induced strain. (d-f) M_r/M_s ratio distribution in the in-plane directions with different electric-field conditions: 'virgin' means the as-prepared MCFO/PMN-PT heterostructure without application of an electric field; '10-0kV/cm' means the curve is measured at 0 kV/cm after removal of the 10 kV/cm electric-field, that is the magnetic response of poled MCFO/PMN-PT.

Figure 3.6 (d) shows the anisotropy of M_r/M_s (i.e. R_M) distribution in a MCFO thin film on PMN-28PT for different electric-field conditions. First, the MCFO film displayed larger remnant magnetization along the directions diagonal to the square crystal due to a large shape anisotropy that could not be controlled by E. Second, increased and decreased values for M_r can be found along the <001> (IP) and <110> (IP) directions, respectively, after application of E=10 kV/cm to the PMN-PT

substrates. Third, the values for M_r were similar for the MCFO/PMN-28PT heterostructure before and after application of 10kV/cm, indicating a complete recovery of the original magnetic anisotropy condition after removal of E. These results demonstrate a reversible rotation of the magnetic easy axis from <110> (IP) to <001> (IP) by E. (It should be noted that we only compared the in-plane <110> and in-plane <001> directions, but not the diagonal ones where the M_r could not be effectively turned by E.) Figure 3.6 (e) shows the anisotropy of R_M for a MCFO film on PMN-29.5PT under different field conditions. Again, a reversible rotation of the magnetic easy axis from <110> (IP) to <100> (IP) by E was observed. The value of R_M along the <001> (IP) at 10 kV/cm was 1.5 times larger than that at 0 kV/cm; whereas along the <110> (IP), at 10 kV/cm, it was only 1/3 of the value that at 0 kV/cm. Figure 3.6 (f) shows the anisotropy of R_M for an MCFO film on PMN-30PT. Again, a rotation of the magnetic easy axis from <110> (IP) to <100> (IP) by E can be seen after application of 10 kV/cm to the PMN-30PT substrate. The value of R_M increased from 0.25 to 0.63 along <001> (IP); in contrast, along <110> (IP) it decreased from 0.56 to 0.36 as E increased from 0 to 10 kV/cm. Moreover, the field-induced changes in M_r were preserved upon removal of E, demonstrating an irreversible magnetic easy axis rotation.

3.1.5 Summary

In summary, large reversible and irreversible field-induced strains in PMN-PT single-crystal substrates have been used to tune the magnetic anisotropy of epitaxial magnetic ferrite films. Thin films of MCFO on PMN-28PT and PMN-29.5PT both exhibited volatile strain-mediated magnetic anisotropy variations with an easy axis that changed from being along <110> (in-plane) to <001> (in-plane) under electric field application, which then recovered its original condition upon removal of E. In

contrast, the MCFO films on PMN-30PT exhibited a nonvolatile strain-mediated magnetic anisotropy variation with a permanent easy axis change from <110> (in-plane) to <100> (in-plane). These results clearly demonstrate the strong coupling between ferroelectric and ferromagnetic orders. Moreover, the volatile and nonvolatile magnetic anisotropy tunability described herein may provide additional approaches to magnetic memory and spintronic applications.

3.2 E-field modulation of magnetic coercive field in CFO/PMN-PT heterostructures

3.2.1 Introduction

Cobalt ferrite or CFO has been the subject of many investigations because of its large magnetostriction, magnetocrystalline anisotropy, and unique nonlinear spin-wave properties. These properties show promise for applications including data storage, sensing, drug delivery, and imaging.[83-88] The magnetic coercive field (H_c), in particular, is one of the most important parameters for these applications.[89] For example, magnetic materials with high coercivity and perpendicular magnetic anisotropy have been used in ultrahigh-density recording.[90, 91]

There are three principal ways for controlling the magnetic coercive field in ferromagnetic materials. First, by considering architecture design and fabrication of magnetic nanostructures with different aspect ratios and particle sizes, one can significnatly alter the magnetic coercive field due to magnetic shape anisotropy and quantum effects.[82] Second, the temperature dependence of H_c enables laser heat assistance in magnetic perpendicular recording (HTMR), where H_c can be dramatically decreased as the bit area is heated to the magnetic Curie temperature.[92] Third, elastic strain has proven to be effective in the control of H_c,[93, 94] where the

magnetic shape anisotropy can be controlled only during the fabrication process. It is important to note that high-temperature treatment of a memory cell induces error in the writing process, and also that the writing rate is restricted by the cooling rate of the heated bit area.[95, 96] However, elastic strain control of H_c can be realized through magnetoelectric (ME) exchange, where the electric and magnetic orders are coupled. Thus, electric-field-tunable H_c can be used in the fabrication of memory devices with high recording density and high operating rates, as well as low energy consumption.[65]

Studies describing the deposition of ferromagnetic thin films on piezoelectric single crystals have been reported.[63, 64] However, these reports focused on PMN-xPT crystals whose compositions were in the vicinity of the morphotropic phase boundary (MPB); these crystals were selected in order to take advantage of their high piezoelectric coefficients. Renault *et al.*[97] systematically studied the temperature range capable of generating an electric field-induced orthorhombic (O) phase in $Pb(Zn_{1/3}Nb_{2/3})_{0.955}Ti_{0.045}O_3$. Their results clearly confirmed that the electric field along ⟨101⟩ can rotate the spontaneous polarizations into ones along ⟨101⟩, forming a monodomain O phase. Quite recently, Franzbach *et al.*[98] investigated the value of the electric field for tetragonal (T) to O phase transformation, which showed an linear relationship with temperature. As for PMN-PT, we have previously reported that the electric field phase transition was in the vicinity of MPB, where electric field-induced strains smaller than 0.4% were observed.[77, 99, 100] Alternatively, much larger strains could be induced by polarization reorientation in T phase PMN-PT, where the unit cells tend to align their long axes along the external electric field.[101] The induced strain ε is proportional to the difference between lattice parameters of the long and short axes: *i.e.* $\varepsilon=(c-a)/a$.[102] A step decrease in magnetization of ~65% has previously been reported for $(La,Sr)MnO_3$ films on BTO (T-phase) heterostructures.[43] The value

of ε in T-phase PMN-PT can reach 2%, whereas the corresponding value for BTO is only 1.1%.[103, 104] Accordingly, a much larger polarization reorientation-induced strain can be expected in tetragonal structured PMN-PT single crystals.

The following section describes the epitaxial growth of CFO thin films on ⟨011⟩ oriented PMN-38PT single-crystal substrates, along with systematic studies of the change in both the remnant magnetization (M_r) and H_c due to the uniaxial strain induced by an electric field applied to the substrate along the in-plane direction.

3.2.2 Epitaxial growth of CFO thin film on <011>-oriented PMN-38PT substrate

PMN-38PT substrates with a dimension size of 5mm×5mm×0.5mm and featuring a tetragonal (T) structure were grown at the Shanghai Institute of Ceramics Chinese Academy Sciences using the Bridgman method. The thickness of the CFO films was 400 nm after one hour deposition by pulsed laser deposition (KrF excimer laser, λ=248 nm) at 800°C. The laser was focused to a spot size of about 2 mm^2, and was incident on the surface of the target using an energy density of 6 J/cm^2. The distance between the substrate and target was 6 cm, and the base vacuum of the chamber was 10^{-6} Torr. During film deposition, the oxygen pressure was 90 mTorr. Magnetic hysteresis (M-H) loops were measured with a Lakeshore 7300 series vibrating sample magnetometer (VSM) system at room temperature. The samples were connected to a Bertan high voltage power supply (210-20R) in order to apply the electric fields.

3.2.3 Polarization reorientation induced uniaxial strain

First, we measured the dielectric constant (ε) as a function of temperature to confirm the composition of the PMN-PT substrate, as shown in Figure 3.7. We then measured the value of ε in both heating and cooling processes; the temperature at which ε showed the largest value was consideded to be the Curie tempearture (T_c) of

the ferroelectric PMN-PT substrate. A composition of PMN-38PT can be determined with a Curie temperature of 450 K, which agreed well with that of the raw material for PMN-PT single-crystal growth.

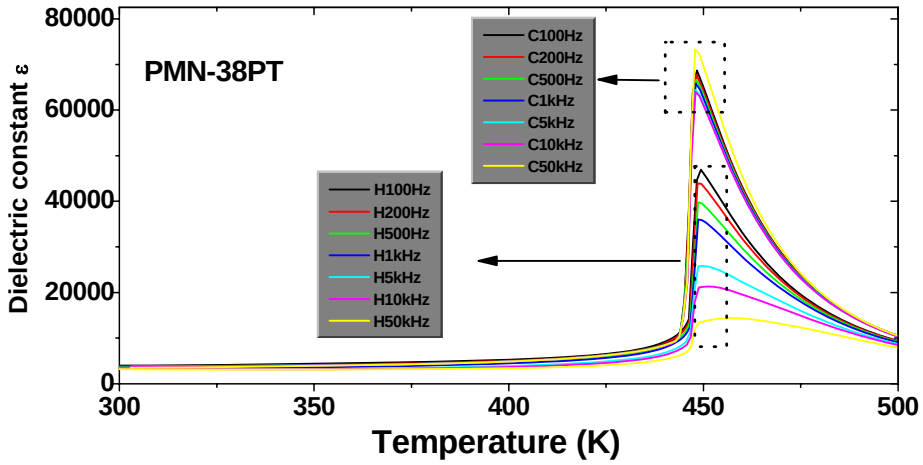

Figure 3.7. Dielectric constant measurement as a function of temperature for poled PMN-PT substrates, showing a T_c=450 K.

Figure 3.8 illustrates the polarization reorientation-induced uniaxial strain within both the $(\vec{y},\vec{z})$ and $(\vec{x},\vec{y})$ planes The tetragonal phase of PMN-38PT has six possible polarization orientations, as shown in Figure 3.8(a). The application of an electric field (*E*) along the out-of-plane direction will align these orientations to being closer to the direction of *E*. Since the crystal lattice parameters of PMN-38PT are longer along the polar direction, polarization reorientation will induce a large strain that can then be transmitted to an epitaxially-grown film.[105] In the $(\vec{y},\vec{z})$ plane, there are six possible polarization projections along $\vec{y}$ and $\vec{z}$ before the application of *E*. However, these six will degenerate into two possible orientations that are directed upwards after application of a sufficiently large *E* along the out-of-plane direction. This will result in a polarization projection along only $\vec{z}$, as shown in Figure 3.8(b).

Accordingly, tensile and compressive strains can be expected along $\vec{z}$ and $\vec{y}$, respectively. In the $(\vec{x},\vec{y})$ plane, under application of *E*, the four possible polarization projections will degenerate into two along $\vec{x}$. This process will result in tensile and compressive strains along $\vec{x}$ and $\vec{y}$, respectively, as shown in Figure 3.8(c). Two different types of domains can be identified based on the d-spacing between adjacent planes along the out-of-plane direction: domain-I whose polarization is along $\vec{y}$ with $d_1 = \frac{\sqrt{2}a}{2}$, and domain-II whose polarization is not along $\vec{y}$ with $d_2 = \frac{a \times c}{\sqrt{a^2+c^2}}$, where *a* and *c* are the T crystal lattice parameters, and d_1 and d_2 are the distances between adjacent planes along $\vec{z}$. Figure 3.8(d) shows a comparison of XRD line scans before and after poling: the (110) peak is from domain-I, whereas the (101) one is from domain-II. After poling the substrate, the (110) peak disappeared. This demonstrates a complete domain-I→domain-II transformation under *E*. The crystal lattice parameters of the T structure were calculated from the 2θ positions and determined to be (*a*, *c*)=(3.980Å, 4.031Å). Thus, a complete domain-I→domain-II transformation would result in a compressive strain of $\frac{a-c}{c} = -1.3\%$ along $\vec{y}$, and a tensile strain of $\frac{\sqrt{a^2+c^2}-\sqrt{2}a}{\sqrt{2}a} = 0.64\%$ along $\vec{x}$.

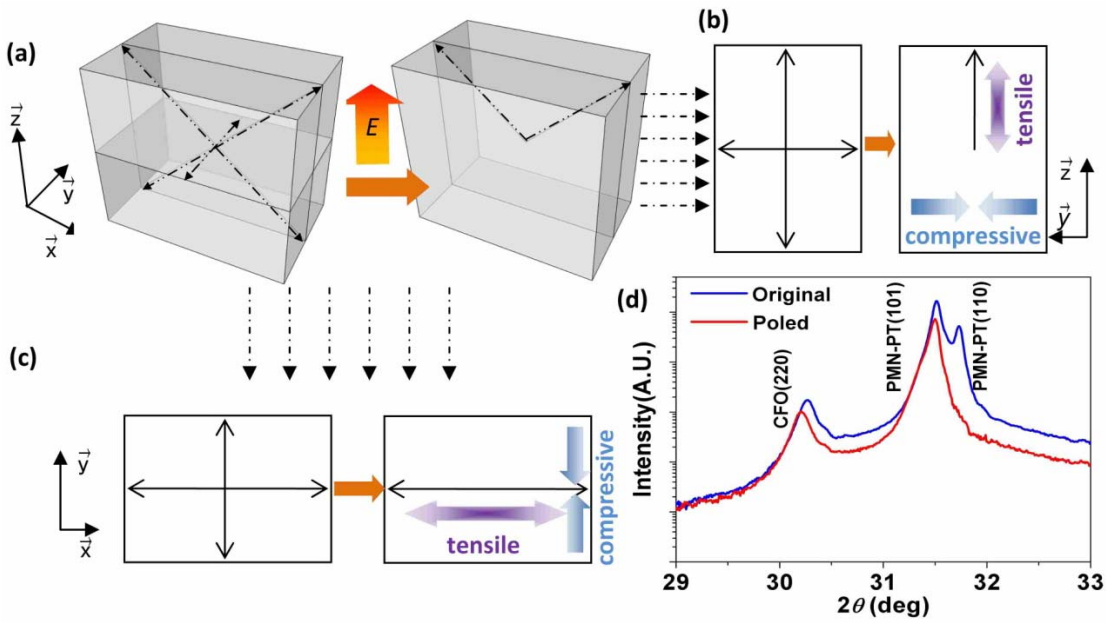

Figure 3.8. Schematic of polarization reorientation induced uniaxial strains in both in-plane and out-of-plane directions: (a) six possible polarization orientations in tetragonal PMN-PT which degenerate into two upward ones by *E* along out-of-plane; uniaxial strains within $(\vec{y},\vec{z})$ (b) and $(\vec{x},\vec{y})$ (c) planes, respectively; and (d) XRD of CFO thin films on poled and unpoled $\langle 011 \rangle$ oriented PMN-PT substrate.

Figure 3.9 shows the evolution of the XRD line scan with *E* for the PMN-38PT substrates. The as-grown substrates had six equivalent polarization orientations: four belonging to domain-II, and two belonging to domain-I. This figure depicts the intensity of the (101) peak corresponding to domain-II, which can be seen to be stronger than that of the (110) for *E*=0 kV/cm. In this case, we determined that the domain ratio (domain-I/domain-II) was R_d=0.74. Theoretically, in the unpoled state, R_d=0.5, since the domain distribution should be equivalent among the six possible orientations. However, the different domains may have different x-ray line profiles,

and accordingly, R_d is only quasi-linear with the peak intensity ratio. Here, for simplicity, we used the peak intensity ratio to estimate R_d. With increasing E, a domain-I→domain-II transformation began to be evident near E=3 kV/cm. An abrupt decrease of R_d to a value of 0.159 was then observed over a modest field range of $3.5 \leq E \leq 4$ kV/cm. The abrupt nature of this decrease indicates a burst of domain reorientations. It should also be noted that this decrease was irreversible, since the changes in R_d remained stable upon removal of E (see Fig. 3.9b). Thus, a large remnant strain change can be anticipated. Interestingly, the value of R_d did not change with reversal of the sign of E, indicating that polarization was confined to the four domain-II directions after the initial reorientation, and that subsequently only 180° domain switching was induced by E.

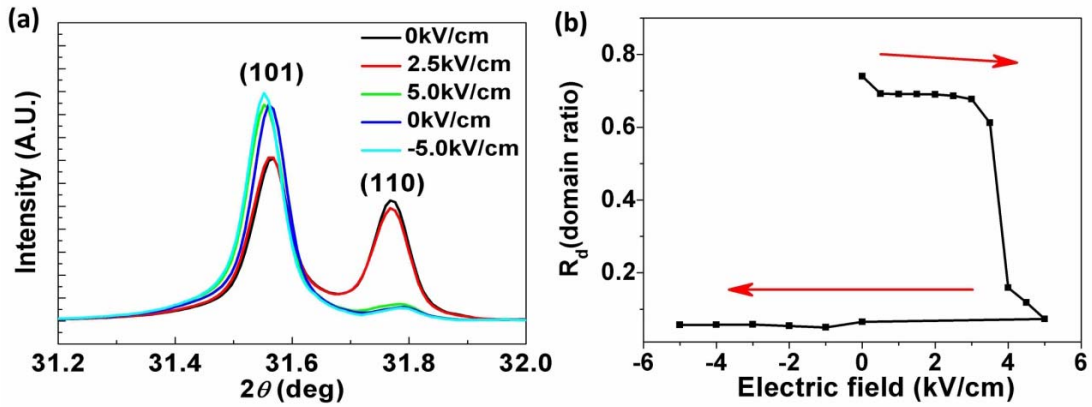

Figure 3.9. (a) XRD of PMN-38PT substrate under different electric fields; (b) electric field-dependence of domain-I/domain-II ratio, calculated by comparisons of the diffraction intensities of the (101) and (110) peaks.

3.2.4 E-field and thermal modulation of magnetic coercive field

Figure 3.10 shows the M-H loops of a CFO/PMN-PT heterostructure under various applied electric fields. CFO is known to have a negative magnetostriction

along both <011> and <100>. Along $\vec{x}$, a tensile strain was induced by E in PMN-PT. As a consequence, magnetic domain switching became easier as demonstrated by reductions in H_c and M_r with increasing E. Along $\vec{y}$, a compressive strain was induced in the substrate by E, which was then transmitted to the CFO film. Accordingly, magnetic domain switching became more difficult, as demonstrated by increases in both H_c and M_r with increasing E. Figure 3(d) summarizes the values of the remnant-to-saturation magnetization ratio, $R_M=M_r/M_s$, as a function of E applied out-of-plane E. For the CFO film, the value of the ratio is R_M=0.16 in the original state along $\vec{y}$, which increased to R_M≈0.4 for E>4 kV/cm. The value of R_M was largest along $\vec{x}$ with R=0.51 in the initial state, which then decreased to R_M<0.4 for E>5kV/cm. The value of R_M along $\vec{y}$ became larger than that along $\vec{x}$ for E>5kV/cm, indicating a rotation of the magnetic easy axis from $\vec{x}$ to $\vec{y}$. Moreover, it is obvious that the change of R_M along $\vec{y}$ was much larger than that along $\vec{x}$. This is in accordance with the calculated larger strain value along $\vec{y}$ than along $\vec{x}$: i.e. |-1.3%|>|0.667|. The value of R_M along $\vec{z}$ was small over the entire measurement range of -8<E<8kV/cm, reflecting the difficulty in altering magnetic shape anisotropy due to the CFO thin film architecture. Finally, for all three orientations, the changes in the R_M values were stable after removal of E.

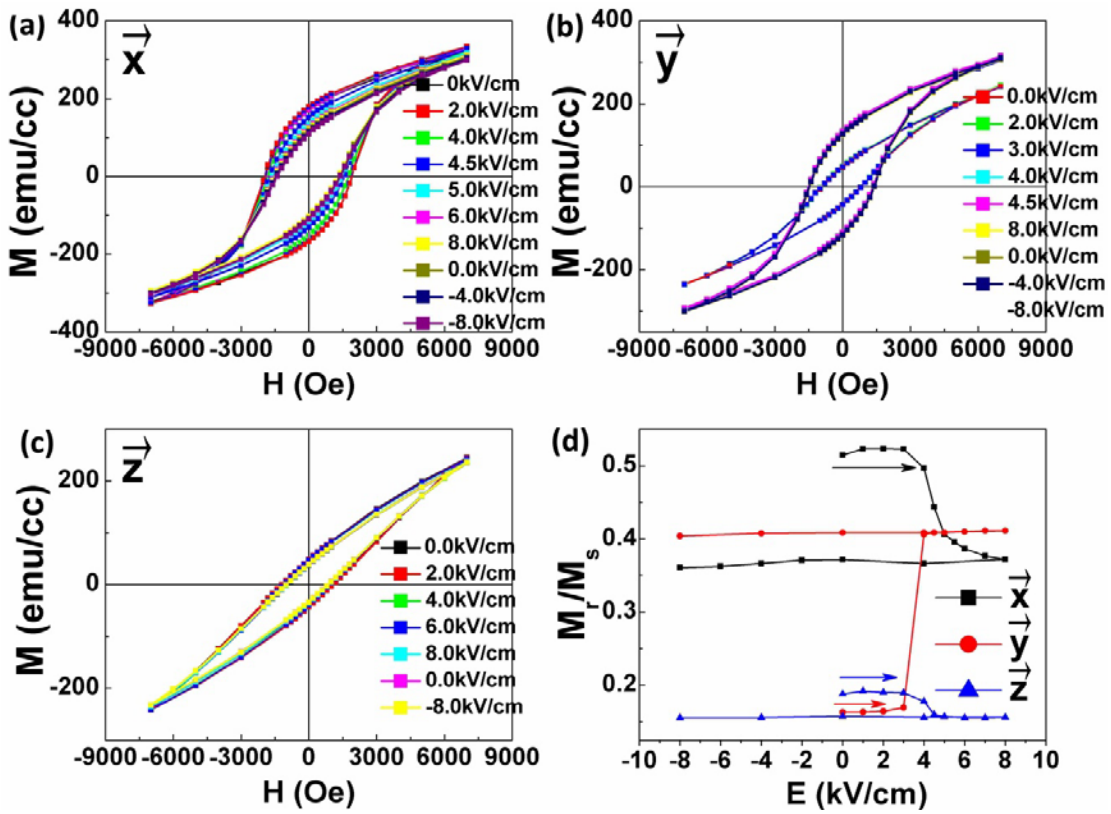

Figure 3.10. M-H loops of CFO/PMN-PT under different *E* along $\vec{x}$ (a), $\vec{y}$ (b), and $\vec{z}$ (c); (d) M_r/M_s ratio as a function of *E*.

Figure 3.11 shows the evolution of H_c with increasing E for $0<E<8$ kV/cm. The value of H_c along $\vec{x}$ decreased from 1.9 to 1.4 kOe; along $\vec{y}$, it increased from 0.8 to 1.4 kOe; and along $\vec{z}$, it decreased from 1.1 to 0.9 kOe. Please note that the change in the value of H_c along $\vec{y}$ (ΔH_c=1.4-0.8=0.6kOe) was larger than that along $\vec{x}$ (ΔH_c=1.9-1.4=0.5kOe). This finding in consistent with both larger E-induced strains and M_r/M_s ratio changes along $\vec{y}$ (see Fig.3.10d). In addition, the changes in H_c were irreversible upon removal of E along all three directions, indicating stable remnant changes.

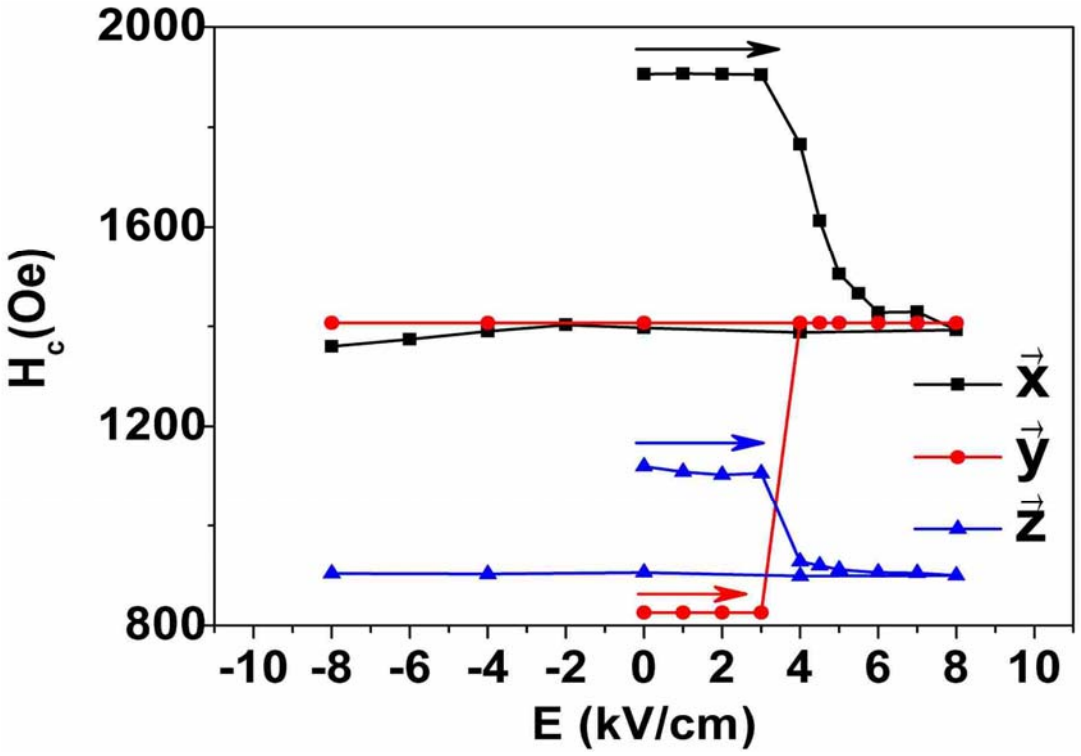

Figure 3.11. Magnetic coercive field of the CFO film under different E along $\vec{x}$, $\vec{y}$, and $\vec{z}$ directions;

Figure 3.12 illustrates the controllability of H_c for different poling and thermal annealing conditions. Along $\vec{y}$, the value of H_c was 870 Oe for the as-grown CFO/PMN-PT heterostructure, which then increased to 1380 Oe after poling of the substrate. The heterostructure was then annealed at a range of temperatures (T_a) and the value of H_c was remeasured. For $T_a \leq 420$ K, H_c remained stable. However, the original value of H_c was recovered after annealing at 470 K, which was linked to the recovery of the unpoled substrate condition. The Curie temperature of the PMN-38PT substrate was $T_c \approx 450$ K, as determined by dielectric constant data as a function of temperature. Thus, it is reasonable to conclude that the original value of H_c was not recovered until heating above the T→C phase transformation of the substrate. This

temperature of T_a=470K required for H_c recovery in the CFO/PMN-PT heterostructure is notably lower than that previously required for other heat-assisted magnetic recording (HAMR) medias: e.g., $CoPt_3$ (600K), FePt (750K), FePd (760K) and CoPt (840K).[91] Accordingly, the coercive field of a CFO/PMN-PT heterostructure might easily be recovered by a HAMR writing head. As an example, consider a bit recorded along $\vec{x}$ where CFO has large values of H_c and M_r; in such a case the original magnetic state is quite stable. During writing, the local value of H_c would be notably decreased due to a field-induced strain in the substrate; thus, a small magnetic field could switch the magnetization. A laser could then be used to heat the switched area, recovering the large H_c and M_r values. This process would facilitate high-density magnetic recording and ease the read-out procedure.

There are two main advantages of the proposed *E*-controlled-H_c magnetic recording (EHMR) compared with traditional HAMR. The first is the lower energy consumption due to the smaller Curie temperature of piezoelectric substrate compared with that of the ferromagnetic thin films (470K< 600K). The second is the smaller writing time due to the fact that the recording unit cells always remain in the ferromagnetic state—meaning that the writing magnetic field does not have to be retained during the cooling process. In contrast, in traditional HAMR the writing magnetic field has to be stabilized until the memory cell transfers from the paramagnetic to the ferromagnetic state. Given important economic factors, it makes sense to utilize piezoelectric thin films instead of piezoelectric single-crystal substrates in EHMR. In their study of $PbTiO_3$ (PTO) thin films on $DyScO_3$ substrates, Catalan et al. described ferromagnetic domain size of ~50 nm.[106] Based on our previous results about the relationship of domain size with the PMN-PT concentration,[107] it is highly possible that we can obtain much smaller ferroelastic

domains in PMN-38PT films compared with pure PTO films. Similarly, Xu et al. used neutron scattering to study the correlation length of polar nanoregions where size averaging less than 10 nm was observed.[108] These studies point to the fact that recording density is confined by the sizeable electrode, but not by the domain size of the ferroelastic domains. A recording density well exceeding 6 Tb/inch^2 can be achieved if each single domain (10nm×10nm) can be used to record one bit of information.

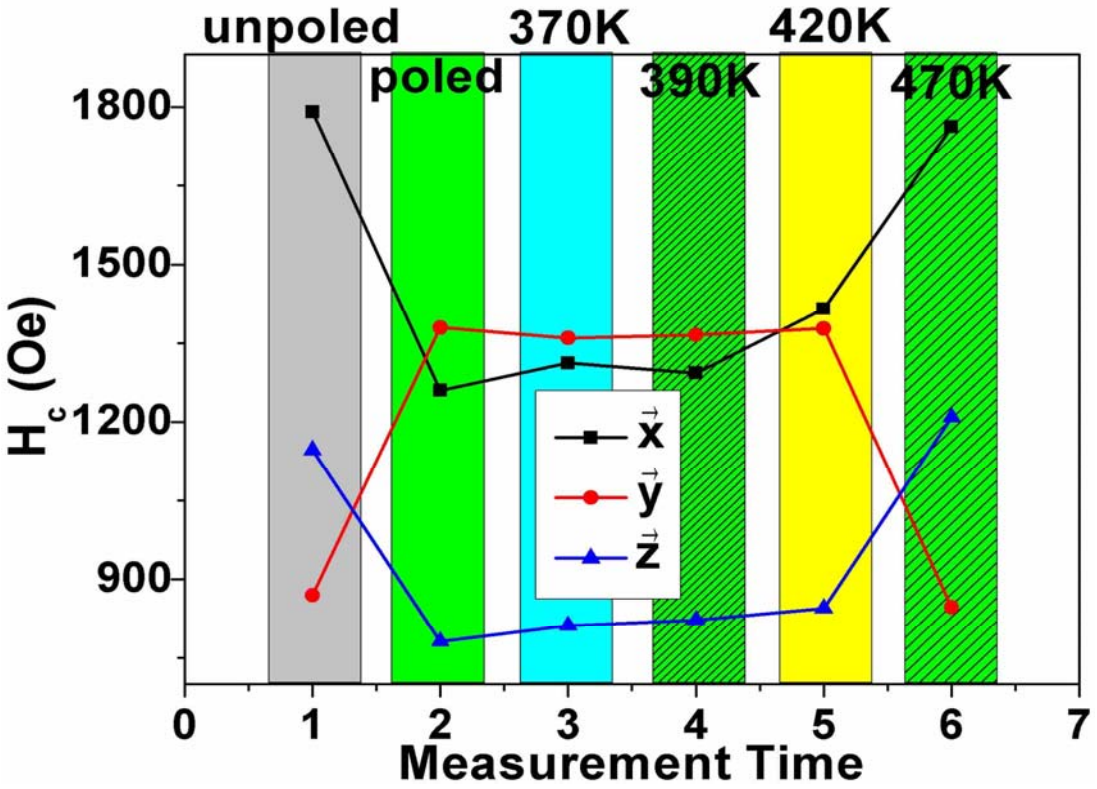

Figure 3.12. Electric field and thermal annealing dependence of H_c along different directions.

Table 3.2 lists values for magnetic coercive field changes (ΔH_c) under different electric fields in various ferromagnetic/ferroelectric heterostructures.[59, 109-113] The largest value of ΔH_c previously reported was 50 Oe for Fe_3O_4/PZN-PT.[109] The value for CFO/PMN-38PT reported here is more than 10 times larger—namely, 580 Oe.

Three reasons are proposed for the abnormally large value of ΔH_c for CFO/PMN-38PT: (i) the magnetostriction of CFO is more than 10 times larger than those of previously-described ferromagnetic materials; (ii) the tetragonal PMN-38PT provides much larger strain compared with that of BTO or rhombohedral PMN-PT substrates; and (iii) high-temperature deposition engenders an epitaxial interface between CFO and PMN-PT, which assures an effective elastic strain transfer from substrate to thin film.

Table 3.2. Magnetic coercive field tunability in various ferromagnetic/ferroelectric heterostructures.

Thin Film	Ni	Ni	$Ni_{80}Fe_{20}$	Fe_3O_4	Fe_3O_4	CFO
Substrate	BTO	PMN-PT	PZN-PT	PZN-PT	PMN-PT	PMN-PT
magnetostriction (ppm)	-32.9	-32.9	-10.7	20	28	-590
thickness (nm)	10	10	10/100	~500	~900	~400
ΔH_c(Oe)	~10	~30	~13/~0	~50	<30	580

3.2.5 Summary

In summary, CFO/PMN-38PT epitaxial magnetoelectric heterostructures were fabricated. Subsequently, electric fields were applied along the out-of-plane direction, which induced a uniaxial strain in PMN-38PT via polarization reorientation. This strain was then elastically transferred to the CFO films. A significant and stable change in the magnetic coercive field of $\Delta H_c \approx$ 580 Oe was found along the in-plane ⟨100⟩ upon removal of E. The original condition and properties of the heterostructures were recovered after annealing at 470 K. These findings demonstrate effective electric and thermal control of the magnetic coercive field, which could be exploited for potential applications in high density magnetic recording and spintronics.

3.3 ME effect in CFO film on <001>-oriented T-phase PMN-PT

3.3.1 Introduction

Eerenstein et al. reported the growth of epitaxial $La_{0.66}Sr_{0.33}MnO_3$(LSMO) thin films deposited on single-crystal $BaTiO_3$ (BTO) substrates, wherein they observed sizable magnetization changes near the R→O phase transition.[43] In a similar study, Yang et al. deposited epitaxial CFO thin films on PMN-PT substrates to study magnetization changes under different electric fields; in response, the researchers observed a converse ME coupling coefficient of $\alpha=\mu_0 dM/dE=3.2\times10^{-8}sm^{-1}$.[69] Thiele et al. reported the growth of LSMO on a PMN-PT substrate and obtained a strain-mediated converse ME coupling coefficient of $\sim6\times10^{-8}sm^{-1}$.[114] Despite the variety of materials, all of these studies focused on the overall magnetization change due to a strain introduced by an external electric field (E) on the piezoelectric substrate, or the switching of magnetization near a phase transition. Local magnetization changes under E are potentially more important for applications.

In this phase of the study, we deposited epitaxial CFO thin films on single-crystal 60PMN-40PT by pulsed laser deposition (PLD) in order to study the domain rotation-induced strain effect on the magnetic properties of CFO, as well as the corresponding ME coupling effects.

3.3.2 Electric field-induced domain rotation and strain in CFO film on (001)-oriented PMN-PT substrate

Figure 3.13 show the reciprocal space mappings (RSM) of CFO on (001) PMN-PT substrates before and after application of E, respectively. In the unpoled condition, the PMN-PT substrate had a tetragonal (T) structure, and showed a multi-domain (*a*- and *c*-) configuration. The polarization direction can lie arbitrarily

between in-plane and out-of-plane directions. Thus, in the out-of-plane direction we could see an equal amount of a-domains and c-domains. Accordingly, in Figure 3.13(a), the *a*-and *c*-domains can be seen to exhibit similar diffraction intensities due to equal populations.

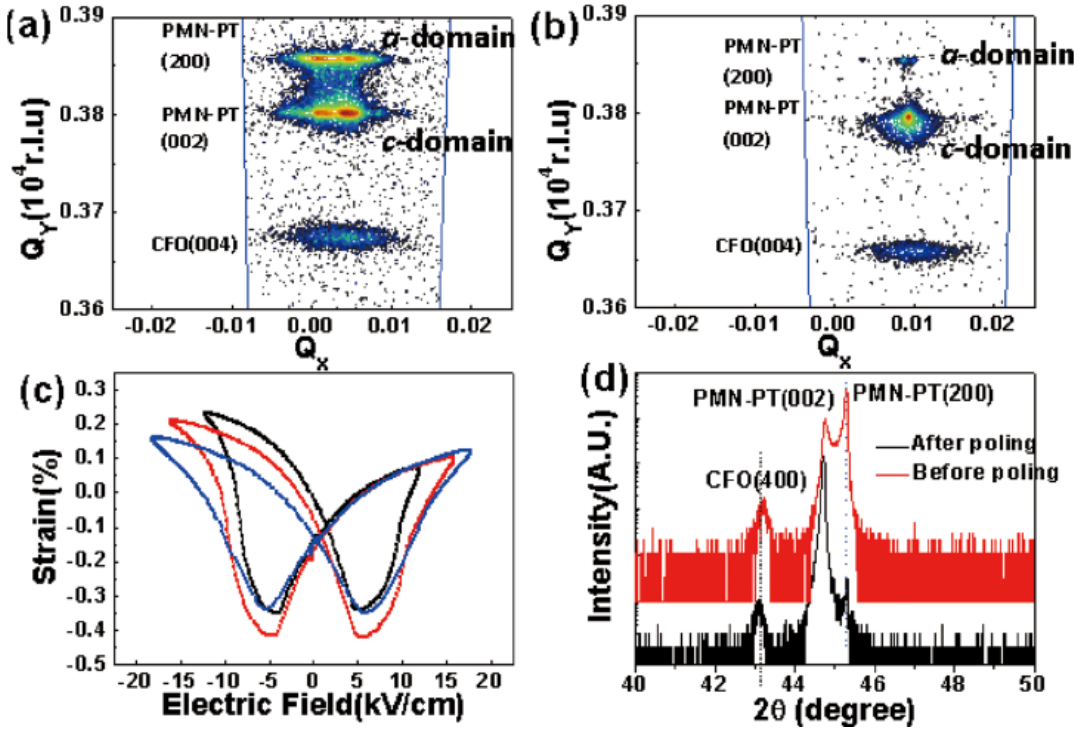

Figure 3.13. (a), (b) Mesh scan of CFO on PMN-PT with different ferroelectric domain configurations. (c) Strain-E curve of piezoelectric PMN-PT substrate. (d) XRD line scans of theCFO/PMN-PT before and after electric field poling.

We then applied E_p=15 kV/cm along the vertical direction through the substrate, poling the sample and rotating the *a*-domains by 90°, thereby transforming them into *c*-domains. The coercive electric filed (E_c) of the PMN-PT substrate was about 5 kV/cm, and the electric field E_p we applied was 3 times larger than E_c. In this condition, E_p produced two effects on the ferroelectric domains First, E_p was able to induce a 180° domain rotation in the c-domains, aligning all the c-domains in the same polarization direction with E_p. Second, E_p was able to rotate most of the

a-domains from the in-plane to the out-of-plane direction, resulting in a quasi single c-domain condition in the PMN-PT substrate. This domain transformation process was clearly evidenced by a decreased *a*-domain peak intensity as evidenced in Figure 3.13(b); the diffraction from the a-domains formed a small area with a very weak intensity. This change in the RSM demonstrates that after poling, most of the domains rotated so that their polarization axes were along the out-of-plane direction in accordance with the E_p direction. The crystal lattice parameters of PMN-PT were determined to be (a_t, c_t)=(4.032, 4.083), where the maximum strain induced by the domain reorientation was $\varepsilon=(a-c)/a=0.0126$. Next, we measured the maximum induced stain under an AC electric field (ε-E response), as shown in Figure 3.13(c). In this case, the maximum induced strain was about 0.006 under an AC electric field of 15 kV/cm.

The induced strain in the PMN-PT substrate could be transferred to the epitaxially-grown CFO thin films on top, thus changing the crystal lattice parameters and spin state of the CFO. Figure 3.13(d) shows XRD line scans for the CFO/PMN-PT heterostructures. The PMN-PT substrate had a tetragonal structure, and hence both (002) and (200) diffraction peaks for this substrate were evident. In addition, we identified a CFO (400) diffraction peak, indicating a epitaxial growth mechanism for CFO on a single-crystal PMN-PT substrate. Comparison of these diffraction peaks before and after poling revealed two trends: (i) an obvious left-shift of the CFO peaks after poling due to strain from PMN-PT; and (ii) a dramatically-decreased intensity for the PMN-PT (200) peak, corresponding to the *a*- to *c*-domain transformation.

3.3.3 Electric-controlled magnetic response through interface elastic strain coupling

Figure 3.14(a) shows an AFM topography image of the PMN-PT substrate, revealing a roughness of only about 5 nm after polishing. Figure 3.14(b) shows a contrast PFM image, where the center square was poled. The surrounding unpoled area reveals stripe-like domains with a width of about 100 nm that are evenly distributed throughout the PMN-PT. The bright and dark contrast areas correspond to regions having different polarization orientations for the vertically-aligned *c*-domains. After poling of the center area (4μm×4μm) with E=5 kV/cm, one can see that the square is entirely dark, demonstrating the presence of a single *c*-domain state.

Figure 3.14(c) depicts an AFM topography image of the CFO film on PMN-PT, revealing a smooth surface with CFO nanostructures smaller than 100 nm. We then poled the center area (5μm×5μm) of the CFO/PMN-PT heterostructure and obtained MFM images that revealed obvious contrast differences between poled and unpoled areas. The MFM probe tip was magnetized in the up direction, and the sample was magnetized in the down direction: thus, the higher the out-of-plane remnant magnetization, the lighter the contrast. In the center poled area, the transformation of the *a*- to *c*-domains applies a compressive strain to the CFO film. Since CFO has a negative magnetostriction, its magnetic moments instinctively lay in the in-plane direction under compressive strain, resulting in decreased remnant magnetization along the out-of-plane direction. The darkened area in the center of the MFM image clearly demonstrates this compressive strain-induced decrease in the remnant magnetization in the CFO layer.

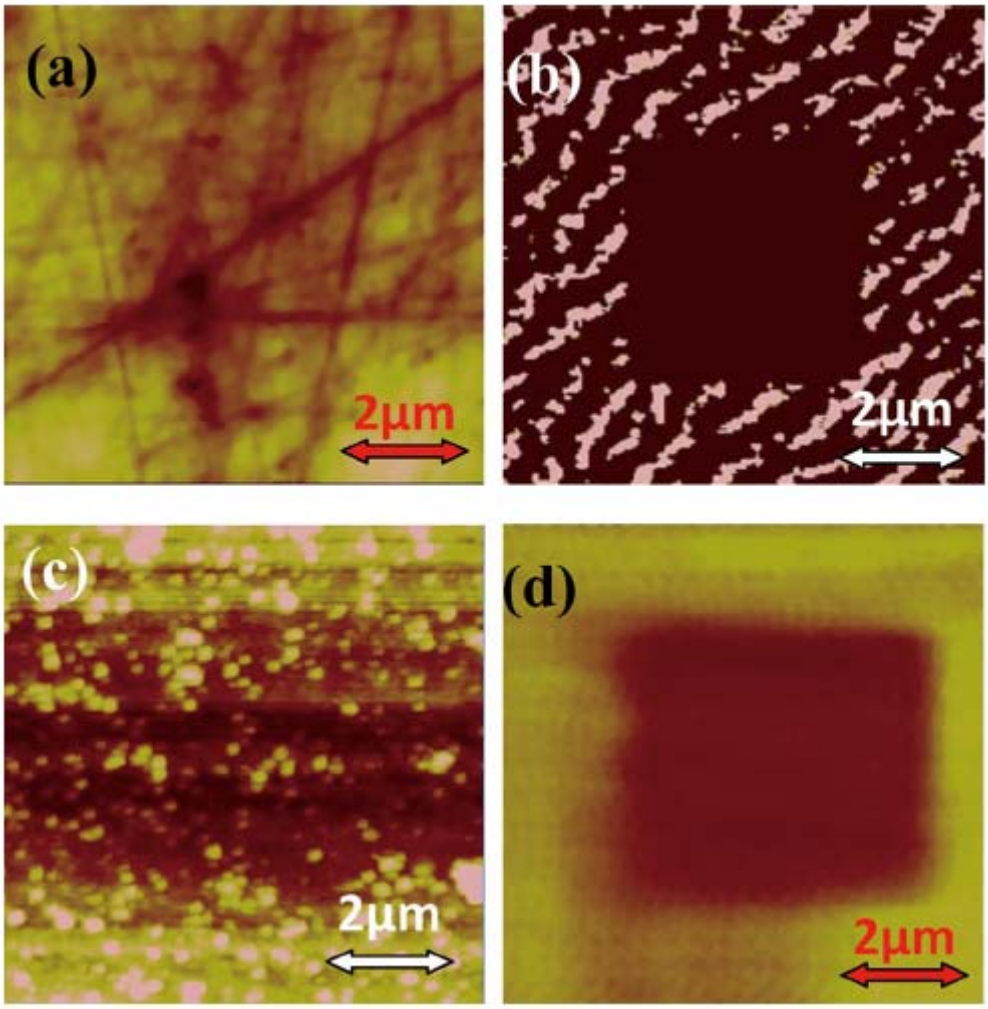

Figure 3.14. (a) Topographic AFM image of PMN-PT single-crystal substrate; (b) PFM measurement of domain rotation in PMN-PT; (c) Topographic AFM image of CFO thin film on PMN-PT; (d) MFM measurement of the strain effect on the magnetic response in the poled area.

Quantitative analysis of the strain-induced magnetization anisotropy change was then performed using VSM measurements. Figure 3.15(a) shows the in-plane magnetic hysteresis loops of the sample before and after the *a*- to *c*-domain transformation. This ferroelectric domain transformation in the PMN-PT substrate resulted in a 220% increase in remnant magnetization along the in-plane direction. Converely, along the out-of-plane direction the M-H loops (Figure 3.15(b)) exhibited

decreased remnant (67%) and saturation (72%) magnetizations after the ferroelectric *a*- to *c*-domain transformation. This decrease in remnant magnetization along the out-of-plane direction was also confirmed by the MFM image (Figure 3.15(d)). We should note that the saturation magnetization should be equal to the spontaneous magnetization (M_s) in a ferromagnet, and that M_s can be notably affected by strain conditions.[69, 114] Thus, the significant strain induced during domain rotation resulted in a dramatic change in both remnant and saturation magnetization values. To eliminate the possible charging effect from the ordering of electric dipoles in the PMN-PT substrate during VSM measurements, we performed similar measurements for a pure PMN-PT substrate without a deposited CFO layer: no magnetization hysteresis loop was found for either the single- or multi-domain PMN-PT.

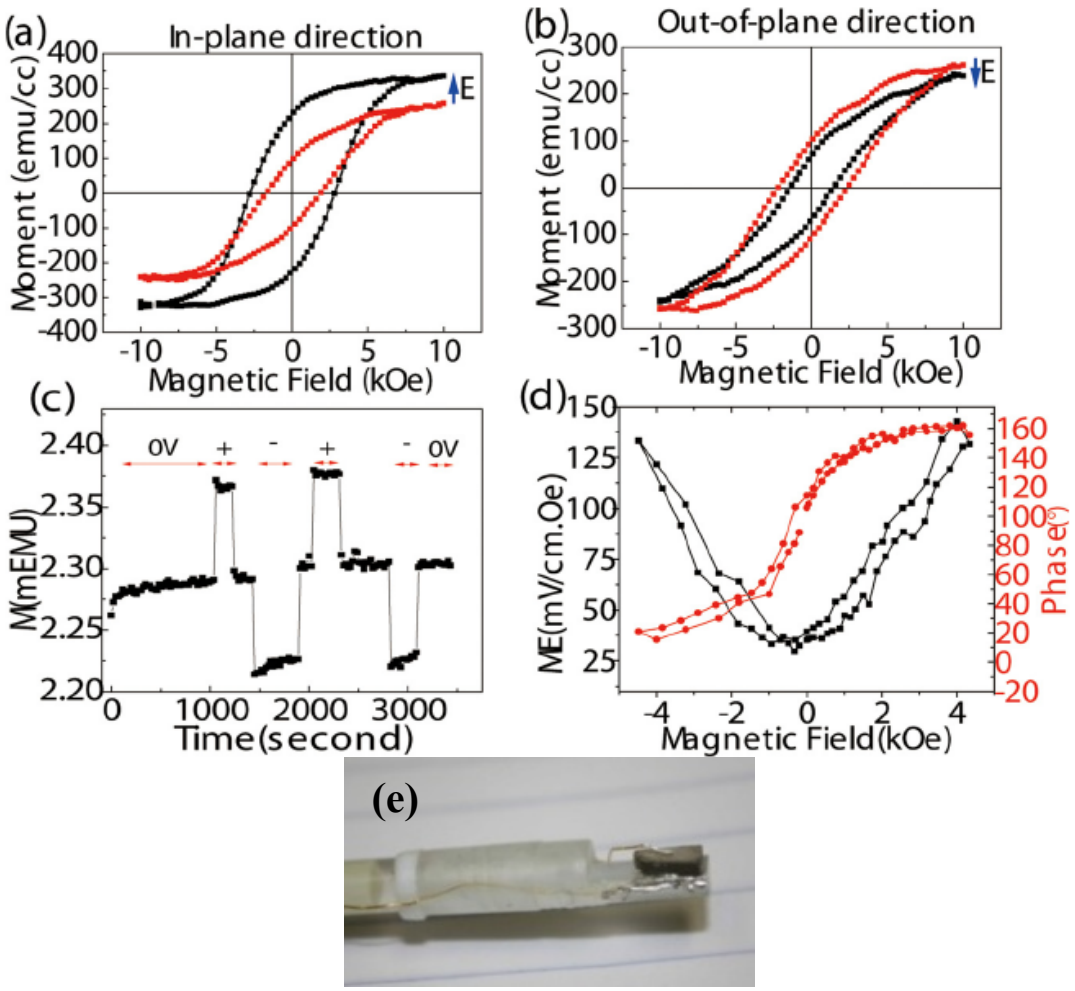

Figure 3.15. (a), (b) Magnetic hysteresis loops of CFO thin films with different domain configuration in the in-plane direction and out-of-plane directions, respectively; (c) magnetization step change under square wave electric voltage (±50V); (d) voltage ME coupling coefficient; and (e) set up of VSM holder for electric field application.

Next, we fixed the sample on the VSM holder and applied an electric field to obtain the magnetization-time measurement, as shown in Figure 3.15(e). The converse ME coefficient of the CFO/PMN-PT heterostructures was then measured (Figure 3.15(c)). Square wave 50 volt pulses (E=1kV/cm) were applied across the PMN-PT

substrate, and a change in magnetization of ΔM≈0.1mEMU was measured. The converse ME coefficient $\alpha_{ME}=\mu_0(\partial M/\partial E)H$ was then calculated to be $\alpha_{ME}=1\times10^{-7}$ sm^{-1} for the CFO layers. This is a much higher value than the $\alpha_{ME}=2.3\times10^{-8}$ sm^{-1} previously reported for LSMO films on $BaTiO_3$ single crystals near an induced R→O transformation.[43] Our measured value is comparable to the analogous value for bulk laminate ME composites (4×10^{-7} sm^{-1}).[54] More importantly, it must be stressed that our giant converse ME effect was achieved by means of a reversible electric field, and not via a phase transition at a particular temperature.

Finally, we performed direct magneto-electric measurements of α_{ME}, as shown in Figure 4.14(d), following previously-reported techniques.[104] A magnet was used as the dc magnetic bias field (H_{dc}), after which a 10kHz ac magnetic field H_{ac} was applied along the long axis of the heterostructure. This changing magnetic field resulted in an induced strain via magnetostriction along the CFO thin film. The induced strain was then transmitted to the PMN-PT substrate, resulting in an output voltage that was detected by a lock-in amplifier. Figure 4.14(d) shows α_{ME} as a function of H_{dc}. A maximum value of α_{ME}≈140 mV/cm-Oe was found. The shape of the ME coupling coefficient curve is different from that of the NFO/PZT bulk ceramic material, which exhibited a saturation of α_{ME}near 100 Oe, above which point α_{ME} decreased with further increasing H_{dc}. It is well known that magnetization is determined by magnetic domains, and the domain size and configuration are notably influenced by the stress state of the material.[115, 116] Thus, strained CFO epitaxial thin films may require a higher applied H_{dc} to reach saturation value in comparison to bulk ceramics.

In summary, epitaxial CFO thin films were grown on PMN-PT substrates. Resulting PFM images revealed domain control in precise positions under an external electric field. The strain effect on the magnetic properties of the CFO thin films was

then measured by MFM; results showed the possibility of writing on CFO thin films with an electric field by a MFM probe tip. Comparison of the M-H loops of the multi-domain and the poled single-domain samples showed dramatic changes in the magnetic anisotropy. Specifically, compressive strain decreased the magnetization in the out-of-plane direction, and increased it along the in-plane direction. Finally, both converse and direct ME measurement showed huge ME coupling effects.

3.4 Future work about ferromagnetic thin films on piezoelectric substrates

Single-crystal PMN-PT shows the largest piezoelectric coefficient, making it an optimal substrate on which to apply a controllable strain in the epitaxial thin film on top. More importantly, the lattice mismatch between PMN-PT and most of ferromagnetic ferrites is moderate. Therefore, it is possible to grow various ferromagnetic thin films on a PMN-PT substrate. Both phase transformation and ferroelectric polarization reorientation can induce large strain in epitaxial ferromagnetic thin films. PMN-PT single crystals show a phase sequence of R→O→M→T with increasing concentrations of $PbTiO_3$. This relationship means that different types of electric field-induced strain can be obtained based on the intrinsic phase configuration and specific orientation of the PMN-PT single crystals.

Two types of ferromagnetic materials can be deposited on PMN-PT with different possible applications:

1. Ferrites with high resistivity: $CoFe_2O_4$, $NiFe_2O_4$, and MFO, for example. The huge tunability of the magnetic coercive field ensures a significant change in the ferromagnetic resonance frequency (FMR). Electric field-controlled FMR can be used in various microwave devices. Moreover, the high resistivity of the ferrites would help to solve the eddy current problem in microwave devices.

2. Ferromagnetic alloys: FeGa, CoFe, and NiFe, for example. Our group has investigated the growth of FeGa/PMN-PT magnetoelectric heterostructures. Despite the fact that the large crystal lattice mismatch hindered the epitaxial growth mechanism, dramatic magnetoelectric coupling can still be observed. Through careful selection of alloys with appropriate lattice parameters, it is possible to grow epitaxial ferromagnetic alloys on perovskite substrates, e.g. FeCo/MgO.[117] One should note that PMN-PT and MgO have very similar crystal lattice parameters, making it highly possible to grow epitaxial FeCo on PMN-PT substrates. The small magnetic coercive field, in addition to the larger squareness of the magnetic hysteresis loop of specific ferromagnetic alloys, enhances the likelihood of using these materials in magnetic recording devices.

Chapter 4 Phase Architecture and Magnetic Anisotropy in BFO-CFO Films

Controllable magnetic anisotropy is desirable for the fabrication of high-density magnetic memory. The hard magnetic material CFO has been studied in detail due to its high coercivity (5400 Oe) and large magnetic anisotropy, as well as high magnetostriction. Another important property of CFO is that it can be grown epitaxially together with perovskite-structured phases due to fairly close lattice matching, forming well-defined self-assembled structures with CFO nano-pillars embedded in a perovskite matrix. These self-assembled nanostructures allow much larger interfacial areas between the ferromagnetic and ferroelectric phases, thereby promising much larger magnetoelectric (ME) coupling effects, which is ultimately realized through interfacial elastic strain coupling between the two phases. In recent years, the interest in self-assembled BFO-CFO materials has increased due to their promising properties. Thus, a better understanding of them is crucial to opening new paths for the development of highly-efficient magnetic and magneto-electric materials and devices. However, a thorough analysis of magnetic anisotropy and exact determination of its origin with respect to strain, crystal orientation and shape is not yet available. To help fill this research gap, we conducted a study whereby we deposited BFO-CFO with different phase architectures on differently-oriented STO substrates and analyzed their shape, strain, and magnetocrystalline anisotropies in details.

4.1 Orientation-related phase architectures and crystal structure characterization

Figure 4.1 shows the phase architectures of BFO-CFO grown on differently-oriented STO substrates. CFO has a converse spinel crystal structure,

whereas BFO is a rhombohedrally-distorted perovskite. The large crystal lattice mismatch (7.4%) between CFO and STO induces a significant surface energy difference. Moreover, a lack of "wetting" on the STO drives the CFO to form nanopillars embedded in a coherent BFO matrix, which has a close lattice constant to that of STO. SEM images in Figure 4.1(c) reveal the morphological features of square, stripe and triangular nanostructured CFO on (001)-, (110)-, and (111)-oriented STO substrates, respectively.

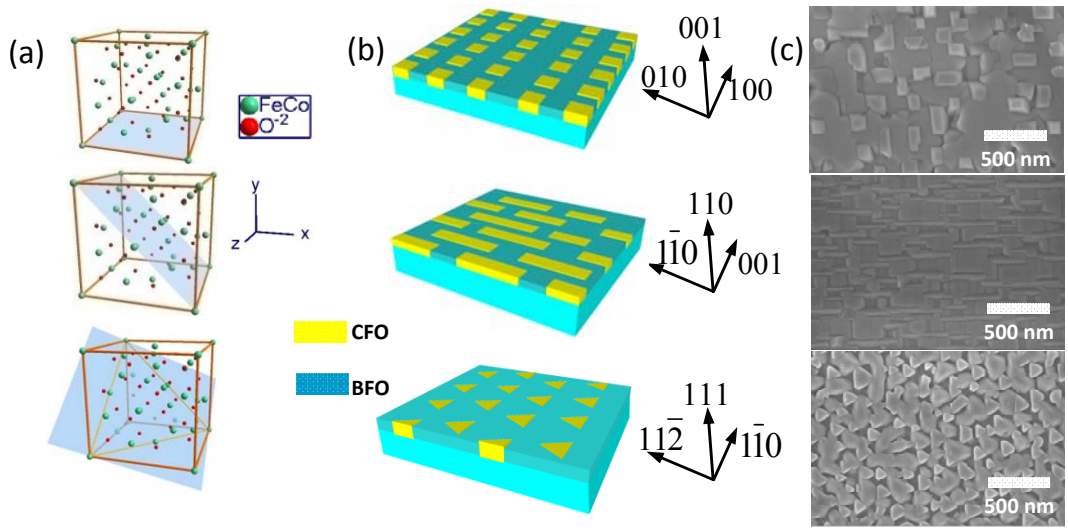

Figure 4.1. (a) Crystal structure of converse spinel CFO with the (001), (110) and (111) planes entitled. (b) Schematic of phase architectures for differently-oriented BFO-CFO thin films on STO substrates. (c) SEM of BFO-CFO with square, stripe and triangular CFO features.

We then examined the out-of-plane crystallographic orientation of the BFO-CFO composite thin films on differently-oriented STO substrate by XRD θ-2θ scans, as shown in Figure 4.2. Diffraction peaks of atomic planes in accordance with the orientation of the STO substrate were observed. These consistent diffraction peaks indicate an epitaxial growth mechanism, as well as evidence of phase separation.

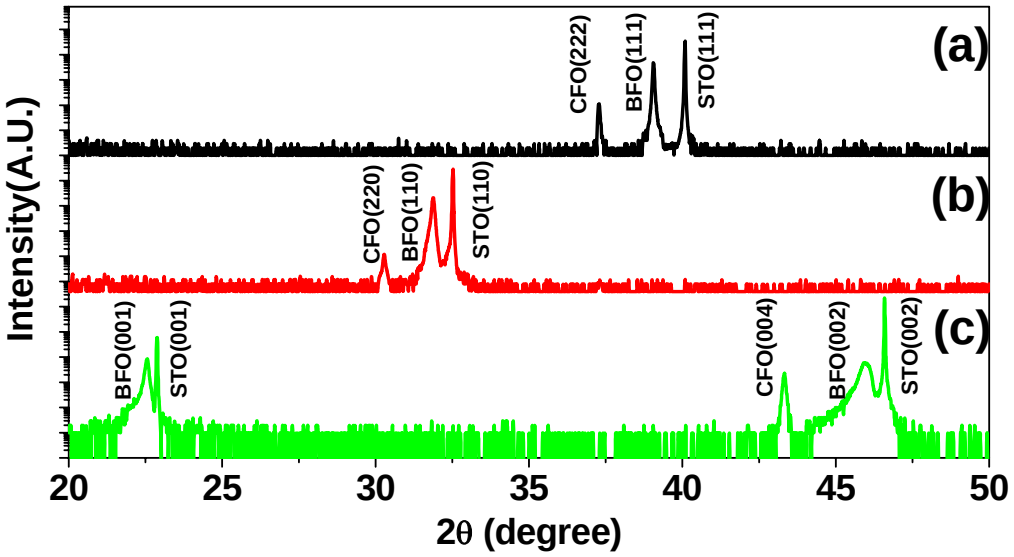

Figure 4.2. (a-c) Out-of-plane X-ray diffraction line scan of BFO-CFO on (111), (110) and (100) STO substrates.

4.2 Competition of magnetic strain and shape anisotropies

Figure 4.3 depicts how the magnetic properties of BFO-CFO on (001) STO change with dimensions. A magnetic force microscopy (MFM) probe was magnetized in the spin-up direction. The black and white areas in the MFM images demonstrate spin-up and spin-down magnetic domains, indicating a perpendicular push-pull magnetic moment coupling between the probe and the CFO nanopillars. First, we studied the magnetic response in a BFO-CFO film with a thickness of 500 nm, where the diameter of the CFO nanopillars was 100 nm, i.e., a height-to-diameter ratio of R≈5. The thin film thickness was determined by direct measurement of the cross-sectional SEM images. We examined the lateral size of the CFO nanopillars in the BFO-CFO thin films by cutting the sample with a focused ion beam, after which a uniform width could be observed.[61] The aspect ratio can therefore be calculated by dividing the thickness by the lateral size of the CFO features. The shape anisotropy

energy density of a CFO cylinder with an aspect ratio of 5:1 and a demagnetization factor of N_z=0.04 can be estimated as $E_{shape}= 2\pi(N_x-N_z)M_s^2= 4.2\times10^5$ erg/cm^3, where $N_x= (1-N_z)/2$.[118] The shape anisotropy field was calculated to be $H_{shape}= 2E_{shape}/M_s$= 1.9 kOe. Accordingly, the CFO nanopillars should have a pronounced out-of-plane magnetic easy axis. Black and white square areas of similar proportion can be seen in the MFM image in Figure 4.3(a), indicating a near-random distribution of up and down magnetizations for the as-prepared BFO-CFO. Then, a perpendicular 5 kOe magnetic field was applied along both the up and down directions. Changes in the MFM image were used to study the remnant magnetization in each CFO nanopillar. Figure 4.3(b) shows a MFM image of CFO in the down-magnetized state. Uniform white rectangles of size ~100 nm show that the CFO nanopillars are predominantly in a similar single domain state. A near-complete switching of the magnetization direction (from black to white) was observed in the square CFO areas under -5 kOe, as seen in the MFM images of Figure 4.3(c).

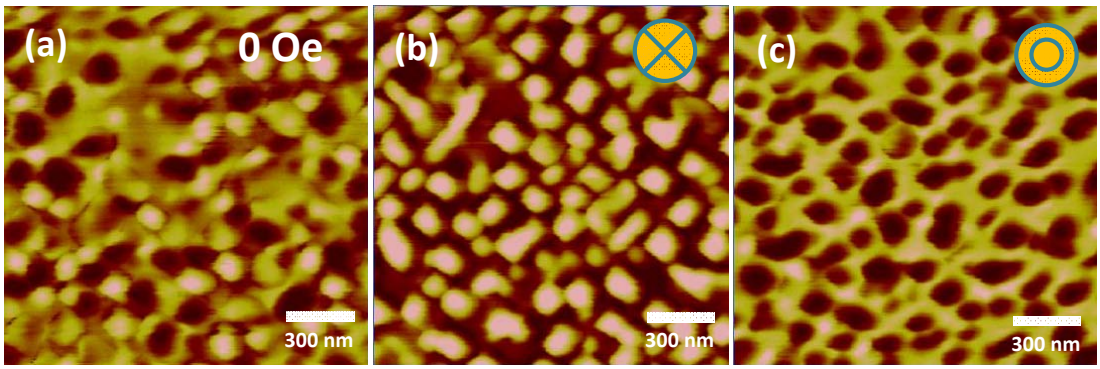

Figure 4.3. (a-c) Out-of-plane X-ray diffraction line scan of BFO-CFO on (111), (110) and (100) STO substrates.

To confirm that shape anisotropy is more significant than other effects in the BFO-CFO with large aspect ratio, we measured the M-H loops for different rotation angle (θ) from in-plane to out-of-plane directions. For CFO square pillars with a finite

length, the easy axis should be in the longest dimension direction due to shape anisotropy, as illustrated by the arrow in Figure 4.4. BFO-CFO films with thicknesses of 500 nm and 300 nm were selected, where the aspect ratio varied from R=5:1 to 3:1. Figures 4.4(a) and (b) show the evolution of the M-H loops as the measurement angle was rotated from the in-plane to out-of-plane directions for CFO nanopillars with aspects of 5:1 and 3:1, respectively. A large magnetic perpendicular shape anisotropy can be seen in the 500 nm BFO-CFO layer, where the remnant magnetization (M_r) in the out-of-plane direction was four times larger in comparison to the in-plane direction. The coercive field in the out-of-plane direction reached H_c=2.5 kOe, which was almost three times larger than the in-plane result (0.9kOe). The magnetic field was not sufficiently high to saturate the magnetization, so the coercive field difference H_{diff} =2.5-0.9 =1.6 kOe was smaller than the calculated anisotropy field (1.9kOe). The M-H loops for BFO-CFO with a smaller R (3:1) showed a weaker magnetic anisotropy. The remnant magnetizations (after normalization) were 0.28 and 0.11 in the OP and IP directions, respectively. The coercive fields were also much smaller: 1.5 kOe and 0.608 kOe for OP and IP directions, respectively. It is well known that the coercive field for single-domain magnetic nanostructure decreases rapidly as the size is decreased.[119-121] Therefore, the decrease in magnetic anisotropy and the coercive field when R was changed from 5:1 to 3:1 can be attributed to size and shape anisotropy effects, instead of the effects of strain anisotropy—principally because strain conditions should be identical for the BFO-CFO system.

Figure 4.4(c) also shows remnant magnetization as a function of the IP-to-OP rotation angle. For a square shape with a specific aspect ratio R, the longest distance should be along the direction indicated by the arrow this figure, where $\theta = \arctan(R)$. For a large R, the value of θ was very close to 90°. Thus, the 500 nm BFO-CFO thin

film had the highest remnant value of 0.6 along the OP direction. For a 300 nm BFO-CFO thin film with R=3:1, the easy axis angle is θ=arctan(3)=71° or 109°. Accordingly, the largest remnant values observed in the M-H loops occurred at θ=70° and 110°. These results unambiguously demonstrate that shape anisotropy is a predominant factor for BFO-CFO self-assembled nanostructures on (001) STO, where the easy axis direction can be rotated by tuning the aspect ratio of the CFO nanopillars.

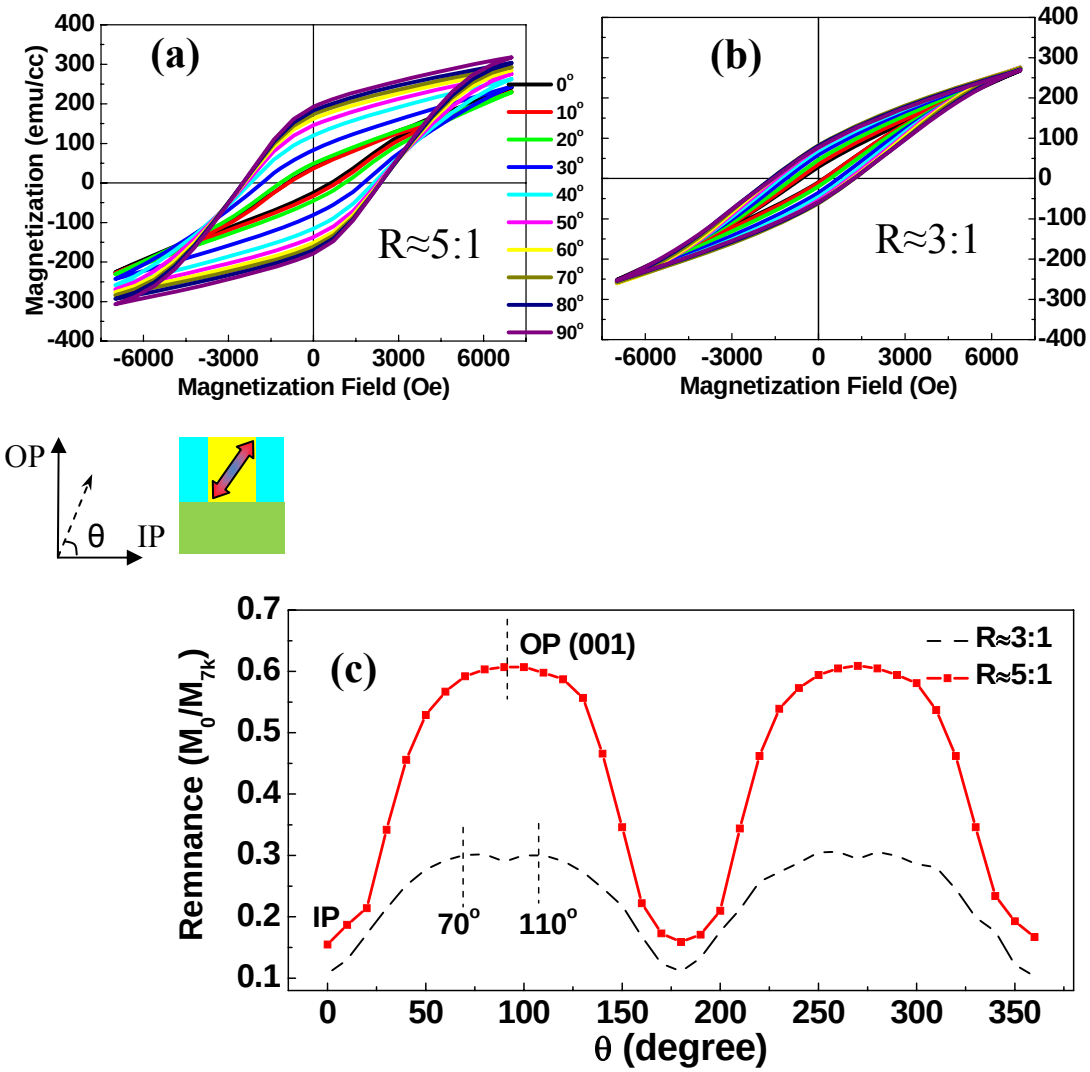

Figure 4.4. (a), (b) M-H loops for different measurement angles of CFO nanopillars with different aspect ratios. (c) Remnant magnetization as a function

of in-plane to out-of-plane rotation angle.

CFO has a large saturation magnetization, and thus the magnetic anisotropy is sensitive to the strain conditions of the CFO nanostructure. We studied strain relaxation as a function of film thickness, as llustrated in Figure 4.5(a). 200 nm CFO thin films on STO showed a (400) peak at 43.166°, which remained relatively stable as the thickness changed. This finding corresponds to a crystal lattice parameter of a_c= 8.3815 Å, which is slightly smaller than that of the bulk CFO. In BFO-CFO self-assembled thin films, CFO is confined by a compressive strain from the BFO matrix. This strain will relax as the thin film thickness increases. As the BFO-CFO thickness increased from 200 nm to 900 nm, the CFO diffraction peaks shifted from 43.215° to 43.185°, indicating a strain relaxation from 0.079% to 0.03%. The strain anisotropy energy density of BFO-CFO films of differing thicknesses was then compared with the comparative strain-induced results, as illustrated in Figure 4.5(c). The strain-induced anisotropy energy was larger for BFO-CFO with small aspect ratios. However, as film thickness increases, shape anisotropy will become increasingly important. Thus, we also measured the magnetic coercive field as a function of thickness, as shown in Figure 4.5(c). With increasing thickness, the strain effect from the BFO matrix relaxes; thus, the value of H_c should decrease if the strain effect is the only source of magnetic anisotropy in BFO-CFO. However, H_c increased from 1.2 to 2.53 and then to 3.4 kOe as the BFO-CFO thickness increased from 300nm to 500nm and then to 900nm due to the existence of the shape anisotropy effect.

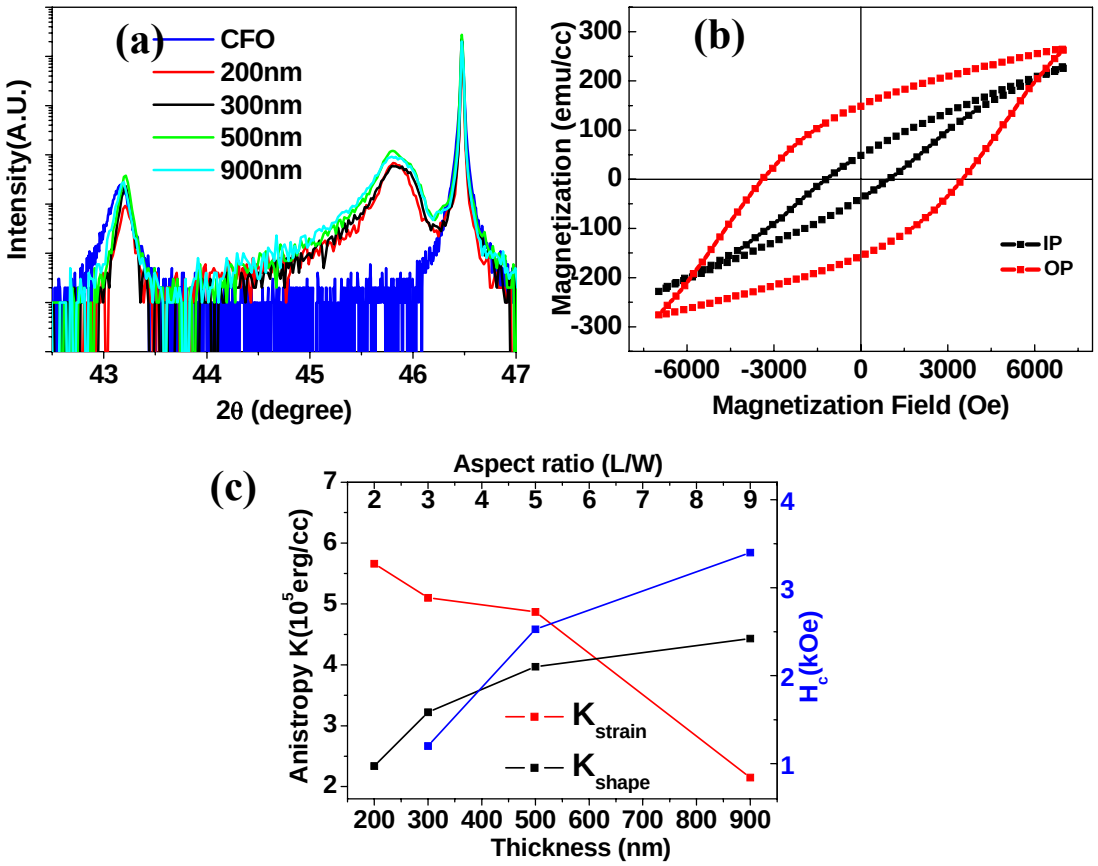

Figure 4.5. (a) X-ray line scan of pure CFO and BFO-CFO thin films with different thickness. (b) M-H loops for 900 nm BFO-CFO in IP and OP directions. (c) Comparison of strain- and shape-induced magnetic anisotropy energy density (K) and magnetic coercive field (H_c) as a function of BFO-CFO thickness.

Figure 4.6 shows the AFM and MFM images of BFO-CFO on (110) STO substrates, where the morphological features were aligned along the in-plane direction. The deposition temperature was set at 700°C, which is required for well-separated phase distribution, as well as related to the development of thermal dynamics. Both growth rate and deposition temperature can affect the size features of CFO nanostripes; specifically, faster growth rate and higher deposition temperature will produce CFO nanostripes with larger width and length values. Detailed CFO nanostructure

dimension control is described in our prior results.[122] The CFO phase formed as nanostripes with R≈5:1 that were oriented in the in-plane direction, with lengths of ~300 nm and widths of ~60 nm. Figure 4.6(a) illustrates an atomic force microscopy (AFM) topography that shows that the CFO nanostripes were slightly higher than the BFO matrix. The right-hand portion of this figure shows the corresponding MFM image, wherein a strong magnetic response was evident in the CFO phase, but not in the BFO matrix.

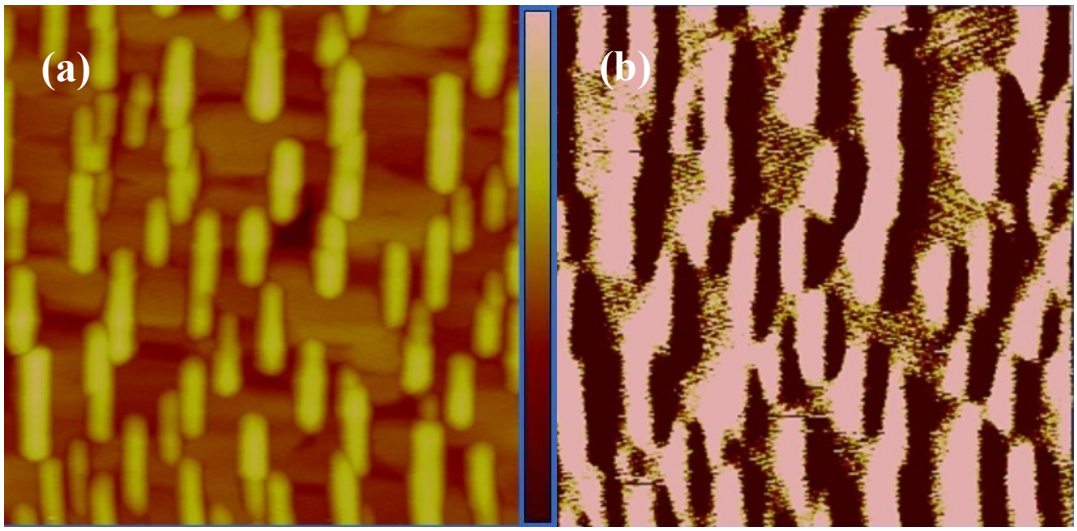

Figure 4.6. AFM (a) and MFM (b) images of BFO-CFO on (110) STO (AFM error bar: 50nm).

Prior research has shown that the CFO phase has a large magnetocrystalline anisotropy of $K_1=2\times10^6$ erg/cm^3; thus, the crystalline anisotropy energy difference between the <001> and <110> directions is $\Delta E=K_0-(K_0+K_1/4)=5\times10^5$ erg/cm^3,[123] which is close to the shape anisotropy energy for a nanostructure with an aspect ratio of R=5:1. However, it has been reported that effective magnetocrystalline anisotropy energy (K_{eff}) is strongly dependent on the size of the magnetic nanostructures: K_{eff} will decrease as the particle size decreases.[124-126] The M-H loops for BFO-CFO on an (001) STO substrate exhibited similar ferromagnetic behavior when referenced to their

in-plane <001> and <$1\bar{1}0$> directions. The crystal lattice mismatch between CFO and STO was 7.7% while the corresponding results for CFO and BFO was 6.06%. A large crystal lattice mismatch will induce excessive misalignment in the longitudinal and perpendicular interfaces. Lower coordinated atoms at the surface will then play a more significant role, resulting in decreased agnetocrystalline anisotropy. Accordingly, an easy axis along the length can be expected for BFO-CFO on (110) STO: i.e., the IP1 direction in Figure 4.7(b), where IP1 denotes the long axis <$1\bar{1}0$> of the CFO nanostripes and IP2 the short axis of <001>. The M-H loops for the BFO-CFO epitaxial layers in both the IP and OP directions are shown in Figure 4.7(a). The thickness of the sample was 200 nm. Therefore, the aspect ratio between IP1 and OP was 3:2. IP1 is the easy axis with a much larger M_r, which also had a larger H_c compared with the OP direction. The value of M_r was then measured as a function of the in-plane rotation angle θ, as shown in Figure 4.7(d). A sine-like wave function for M_r can be seen with a large M_r in the IP1 direction (0.79), and a small M_r along IP2 (0.33). Again, the largest M_r was observed in the OP direction (80° and 100°) due to the limited aspect ratio(R) value. These results demonstrate a strong anisotropy for the BFO-CFO layers. This phenomena suggests an effective method for solving the problem of the superparamagnetic limit, where the existence of a strong easy axis may provide enhanced tolerance for tracking misregistration and side-writing for longitudinal recording.[127]

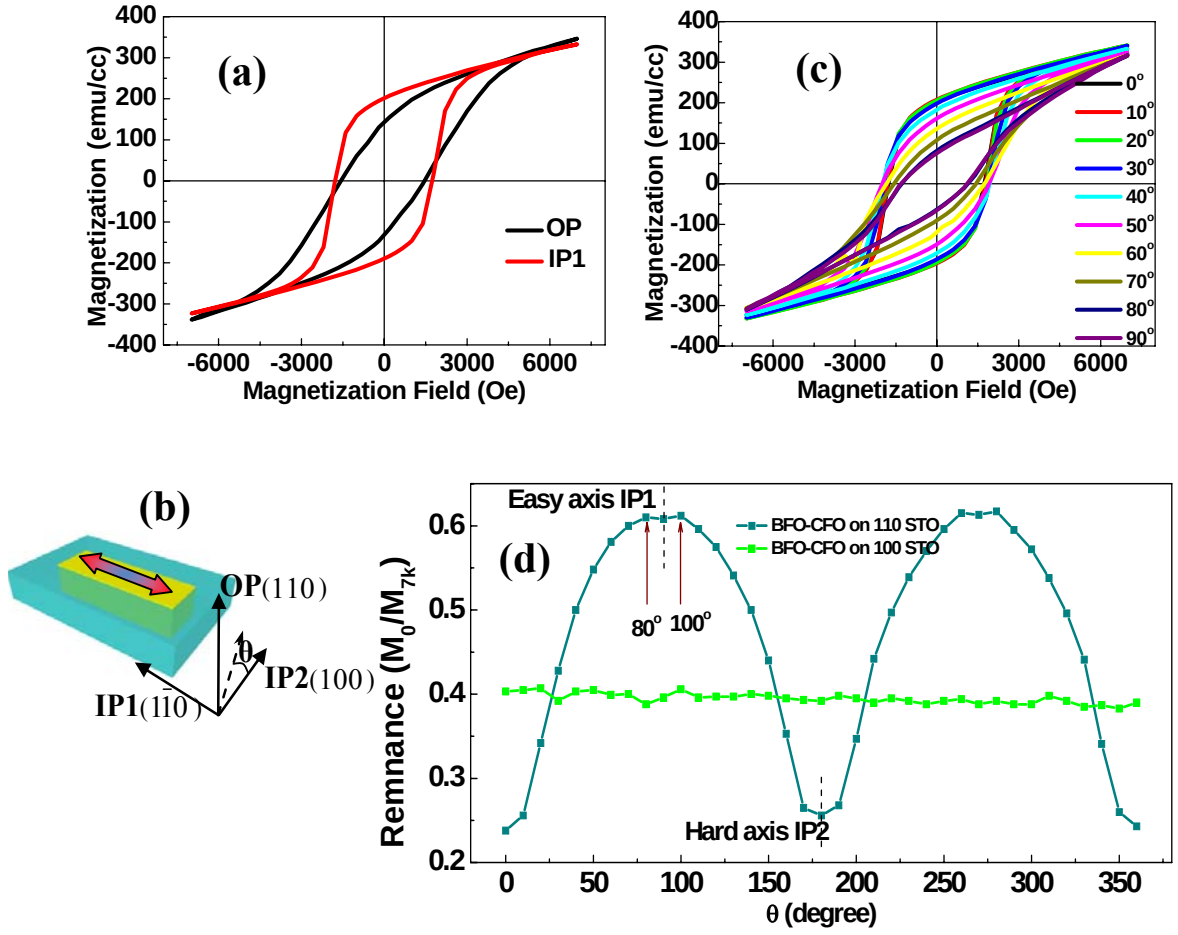

Figure 4.7. (a) M-H loops of (110) BFO-CFO along the IP1 and OP directions. (b) Schematic of magnetic easy axis in the in-plane direction. (c) M-H loops of BFO-CFO on (110) STO with different in-plane rotation angles. (d) Remnant magnetization as a function of in-plane rotation angle θ for BFO-CFO on (100) and (110) STO.

As depicted in Figure 4.8(a), for the BFO-CFO on (110) STO, there were two different interfaces along the IP1 and IP2 directions, respectively. The interface along the IP1 direction was 5 times larger than the corresponding result along the IP2 direction for a CFO nanostripe with an aspect ratio of 5:1. A biaxial strain should

result in similar magnetic strain anisotropy for both the in-plane and out-of-plane directions for each BFO-CFO interface. However, in the out-of-plane direction, the effect of Strain1 and Strain2 can be added together since they both act along the same direction; in comparison, the strain effects act separately along the IP1 and IP2 directions. Thus, the strain along the three different directions can be roughly estimated to be S_{op}:S_{ip1}:S_{ip2}=6:5:1. The CFO crystal structures along the ($\bar{1}10$) and (110) directions were identical; thus, no magnetocrystalline anisotropy between IP1 and OP was observed. We measured the M-H loops for a 200 nm BFO-CFO thin film with different IP1 to OP rotation angles, as shown in Figure 4.8(b) and (c). IP1 is the length direction of the CFO nanostripes, making it the magnetic easy axis, which had a magnetic remnant of 0.55. The OP direction was expected to be the magnetic hard axis as a result of the magnetic shape anisotropy. However, smaller remnance values (~0.35) were found for θ=60° and 120° relative to the value (0.43) at θ=90° along the OP direction. This outcome is associated with the existence of a compressive strain along the OP direction, which induces out-of-plane magnetic anisotropy. The total magnetic anisotropy, therefore, is the competing effect of the IP1 shape anisotropy and the OP strain anisotropy, where shape anisotropy is more significant—therby resulting in a uniaxial in-plane magnetic easy axis along the IP1 direction.

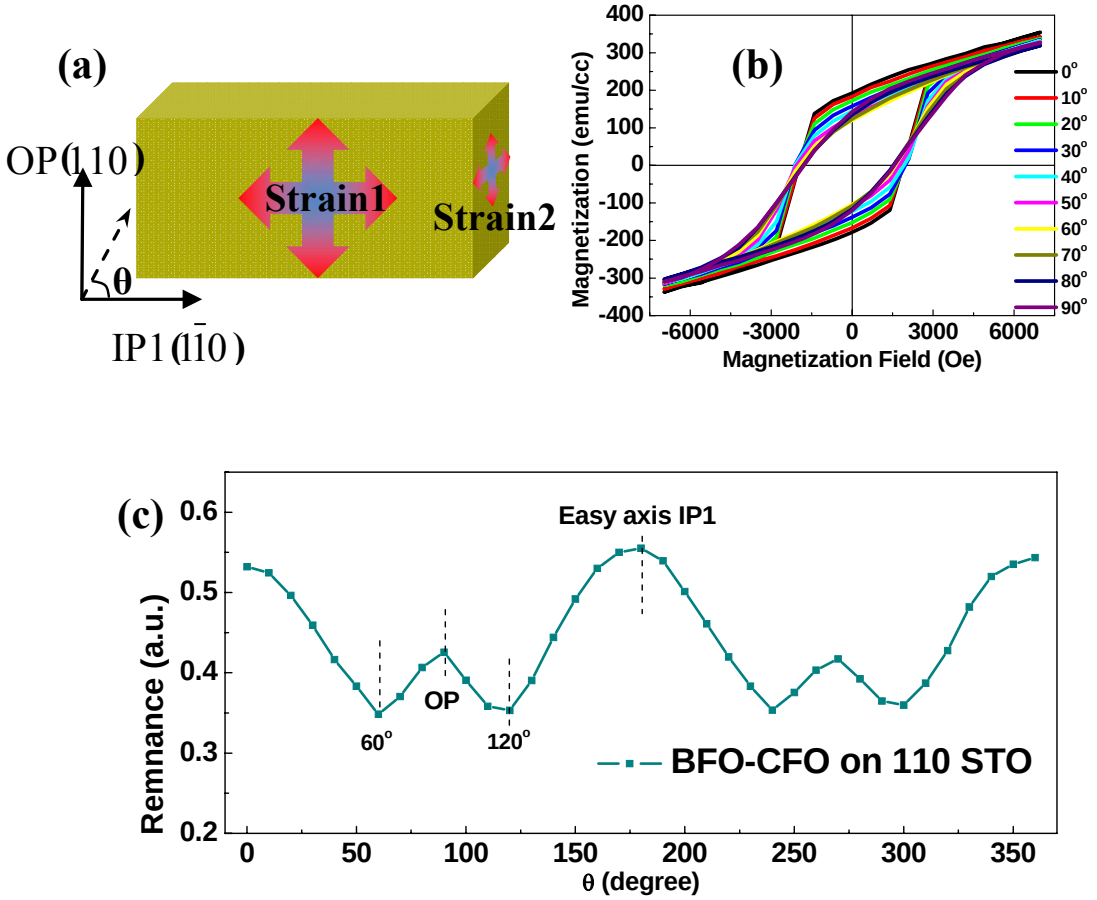

Figure 4.8. (a) Schematic of two different strain effects in the BFO-CFO interfaces along different directions. (b) M-H loops of BFO-CFO with different in-plane rotation angles from the IP1 direction. (c) Magnetic remnance as a function of in-plane rotation angle θ.

Figure 4.9 shows the phase architecture and magnetic response of a BFO-CFO film on (111) STO. Although it has been reported that CFO has a smaller surface energy mismatch with STO compared with the BFO phase, we found that CFO formed as segregated triangular cylinders embedded in a coherent BFO matrix. A BFO-CFO thin film with a thickness of 500 nm was selected due to a comparatively large out-of-plane magnetic anisotropy (compared with thinner films), which favors MFM measurements. The three parts of this figure show AFM and MFM images of

BFO-CFO with different magnetization states. Black triangular areas can be clearly seen in (b), indicating a spin-up state in the CFO pillars under -5 kOe, whereas the white ones in (c) indicate a switching to spin-down under 5 kOe.

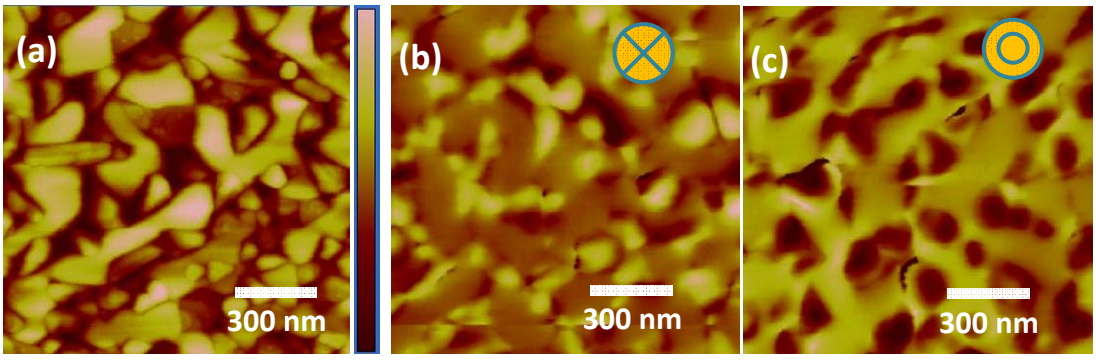

Figure 4.9. (a-c) AFM and MFM images of 500 nm BFO-CFO films on (111) STO with different magnetic configurations (AFM error bar: 125 nm).

Figure 4.10 illustrates the magnetic response of a BFO-CFO film on a (111) STO substrate. The M-H loop of the 500 nm BFO-CFO on (111) STO is shown in (a), where it can be seen that M_r in the in-plane direction is still larger than the out-of-plane result, despite the large aspect ratio (R≈5) of CFO prisms. This intractable in-plane easy axis can be attributed to the shape edge of the triangular CFO pillars. The magnetic pole density is strongest in the tip area of the triangles, resulting in a large demagnetization field, as illustrated in the inset schematic in (a) of this figure. In this case, the demagnetization factor N_{ip} is much smaller compared with that of an elliptical one. This will then pin the easy axis along the in-plane direction. To confirm this phase architecture, we annealed a BFO-CFO film with a thickness of 300 nm at 860 °C for 3 hours to evaporate bismuth and decompose the BFO perovskite phase. Detailed procedures can be found in our previous work about the application of BFO-CFO on (100) STO substrates.[128] We then used acid to etch the remaining iron oxide reduced from the BFO. Distinct CFO prisms can be seen in top-view SEM

image, as shown in Figure 4.10(e). This release effect was also confirmed by XRD results. In (c) of the figure, the BFO-CFO layer released CFO, as evidenced by the apperance of pure CFO diffraction peaks. A compressive strain value of 0.079% in the CFO phase of the BFO-CFO layer was estimated by comparing with pure CFO thin films on (111) STO. After annealing and etching the BFO matrix, the (111) diffraction peak from BFO disappeared; in contrast, the CFO (222) peak remained but shifted from $2\theta=37.28°$ to 37.22°. This shift is due to the release of compressive strain from the BFO matrix. We then compared the M-H loops for the 300 nm BFO-CFO film before and after the releasing procedure, as shown in (d). Despite the large strain along the out-of-plane direction, the BFO-CFO film still exhibited an in-plane magnetic anisotropy with a larger remnant magnetization and a larger H_c along the in-plane direction compared to the out-of-plane direction. For the released CFO nano-arrays, the value of H_c significantly decreased due to the release of the compressive strain, as well as to the fact that the in-plane magnetic anisotropy became much more significant. Detailed magnetic response changes are provided in Table 4.1. Additionally, the M-H loops for the 300nm BFO-CFO thin film on (111) STO with different in-plane rotation angles are shown in Figure 4.11. No significant changes could be found in either H_c or for magnetic remnance values as a function of the in-plane rotation angle θ.

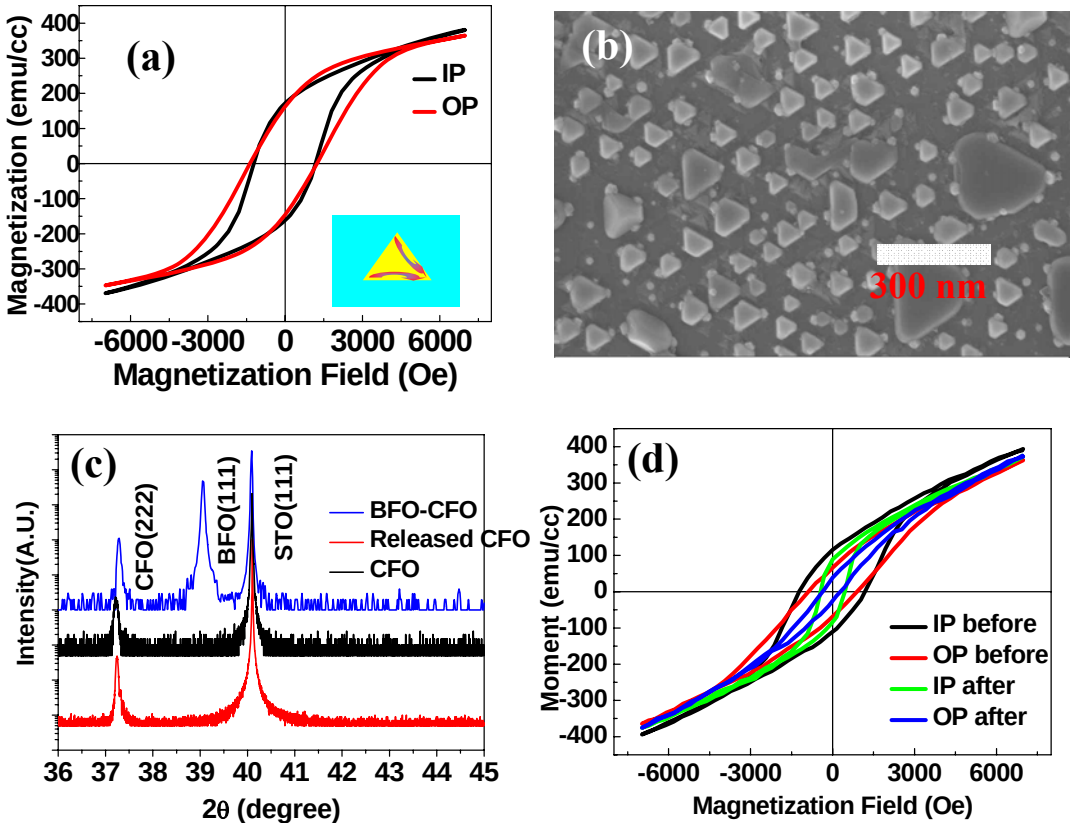

Figure 4.10. (a) M-H loops for 500 nm BFO-CFO on (111) STO and a schematic of demagnetization field (inset); (b) Top-view SEM of released CFO prism arrays; (c) Comparison of XRD results for BFO-CFO, released CFO and pure CFO thin films; (d) M-H loops of BFO-CFO and released CFO.

Table 4.1. Comparison of coercive field (H_c) and remnant magnetization (M_r) for BFO-CFO and released CFO nanoarray structures in both in-plane (IP) and out-of-plane (OP) directions.

Structure	$H_{c\text{-}ip}$(Oe)	$H_{c\text{-}op}$(Oe)	$H_{c\text{-}ip}/H_{c\text{-}op}$	$M_{r\text{-}ip}$(emu/cc)	$M_{r\text{-}op}$(emu/cc)	$M_{r\text{-}ip}/M_{r\text{-}op}$
BFO-CFO	1235	889	1.39	115	66	1.74
released CFO	450	20	1.40	89	38	2.34

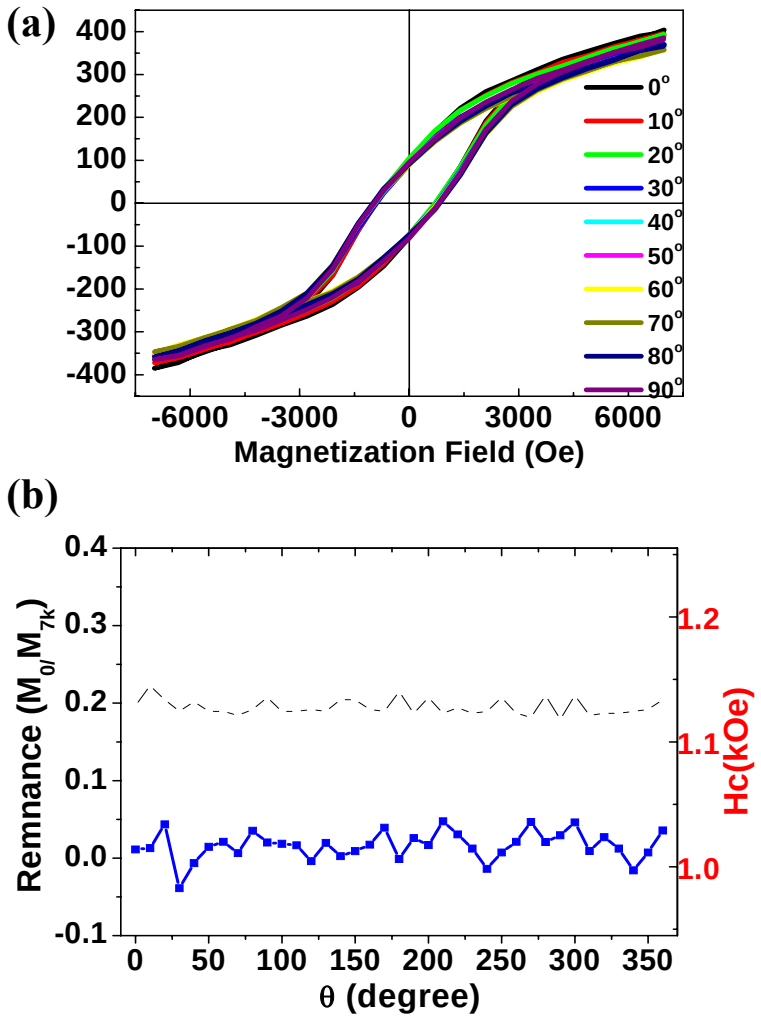

Figure 4.11. M-H loops of BFO-CFO and released CFO. (a) M-H loops for BFO-CFO with different in-plane rotation angle. (b) Magnetization remnance and H_c as a function of in-plane rotation angle θ.

4.3 Summary

Table 4.2 summarizes the phase distribution, morphology and magnetic anisotropy for BFO-CFO thin films grown on (100), (110), and (111) STO substrates. Dramatic differences can be found for BFO-CFO with different shapes. Total magnetic anisotropy is represented as the cooperating effect of shape and strain anisotropy. In (100)-oriented BFO-CFO thin films (thickness>100nm), magnetic shape anisotropy and strain anisotropy are all in the OP direction—as is the easy axis. In (110)-oriented BFO-CFO thin films, magnetic shape anisotropy lies in the IP1($1\bar{1}0$) direction, whereas strain anisotropy is in the OP direction. The competing effect of these two findings results in an easy axis in an IP1 direction and a hard axis that is 30° from the OP direction. In (111)-oriented BFO-CFO thin films, the sharp edge of the CFO prism results in a large IP magnetic anisotropy, while the strain anisotropy is in the OP direction. The easy axis is in the OP direction. No obvious magnetocrysalline anisotropy has been found due to the small size of CFO nanostructures with a large surface-to-volume ratio.

Table 4.2. Phase architecture, morphology and magnetic anisotropy of BFO-CFO self-assembled thin films grown on differently-oriented STO substrates.

substrate	CFO shape	lateral size (nm)	Thickness (nm)	Shape anisotropy	Strain anisotropy	crystalline anisotropy	total anisotropy
100	square	100	300,500,900	OP	OP	N/A	OP(uniaxial)
110	stripe	60(W), 300(L)	200	IP	OP	N/A	IP(uniaxial)
111	triangle	100	300,500	IP	OP	N/A	IP(biaxial)

In summary, we deposited BFO-CFO self-assembled thin films on three differently-oriented STO substrates with different phase architectures. The results confirmed that CFO forms square nanopillars on (001) STO with a lateral size of

around 100 nm, where the aspect ratio could be manipulated by the height of the nanopillars. Complete magnetization switching in each CFO nanopillar was observed in the MFM images. Nanostriped CFO was then deposited on (110) STO substrates with an in-plane aspect ratio of R=5:1. The hard axis was around the OP direction due to competing magnetic shape and strain effects. Furthermore, an easy axis was found along the length direction due to a stronger magnetic shape anisotropy compared with the strain anisotropy result. The CFO had a triangular pillar morphology when deposited on a (111) STO substrate. An intractable in-plane easy axis indicated a strong demagnetization field, which was induced by a large magnetization gradient in each triangular pillar along the in-plane direction. These results illustrate an important relationship between magnetic properties with specific shapes and aspect ratios for BFO-CFO self-assembled heterostructures. Thus, the development of ferromagnetic artificial patterns of nanometer size with controllable magnetic anisotropy may offer important applications for high-density perpendicular storage.

Chapter 5 The ME Effect in BFO-CFO/PMN-PT Heterostructures

Magnetoelectric thin films grown on non-piezoelectric single-crystal substrates can undergo unwanted substrate clamping, which decreases the elastic strain coupling between the ferroelectric and ferromagnetic phases. To reduce the substrate clamping effect, a 1-3 ME structure has been introduced with one ferroic phase in nanopilllar form embedded in the other ferroic phase matrix. In this way, the elastic strain will couple in the perpendicular direction, which is relatively free from substrate clamping. In 2003, Zheng et al.[53] reported BTO-CFO self-assembled structures made up of CFO nanpillars embedded in a BTO matrix on (100) STO substrates. They identified strong anisotropic magnetic properties in the CFO nanopillars, which they attributed to the constraint stress from the BTO matrix. Zavaliche et al.[35] then reported the synthesis of BFO-CFO self-assembled thin films on STO substrates and measured two different electrically-switchable perpendicular magnetic states under ambient conditions. It is well known that magnetic ordering in crystalline solids is related to bond length and the angle of the magnetic atoms.[114] As a number of studies have indicated, magnetic anisotropy is known to be sensitive to the shape, size, and intrinsic and external strain conditions of the ferromagnetic phase.[129-135] Therefore, electro-mechanical-magnetic coupling is believed to be one effective way to control the magenetic response in magnetoelectric composites through interface elastic strain coupling.

Another important property of CFO is that it can be grown epitaxially together with perovskite-structured phases due to fairly close lattice matching. These features permit the formation of well-defined self-assembled structures with CFO nano-pillars embedded in a perovskite matrix. These self-assembled nanostructures allow much

larger interfacial areas between the ferromagnetic and ferroelectric phases, thereby affording much larger magnetoelectric coupling effects since elastic coupling occurs in the out-of-plane direction and thus is not limited by substrate clamping.

In Chapter 3, we reported results from a systematic study of electric field-induced phase transformation in PMN-PT single-crystals, which showed various strain properties: volatile or nonvolation; uniaxial or biaxial. These various strain features result in greater freedeom in designing multifunctional devices. Chapter 4 details our findings with respect to BFO-CFO self-assembled heterostructures with different architectures. Specifically, both the shape and aspect ratio of the CFO component can be controlled by tuning the growing conditions. In this chapter, we describe the epitaxial growth of BFO-CFO self-assembled thin films on PMN-PT single-crystal substrates. It is important to note that PMN-PT crystals have the highest known piezoelectric constants (d_{33}) and electrically-induced strains of ~0.5%.[67, 74, 136] The combination of the strain-sensitive magnetic anisotropy of CFO nano-pillars and the huge d_{33} values for the PMN-PT crystal substrates results in an enormous change in magnetic anisotropy in the heterostructured films.

5.1 Phase separation and crystal structure characterization

We deposited $0.65BiFeO_3$–$0.35CoFe_2O_4$ composite epitaxial thin films using pulsed laser deposition (KrF excimer laser, λ=248 nm) on (001)-oriented PMN-PT single-crystal substrates. The substrates were obtained from the Shanghai Institute of Ceramics at the Chinese Academy of Sciences. The thickness of the films reached 300 nm after one hour deposition at 700 °C. The laser was focused to a spot size of about 2 mm^2, and was incident to the surface of the target using an energy density of 3 J/cm^2. The distance between the substrate and target was 6 cm, and the base vacuum of the

chamber was 10^{-6} Torr. During film deposition, the oxygen pressure was maintained at 75 mTorr.

Figure 5.1(a) shows XRD line scans for the BFO-CFO/PMN-PT heterostructures, both before and after poling of the PMN-PT substrate. The PMN-PT substrate had a tetragonal (T) structure, and hence both (002) and (200) zones were evident. The thickness of the PMN-PT substrates was 0.5 mm, and a voltage of 250V (E=5kV/cm) was used to pole the samples at room temperature. An obvious left-shift of the CFO and BFO peaks can be seen after the poling process, which resulted from an elongation of the *c*-axis of both the CFO and BFO heterostructures due to electric field-induced domain redistribution within the PMN-PT. Figure 5.1(b) shows an SEM top-view image of the BFO-CFO two-phase epitaxial layer. Nano-pillars of CFO with a diameter of about 100 nm can be seen embedded in the BFO matrix. The inset shows a cross-sectional image of the sample prepared via the focused ion beam (FIB) method. In this inset, we can clearly see CFO nano-pillars of length ~100 nm embedded in a BFO matrix, where the aspect ratio of the CFO nano-pillars is about 3:1. This self-assembled nanostructure on PMN-PT is similar to that previously reported by Zheng et al.[118] on $SrTiO_3$ substrates.

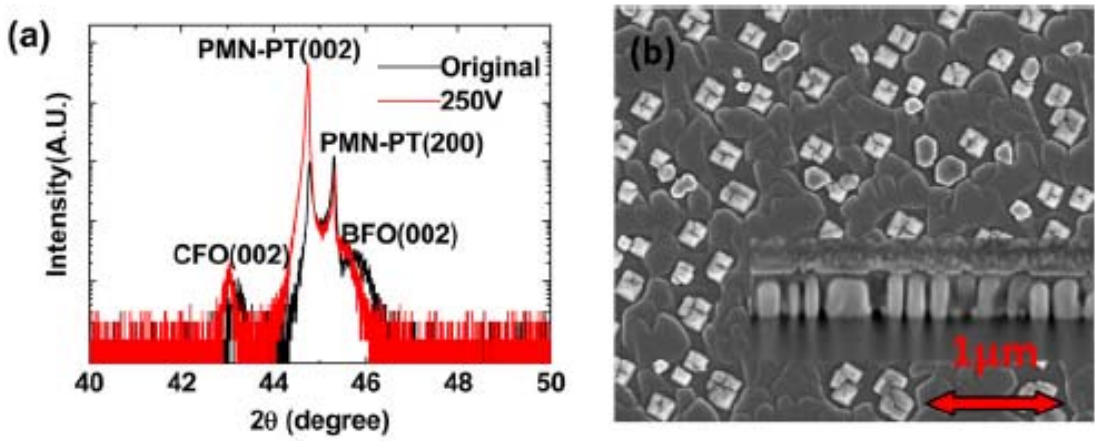

Figure 5.1. (a) XRD line scan of BFO-CFO on PMN-PT before and after polling; and (b) SEM image of the BFO-CFO layer, where the inset shows a cross-sectional view .

The (002) and (200) peaks for PMN-PT in Figure 5.1(a) correspond to the *c*- and *a*- ferroelectric domains, respectively. It should be noted that after poling the intensity of the (002) peak significantly increased; in comparison, the (200) peak decreased. These findings demonstrate that most of the *a*-domains were transformed into *c*-domains, resulting in a nearly single c-domain state oriented in the out-of-plane direction. From the position of the peaks, the crystal lattice parameters of PMN-PT were determined to be (a_t , c_t)=(4.032,4.083). The strain induced by the domain reorientation was thus $\epsilon=(a-c)/a=0.0126$. In addition, it can be seen that the CFO (002) peak shifted from 43.242° to 43.058°, which corresponds to a strain of $\epsilon_{001}=0.426\%$ in the CFO nano-pillars along the c-axis. The magnetoelastic energy density associated with this induced strain in CFO can be estimated as: $E = \frac{-3\lambda \times \sigma}{2} = \frac{3\lambda \times Y \times \epsilon}{2} = 3.1\times10^{6}$ erg/cm^3, where λ is the magnetostriction coefficient (350×10^{-6}) and Y is Young's modulus (141.6GPa). This huge change in the CFO crystal lattice parameters will influence the magnetization of the CFO phase in BFO-CFO self-assembled thin films via the high magnetostriction of CFO. We then annealed the heterostructures to confirm that their original condition could be recovered. Not only did the CFO and BFO peaks shift back to their original positions, but the relative peak intensities of the PMN-PT (002) and (200) zones were also restored to their original values. These results unambiguously demonstrate a correlation between the field-induced lattice parameter changes in the PMN-PT substrate and the corresponding changes in the two phase epitaxial layers of magnetostrictive CFO nano-pillars and BFO matrix.

5.2 Domain rotation-induced strain effect on magnetic properties

The next question influcing the design of this study was the following: How were magnetic properties affect by poling and any field-induced structural changes? Figure 5.2 shows the M-H loops of a BFO-CFO two-phase, epitaxial composite thin film, both before and after poling. The data show both out-of-plane and in-plane directions. Figure 5.2(a) illustrates magnetization as a function of applied magnetic field along the out-of-plane direction under both conditions. First, one can notice that remnant magnetization was reduced by ~ 80% after poling, which demonstrates that only one fifth of the magnetic domains remained aligned in the out-of-plane direction. Such dramatic changes are notably larger than those previously reported for (La,Sr)MnO_3 (LSMO) epitaxial layers grown on $BaTiO_3$ (BTO) single-crystals, where BTO undergoes a rhombohedral (R)→orthorhombic (O) phase transition.[43] Second, the magnetic coercive field was also significantly decreased by poling; specifically, H_c was only about 50% of its value before poling. Correspondingly, Figure 5.2(b) shows the changes in the M-H curve along the in-plane direction due to electric field poling. While the remnant magnetization was increased three-fold by poling, the in-plane coercive field remained nearly the same. Together, these results confirmed that the strain induced by electric field poling influences the magnetization along both in-plane and out-of-plane directions, but in opposite ways.

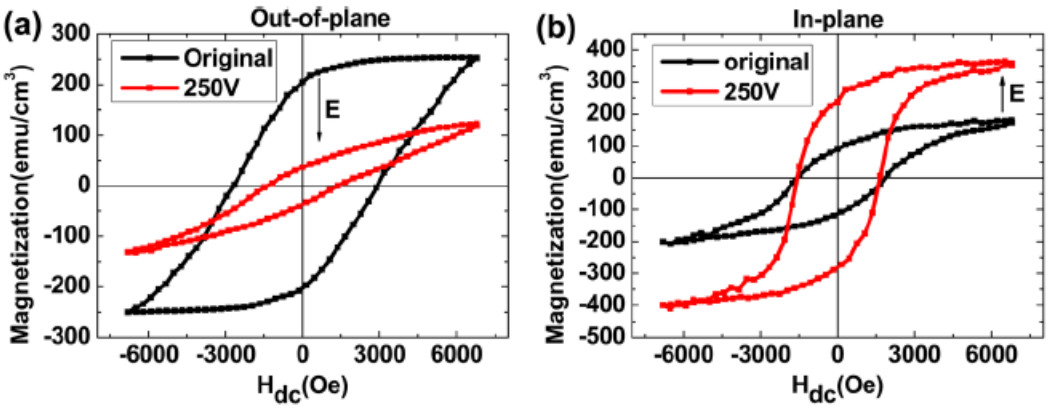

Figure 5.2. Magnetic hysteresis loop comparison before and after polling in the out-of-plane (a) and in-plane (b) directions.

We then calculated the change in the anisotropy energy (E_a) induced by poling. The magnetic energy stored in the CFO phase can be characterized by the hysteresis loss W_h (the area enclosed by the M-H loop). Before poling $E_{a1}= W_h^{out1} - W_h^{in1} = 1.13\times10^6 - 2.87\times10^6 = -1.74$ erg/cm^3, whereas after poling $E_{a2}= W_h^{out2} - W_h^{in2} = 2.12\times10^6 - 0.62\times10^6 = 1.5$ erg/cm^3. Thus, the total anisotropy energy change can be estimated as $E_{a2} - E_{a1} = 1.5 + 1.74 = 3.24$ erg/cm^3, which is much higher than previously reported for BTO-CFO and BFO-CFO on STO substrates.[33, 118] Please note that very high magnetic fields are required for CFO nano-pillars to reach their saturation magnetization along the out-of-plane direction—in fact, much higher than the maximum magnetic field that the vibrating sample magnetometer could apply. Thus, our estimates of changes in magnetic anisotropy energy are limited in this regard, but they still illustrate important changes in the magnetic properties of CFO by poling. Nonetheless, our estimates of anisotropy energy change is quite close in value to the magnetoelastic energy (3.1erg/cm^3) calculated based on the strain of the CFO nano-pillars. This supports our conclusion that the strain in the CFO phase was the cause of the magnetization change. This reduction in E_a can facilitate magnetic

property control of the CFO nano-pillars by external electric field, which could enable unique ME memory or logic functions.

Figure 5.3(a) shows a schematic of our self-assembled BFO-CFO thin film heterostructures on PMN-PT. Illustrated by arrows are the stresses on the CFO nano-pillars along the in-plane and out-of-plane directions. After poling, most of the c-domains were aligned out-of-plane. Thus, we can expect an elongation of the CFO nano-pillars as a result of a tensile strain applied along the out-of-plane direction. Correspondingly, CFO should have a compressive strain along the in-plane direction as a result of the compressive stress from the PMN-PT substrate. However, unlike the out-of-plane direction where the strain was uniaxial, the strain in this case was bi-axial. Also important to note is that CFO has a larger interface area with the BFO piezoelectric matrix in the vertical direction compared with horizontal direction (3:1 aspect ratio); thus, one might anticipate larger strain effects along the out-of-plane direction.

CFO nano-pillars are characterized by a large negative magnetostriction (λ_{001}= -350×10^{-6}). Consequently, after poling, one might expect a large decrease in the magnetization of the CFO nano-pillars as a result of tensile strain. The magnetic domains are more likely to align along the in-plane direction, giving rise to a lower coercive field in the out-of-plane direction. These possibilities were confirmed by M-H measurements, as shown in Figure 5.2. The converse ME coupling coefficient of the BFO-CFO two-phase heterostructure was measured, as shown in Figure 5.3(b). A 50 volt (E=1kV/cm) DC voltage was applied across the PMN-PT substrate, and a change in magnetization (ΔM) of about ≈0.06 mEMU was measured. Using previously reported calculation methods,[43] the converse ME coefficient $\alpha_{ME}=\mu_0(\partial M/\partial E)H$ was calculated, which yielded a value of $\alpha_{ME}\approx1.2\times10^{-7}$ sm^{-1} for our

two-phase layers. This coefficient was much higher than the corresponding value of $\alpha_{ME}=2.3\times10^{-8}$ sm^{-1} previously reported for LSMO films deposited on BTO single-crystal substrates, which was measured near the R→O phase transformation[43] and is comparable with that for bulk laminate ME structures (4×10^{-7} sm^{-1}).[54] More importantly, the enormous ME effect we recorded was achieved by means of a reversible DC electric field, and not via phase transition at a particular temperature. Furthermore, the CFO phase occupies only a modest volume fraction of the BFO-CFO composite thin film. Hence, if the change in magnetization is calculated while also taking into account the actual volume of the CFO phase, a much larger effective value of α_{CME} would be anticipated. For example, if we assume that the thin layer retains the same stoichiometry as the bulk target, we can then estimate an effective value of $\alpha_{ME}\rightarrow2.4\times10^{-7}$ sm^{-1}.

Finally, we used MFM to analyze the magnetic domain response in individual CFO nano-pillars. Figures 5.3(c) and (e) show MFM images of BFO-CFO thin films before and after poling, respectively. Since the probe tip was magnetized in the up direction, the spin-up domains should be dark and the spin-down domains should be light. The size of the dark and light contrast areas was about 100 nm—the same size as shown in the SEM image (see Figure 5.1). In Figure 5.3(c), one can clearly see dark and light contrast areas, which correspond to the magnetic CFO domains. After poling, however, the contrast in these MFM images decreased, and a clear interface between dark and light contrast areas was not evident. Note that the MFM images were obtained in tapping mode without applied DC magnetization (the magnetization of the MFM probe was quite small) or electric fields, and at a specific lift height of 25 nm. One can then conclude that variations in the remnant magnetization of the BFO-CFO thin films in the out-of-plane direction accounts for most of the MFM image contrast.

Thus, these MFM results indicate that the remnant magnetization was decreased notably by poling, which was confirmed by the M-H measurements (see Figure 5.2).

Next, Figures 5.3(d) and (f) display line profiles extracted from the MFM images under different poling/strain conditions, where profile intensity is a measure of magnetization. In these line scans, small "hills and valleys" can be seen at regular intervals, which are indicative of the intensity and direction of the magnetic lines of force on the surface of the sample. From the line scan of the sample before poling, the intensity can be seen to vary from -1.7 to +1.5 degrees; whereas in the poled condition, the intensity varied from –0.3 to +0.3 degrees. Based on these values, the decrease in magnetization by poling can be estimated to be ~20% of the original value before poling, which is in agreement with the calculated ratio from M-H measurements.

Using MFM, we also observed after annealing that the image contrast of the BFO-CFO layer was significantly enhanced, resulting in an image similar to Figure 5.3(c). These results demonstrate that we can reversibly use strain to control the magnetic anisotropy of the CFO nano-pillars in the BFO-CFO layer. Accordingly, it is relevant to note that this enormous electric field-controlled magnetic anisotropy might have relevance for perpendicular recording. One could electrically pole a single CFO nano-pillar area in the BFO-CFO two-phase layers. Then, the magnetic field required to magnetize the CFO domains along the out-of-plane direction would be notably lowered. The area could then be depoled electrically, resulting in a large increase in vertical magnetization.

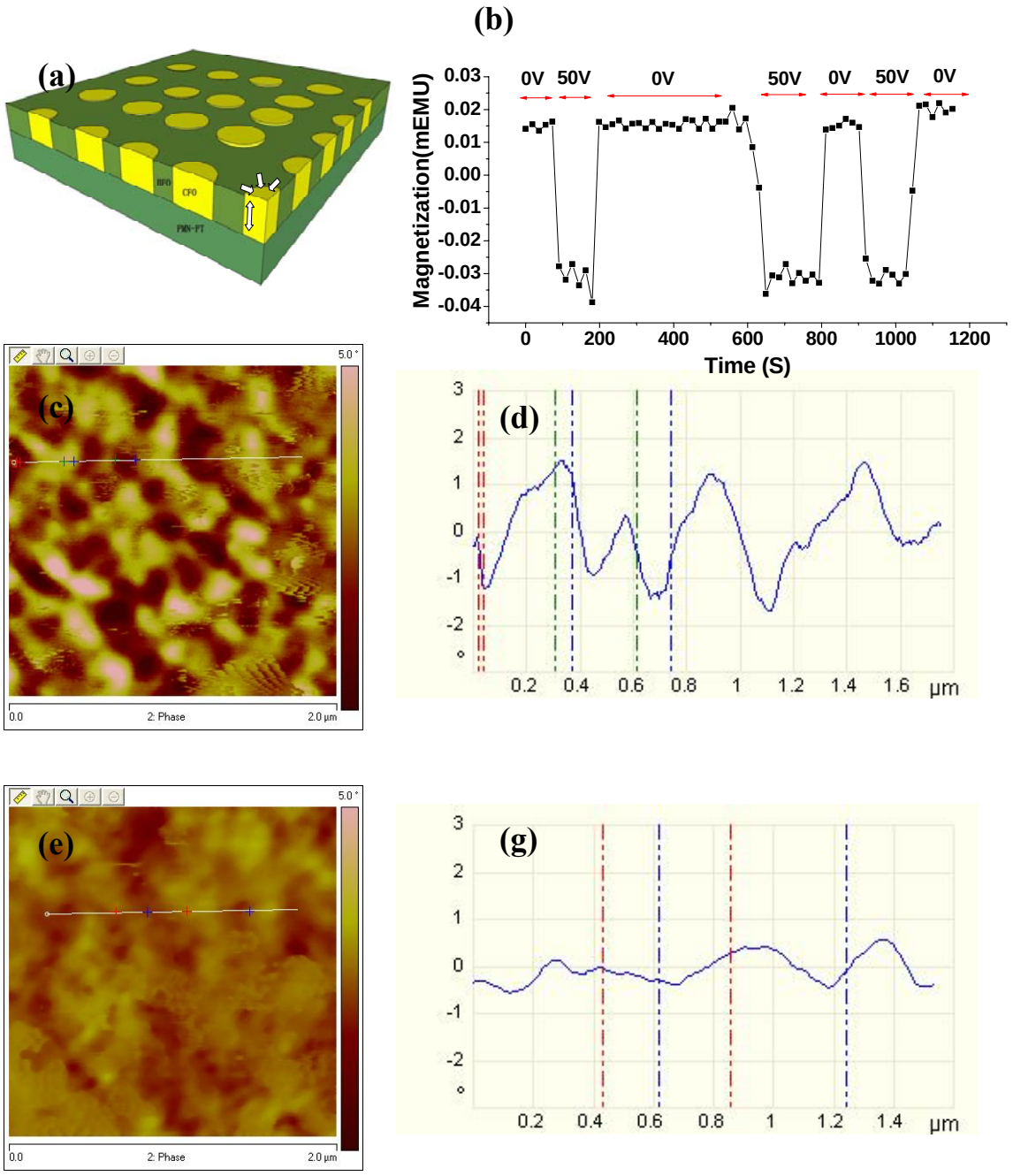

Figure 5.3. (a) Schematic of the strain condition during the poling process; (b) magnetization change induced by a DC electric field as a function of time in the out-of-plane direction; MFM result of the BFO-CFO nanostructure before (c) and after polling (e); and line scans extracted from the MFM images before (d) and after (f) poling.

5.3 Summary

In summary, we successfully deposited vertically-aligned BFO-CFO self-assembled epitaxial composite thin films on PMN-PT substrates. Electric fields applied to the substrates were shown to affect the lattice parameters of the CFO nano-pillars. Correspondingly, a significant decrease was found in both the remnant magnetization and coercive field for the CFO nano-pillars in the out-of-plane direction. Similar changes in magnetization of the CFO nano-pillars were found in the MFM images under the same conditions. Finally, we identified giant values for the converse ME coefficient (10^{-7} sm^{-1}), which were comparable with those of bulk composites. These findings demonstrate an enormous electric field-controlled magnetic anisotropy, which may have important applications in recording devices.

5.4 Future work regarding the BFO-CFO/PMN-PT heterostructures

Different magnetic devices requre different predefined magnetic anisotropies. For example, longitudinal magnetic recording and magnetoresistance random access memory require in-plane bistable magnetiation. Conversely, perpendicular magnetic recording requires stable out-of-plane magnetization. We deposited BFO-CFO self-assembled heterostructures with both in-plane and out-of-plane stable magnetic domains based on the orientaion of the substrate. Important to note is that PMN-PT single crystals possess uniaxial or biaxial strain depending on the direction of the applied electric field. Moreover, the electric field-induced strain can be volatile or nonvolatile based on the stability of the induced phases. Therefore, much remains to be learned about the magnetoelectric effect in BFO-CFO/PMN-PT heterostructures, especially in two areas:

1. The growth of BFO-CFO on R or O phase <001> oriented PMN-PT substrates. The research conducted for this study involved the deposition of BFO-CFO on T phase <001> PMN-PT, where the strain was nonvolatile. This means that the modulation of magnetization was irreversible, which greatly limits the possible application of this design. In contrast, R or O phase PMN-PT single crystals usually show volatile electric field-induced stain. In this case, therefore, the magnetization tuning is reversible, affording more freedom in magnetic device design.

2. The growth of BFO-CFO on <011> oriented PMN-PT substrates. In this scenario, the magnetic moment is confined in-plane, and a uniaxial strain can be generated by an electric field in the bottom of the PMN-PT substrate, which can then be transferred to the BFO-CFO. This design would favor magnetic longitudinal recording and magnetoresistive random access memory.

Chapter 6 The ME Effect in Piezoelectric Thin Film on Metglas

Laminate composites of magnetostrictive and piezoelectric layers have been shown to have much higher ME coefficients in comparison to single-phase materials or particulate composites. The highest ME coefficient to date was reported in Metglas/Pb(Zr,Ti)O_3 laminate structures,[137, 138] which have ME voltage coefficients as high as α_{ME}=20V/cm-Oe. Based on these ME structures, Dong et al.[137] developed highly sensitive, passive magnetic-field sensors that operate at low frequencies with noise floors on the order of 10^{-11} Tesla$/\sqrt{Hz}$ at f=1Hz when using a simple operational amplifier detection method.[139] However, the disadvantages of bulk laminate composites are numerous. First, the size is large, making integration with Si or other substrates problematic. Second, the best magnetostrictive materials are metallic alloys, making the use of ceramic co-firing and packaging unlikely. Third, the dissimilar nature of these layers requires epoxy for bonding component layers, providing a less than ideal interface to facilitate the transmittal of strain between the magnetostrictive and piezoelectric layers. Furthermore, epoxy has problems such as aging, especially when working under resonant conditions. The presence of epoxy can also decrease the ME coefficient due to interfacial relaxation.[140]

Recently, Zhao et al.[140] created PZT/Galfenol heterostructures on Si cantilevers. After etching away the Si substrate, they demonstrated that mechanical clamping effects from the substrate on the PZT/Galfenol heterostructures were greatly mitigated, notably improving α_{ME} relative to that of the unetched Si structures. Brintlinger et al.[141] mechanically released BTO/Galfenol layers from $SrTiO_3$ (STO) substrates by a focused ion beam method, and observed magnetic domain wall movement in the FeGa layer—principally due to the strain transferred from the BTO layer under the

application of an electric field. The ME effect for these heteroepitaxial ME composites is a magneto-elasto-electric effect, just as is the case for laminated ME composites. For these examples, structures must be grown on a substrate suitable to be mechanically released. However, microelectromechanicsl system (MEMS) technologies typically used for this purpose suffer from low fabrication rates and are often incompatible with Si processing technology.

6.1 ME effect in BTO on Metglas

This section describes the direct deposition of BTO films on ferromagnetic metallic glass foils by the pulsed laser deposition (PLD) technique. Commercial 25μm thick, metallic glass (MG) foils were obtained from Vacuumschmelze (Germany). These MG foils had piezomagnetic coefficients of $d_{33,m}$=4 ppm/Oe, which were 3-4 times higher than analogous values for Terfenol-D and Galfenol.[142, 143]

PLD was used to deposit BTO layers on the MG foils. First, Au was sputtered as a buffer layer on the MG in order to achieve highly-ordered BTO layers; sputtering was performed for a duration of 10 minutes. Once the Au formed a continuous layer on the amorphous MG substrates, a secondary grain growth driven by the anisotropic surface free energy[144] resulted in a (111) texture. PLD of the BTO was accomplished using a KrF excimer laser, λ=248 nm. In order to obtain high atomic mobility,[145] as required for crystallization of oriented BTO, a laser energy density of 20 J/cm^2 was utilized. This process allowed for the ejection of high-energy particles from the BTO target, thus enabling the use of a lower deposition temperature and minimizing the oxidation of the MG foil substrates. The size of the laser spot was ~2 mm^2, and the distance between substrate and target was 8 cm. Deposition was carried out in a 90 mTorr oxygen atmosphere with a base vacuum of 10^{-6} Torr. During the first 10 minutes of BTO layer deposition, a laser frequency of 10Hz was used and a

temperature of 300° to prevent melting of the Au layer and subsequent MG oxidation. Next, the substrate temperature was increased to 600° and the deposition cycle was continued for a duration of ~90 minutes.

6.1.1 Crystalization and morphology characterization

XRD results before and after ablation of the BTO target are compared in Figure 6.1(a). Before ablation, the (111) peak of the textured Au layer dominates the spectrum with smaller diffraction features arising from the partially crystallized MG substrate. After ablation, a peak appears that is much more intense than other diffraction features. The d-spacing (d≈0.23nm) of this peak is consistent with the (111) diffraction peak (d=0.231nm) of the BTO structure. These XRD results confirm the growth of highly-oriented BTO films on MG substrates. One may assume a local cube-on-cube epitaxial relationship between the Au buffer layer and the BTO film, such that: (111) BTO||(111)Au|(amorphous)MG. Good in-plane alignment and superior crystal quality of the BTO film was confirmed by measuring the full width at half maximum (FWHM) value, which was 0.14° for the (111) BTO diffraction peak. Other low intensity peaks along different zone axes correspond to other reflections from BTO and are also indicated in Figure 6.1(a).

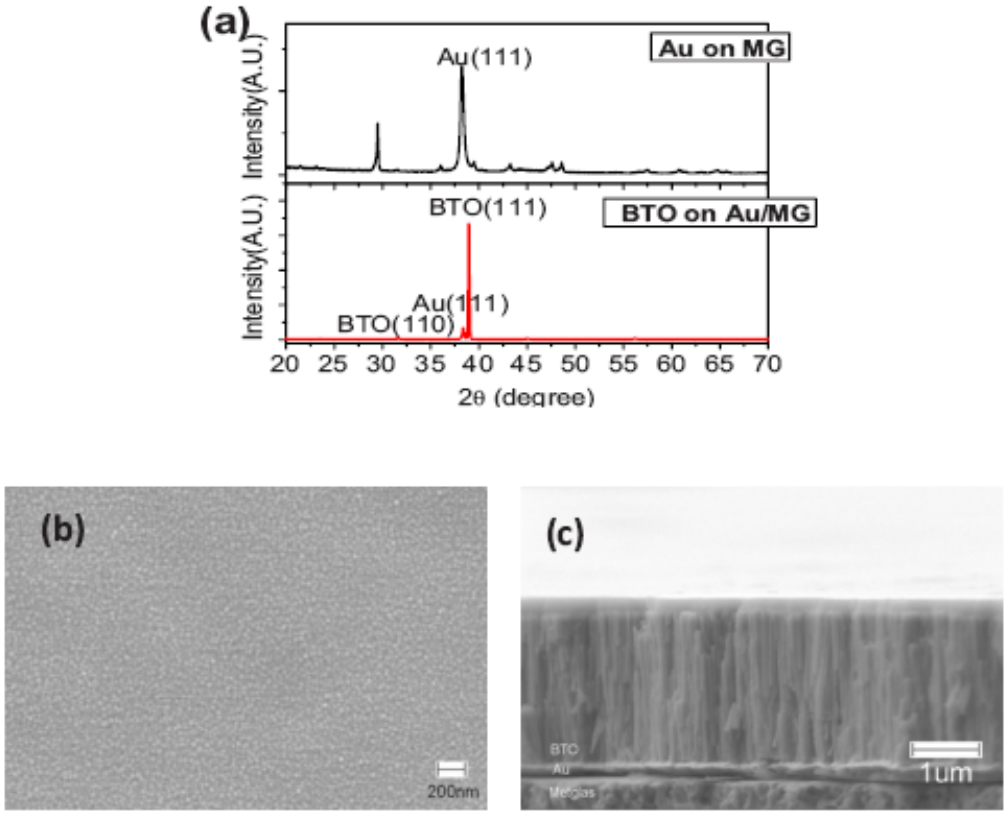

Figure 6.1. (a), (b) Structure and microstructural results for BTO on Au/Metglas (a) XRD line scan; (b) scanning electron microscope image taken from a top view; and (c) cross section.

Figure 6.1(b) displays an SEM image of the top of our BTO/Au/MG heterostructure, which shows the BTO formed as a uniformlayer with a grain size of about 40nm. From the cross-sectional image presented in Figure 6.1(c), one sees that Au formed as a dense and uniform interface between the MG and BTO layers with a thickness of about 60nm. This thickness was sufficient to prevent oxidation of the MG upon subsequent deposition of BTO, while maintaining the (111) orientation of the BTO. The BTO/Au/MG structure was golden in color; however, BTO/MG appeared as black indicating the possible oxidation of MG. The BTO layer thickness reached ~2μm after 2 hours of deposition, with a high-density columnar microstructure of grain size of 40 nm, which is visible in the cross section.

6.1.2 Ferroelectric and ferromagnetic measurement and the product ME effect

The ferroelectric properties of the BTO/Au/MG samples were characterized by a polarization hysteresis measurement using a triangular signal of frequency 100 kHz. Figure 6.2(a) shows a well-defined ferroelectric hysteresis loop with a saturation polarization of $P_s \approx 25\ \mu C/cm^2$, and a remnant polarization of $P_r \approx 7.5\ \mu C/cm^2$. Both of these values are notably larger than the analogous values for BTO deposited on Pt buffered Si.[146, 147] The electric coercive field was 12.5 kV/cm, which was correspondingly much smaller than those for BTO thin films on STO or Si.[148] After obtaining polarization measurements, the BTO films were polarized in the out-of-plane direction and piezoelectric properties were measured. Figure 6.2(b) shows $d_{33,p}$ as a function of electric field. A well-defined butterfly-like loop can be seen with a saturation value for the out-of-plane piezoelectric coefficient value of $d_{33,p} \approx 30$ pm/V as a function of electric field.[149] One of the contributing factors for the enhanced $d_{33,p}$ value is that the BTO layers in the current study are constrained only by a thin (25μm) foil. In contrast, the BTO films on Si substrates are constrained by thick (500μm) Si substrate and thus the constraint effect is much larger.

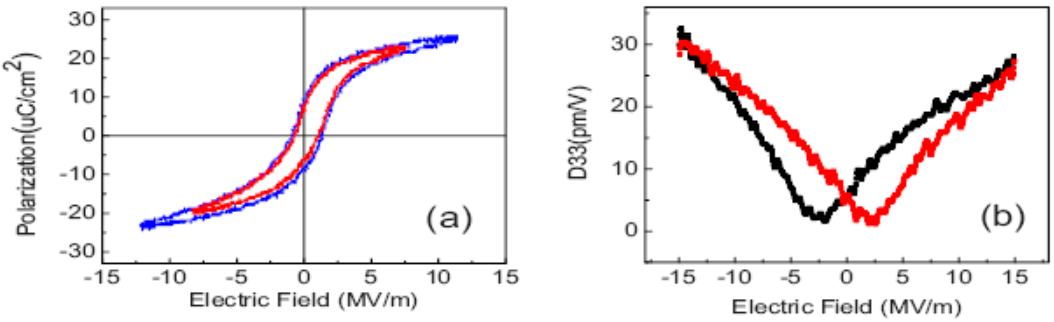

Figure 6.2. Ferroelectric properties of BTO on Au/Metglas: (a) polarization hysteresis loop; (b) piezoelectric hysteresis loop.

The ferromagnetic properties of the MG layer were measured at room

temperature via VSM. Figure 6.3(a) shows a typical M-H loop for the BTO/Au/MG after the high-temperature deposition process. The saturation field was ~400 Oe, and the coercive field was ~60 Oe. Figure 6.3(b) shows the magnetostriction (λ) of MG measured by a strain gauge method. At about 80 Oe dc magnetic field, the magnetostriction reached a value of about 14 ppm. The maximum value of $d_{33,m}$ was ~0.5 ppm/Oe at a dc magnetic field of 200 Oe. This value is comparable with that of Terfenol-D, which has the highest magnetostriction, but is still only 1/8 of that of the as-received MG sample. These results strongly suggest that the MG amorphous foil has undergone partial, if not total, crystallization during the high-temperature film processing.

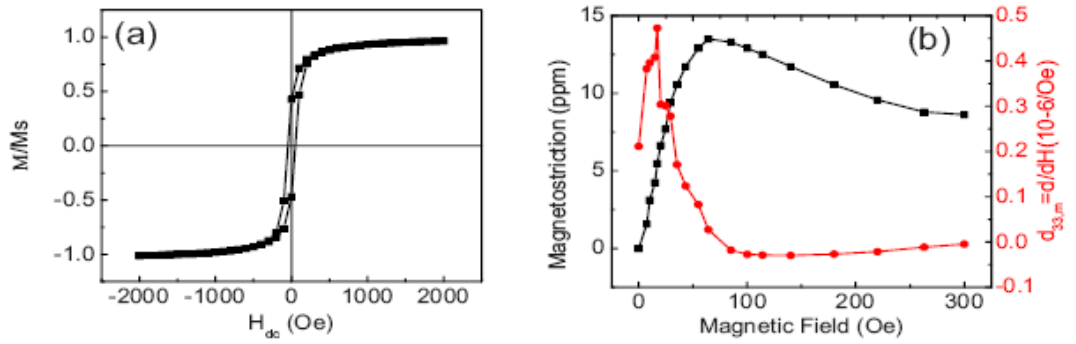

Figure 6.3. (a) Magnetic properties of Metglas with BTO grown on top: (a) normalized magnetization versus applied dc magnetic bias field; and (b) magnetostrictive and piezomagnetic properties as a function of dc magnetic bias.

Finally, the ME voltage coefficient was determined using the structure and measurement method shown in Figure 6.4(a). Details for the measurement method have been reported previously, and are summarized as follows.[150] The Au buffer layer serves as the bottom electrode for the BTO film. A patterned Au top electrode is then sputtered onto the surface of the BTO film. Electrical contacts for the sample are made by gold wire bonding. A large magnet is used as the dc magnetic signal source and a

20 Hz ac magnetic signal is then applied along the long axis of the heterostructure. This method results in an induced strain, via magnetostriction, along the MG foil. The induced strain from the MG is then transmitted to the BTO layer, resulting in a voltage that can be detected by a lock-in amplifier. Figure 6.4(b) shows the magnetoelectric voltage coefficient as a function of dc magnetic field bias. For this study, a maximum value of $\alpha_{ME} \approx 55$ mV/cmOe was found, corresponding to a dc bias field of 20Oe. This value is notably larger than heteroepitaxial and self-assembled ME composites on various substrates.[150] The reason for this higher value compared with that of oxide ferrites is because of the higher value $d_{33,m}$ of the mangetostrictive alloy foil. Another reason for the higher value is that the substrate itself is magnetostrictive, meaning that the structure does not have a large constraint stress, which is unavoidable in ME heteroepitaxial layers or (2-2) structure thin films grown on non-magnetostrictive substrates.

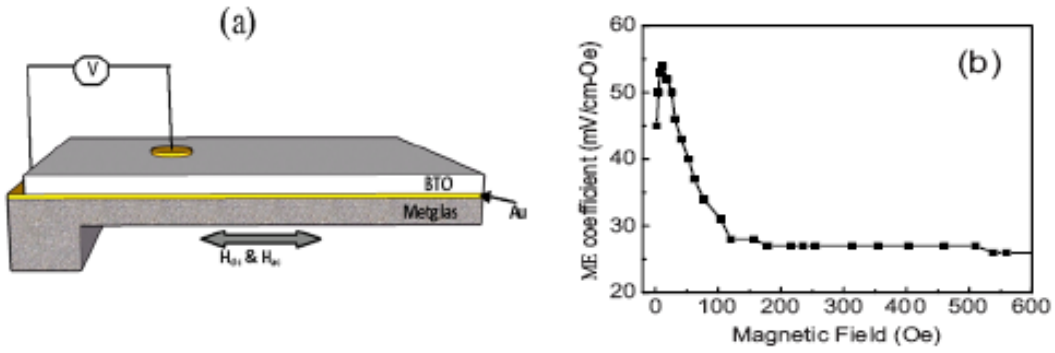

Figure 6.4. (a) Schematic of the BTO/Au/Metglas multilayer structure and measurement setup; and (b) ME voltage coefficient as a function of dc magnetic field.

In summary, we have successfully grown epitaxial (111)-oriented BTO thin films on magnetostrictive MG foils. A buffer of Au was first sputtered on the MG to protect

it from oxidation. Substantial ferroelectric and ferromagnetic properties were obtained from the BTO layers and MG foils. An ME voltage coefficient of α_{ME}≈55 mV/cm·Oe was achieved due to strain coupling between the piezoelectric BTO layer and the magnetostrictive MG foil. Our direct deposition of highly-oriented BTO layers on MG foils with comparable thicknesses eliminates substrate clamping of the ME heterostructure, enhancing the piezoelectric and piezomagnetic coefficients of the respective layers towards values closer to those of their bulk forms, and thus enabling improved magnetoelectricity.

6.2 ME effect in PZT on Metglas

6.2.1 Introduction

The magnetoelectric effect occurs due to the coupling of ferroelectric and ferromagnetic orders through the interface elastic strain in the composite ME heterostructure. Accordingly, dielectric polarization can be induced under application of a magnetic field, and magnetization polarization (M) can be realized under application of an electric field (E). Unfortunately, single-phase ME materials suffer from low Curie temperature and weak polarization at room temperature. Engineered composite ME materials have proven to be more successful in achieving a sizable and useful ME effect. Laminated ME structures in bulk form have been used for high sensitivity magnetic field sensors.[56] However, the ME effect in thin-film heterostructures is extremely weak due to clamping from the substrate. A number of researchers have explored the deposition of ferromagnetic thin films on single-crystal piezoelectric substrates in order to facilitate electric field-controlled magnetic recording.[60, 61, 63] However, the growth of ferroelectric thin films on ferromagnetic substrates has rarely been reported due to the rarity of ferromagnetic single crystals with the appropriate lattice mismatch with perovskite ferroelectric materials.

Ferroelectric thin films on ferromagnetic substrates could show dramatic polarization change under small magnetic field variation due to large magnetostriction-induced strain, and thus can be used as highly sensitive magnetic field sensors.[104] As reported in the literature, the properties of ferroelectric thin films deposited on substrates can be affected by clamping effects of the substrate, lattice mismatch, dislocation generation, as well as thermal expansion and stiffness of the film and the substrate.[151] However, the magnetic response of the ferromagnetic substrate can be tuned by the strain from ferroelectric phase. Therefore, fabrication of sizable ferroelectric/ferromagnetic monolithic heterostructures promises integrated magnetic sensors with controllable ferroelectric and ferromagnetic properties. As detailed in the following section, we investigated the magnetoelectric effect of BTO films grown on MG foils. Specifically, we attempted to deposit $Pb(Zr,Ti)O_3$ (PZT) film on MG foil to take advantage of the large piezoelectric coefficient of PZT, which is usually several times larger than BTO.

6.2.1 Growth of highly-textured PZT films on MG foils

Textured PZT thin films were deposited on amorphous Metglas (MG) foils with a thickness of 25 μm. Pulsed laser deposition was used for thin film preparation. A textured Pt layer with a thickness of 100 nm was sputtered on MG at room temperature, which acted as both a buffer and template layer for the subsequent growth of PZT thin films in an oxygen atmosphere. The deposition temperature for the PZT thin films was kept at 600 °C. An epitaxial $SrRuO_3$ (SRO) thin film (60 nm) was an optimal choice as the bottom electrode for the PZT on $SrTiO_3$ (STO) due to their well-matched crystal lattices.[152] A top electrode was then formed on PZT by sputtering 50 μm Pt, which enabled electrical property measurements.

6.2.2 Growth of highly textured PZT film on MG foil

Figure 6.5(a) provides a top-view and cross-sectional (inset) SEM image of a PZT thin film on an MG foil. One can see pyramidal-shaped PZT grains, which are oriented out of plane, thereby indicating the preferred (111) growth orientation. (100) facets were observed for each pyramid, as marked by a bold circle in this image. The critical step for the growth of the PZT-MG heterostructure was the preparation of a continuous and densely-textured Pt buffer layer of proper thickness. We found that a 100 nm Pt layer could guarantee continuity at high temperature, while preserving the smooth surface of the MG foil substrates. In addition, Pt formed a highly (111) textured layer due to the smaller surface energy along the (111) direction. Clearly, Pt buffer layers served as seed templates for subsequent PZT thin-film growth. One can also see the cross-sectional configuration of the monolithic structure in the bottom-left inset of Figure 6.5(a). A 2.1 μm PZT film covers the 25 μm-thick Pt buffered MG foil. A distinct interface confirms the absence of MG oxidation problem. Figure 6.5(b) shows SEM images of PZT thin films on STO substrates. The PZT grains can be seen to have triangular lateral facets. Smooth PZT thin films of a thickness of 2.1 μm are evident in the cross-sectional SEM image in the inset of Figure 6.5(b). Furthermore, it should be noted that the typical morphology size for the PZT structures on MG was 200 nm; in contrast, the analogous figure the STO substrate was only 80 nm. This discrepancy indicates that the growth mechanism of PZT on MG was less constrained. Figure 6.5(c) shows a XRD line scan for both the PZT-MG and PZT-STO heterostructures. The various peaks are identified in the figure. A Pt buffer layer with a (111) texture is evident by the strong Pt (111) diffraction peak at $2\theta=39.9°$. Also, one can see that the PZT (111) peaks are more intense compared with other zones, demonstrating that the preferred (111) growth direction was continued into the PZT

layer when deposited on MG foils. The intense PZT (111) peak for the PZT-STO heterostructure also confirms the epitaxial growth of PZT on STO substrates. Note that the (111) peak for PZT on MG shifted to the left by about 0.3°, compared with that of PZT on STO. This indicates the release of a compressive strain in the in-plane direction of PZT-MG, which may affect both the ferroelectric and piezoelectric properties.

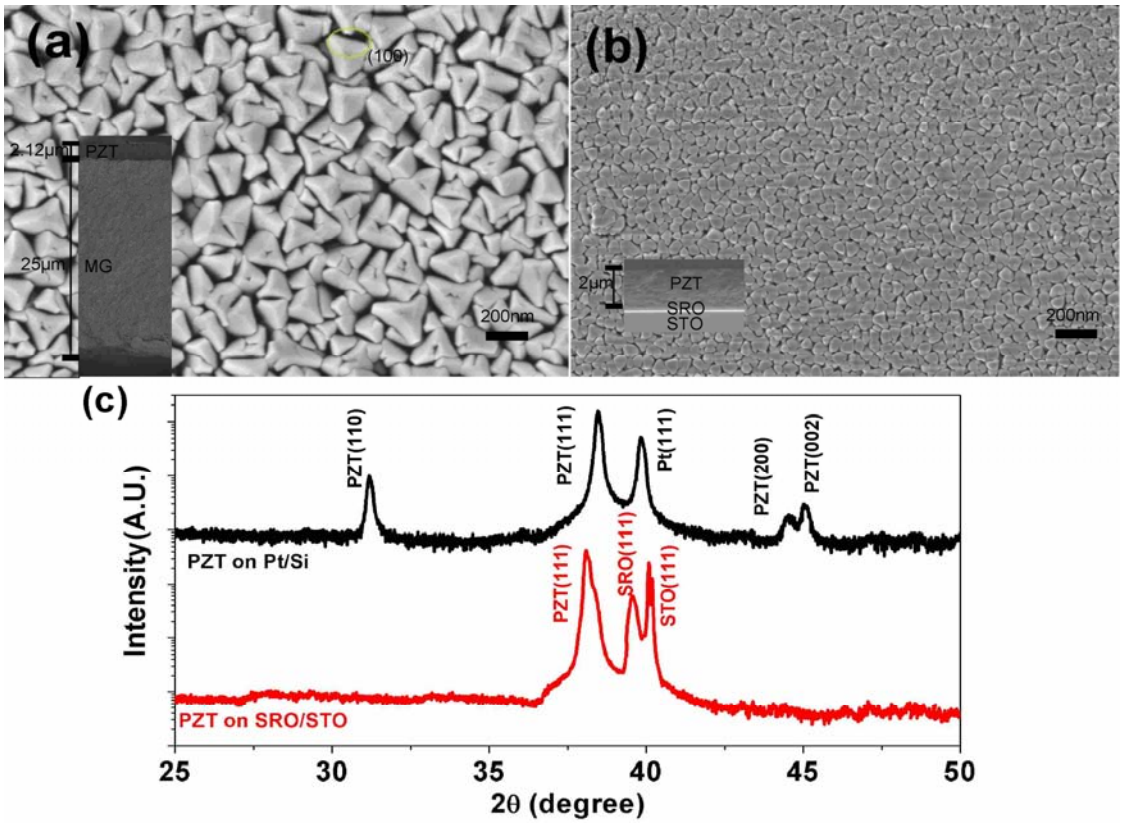

Figure 6.5. (a) SEM top-view and cross-sectional (inset) images of PZT thin films on MG, with pyramid nanocrystals pointing out of plane and one (100) facet marked with green circle; (b) SEM top-view and cross-sectional (inset) images of PZT thin films on STO with triangle shaped nanocrystals; and (c) XRD 2θ scan for the heterostructures.

Figure 6.6 illustrates the evolution of the polarization-electric field (P-E) loops with the number of ac electric field cycles, taken at a test frequency of 10kHz.

Well-defined hysteresis loops are apparent, which exhibit good ferroelectric behavior for PZT layers deposited on both MG and STO. It should be noted that we used the same electrode type and configuration for all sample measurements, and thus can negate any variations due to electrode effects. Figure 6.6(c) summarizes the P-E data, showing P_r as a function of the number of electric field cycles. The P-E loops of PZT on STO in the initial state had a nearly square shape, which degraded with the number of cycles N. The remnant polarization decreased logarithmically with N near 10^6 cycles. The logarithmic decrease of P_r indicates that charged defects may have caused a loss of switchable polarization.[152] By $N=5\times10^7$ cycles, one can see a 50% decrease of $2P_r$ from 109 $\mu C/cm^2$ to 53 $\mu C/cm^2$. For comparison, the PZT thin films on MG initially had a small remnant polarization of $2P_r$=24 $\mu C/cm^2$, which increased to $2P_r$=91 $\mu C/cm^2$ by $N=5\times10^5$. Initially, we could see "pinched" P-E loops for the PZT thin films on MG. These constrained P-E loops were previously identified in both PZT- and BTO-based ferroelectric materials.[66, 153] Although various mechanisms have been proposed for this effect, none can be applied in all cases. However, the pinched P-E shape is believed to be related to domain pinning effects by the defect dipoles. Charged defects can be trapped on domain walls, thus reducing 90° domain reorientation effects. Reorientation of defect dipoles can release interaction between defect dipoles and ferroelectric domains. We observed both (002) and (200) peaks in the XRD line scan as shown in Figure 6.5(c). Thus, it is clear that (002) and (200) oriented ferroelectric domain states coexist in PZT thin films. Ferroelectric domains with polarization in the in-plane direction cannot be switched by vertically-applied electric fields; thus, they do not contribute to the P-E hysteresis loops. During P-E measurements, electric dipoles in polycrystal PZT thin films tend to align along the direction of an applied electric field. This means that (200) ferroelectric domains can

rotate 90°, thereby transforming into (002) domains and increasing the switchable polarization. In the initial stage of aging, such domain rotation effects may dominate the P-E loop evolution, as evidenced by the fact that we observed an increase of P_r. As the PZT thin film crossed a critical number of cycles (~5×10^5), normal fatigue effects would become significant, and thus remnant polarization may begin to decrease, as shown in Figure 6.6(a). One should note that after ~2×10^5 cycles, the PZT thin film on MG exhibited a larger remnant polarization than that of PZT on STO.

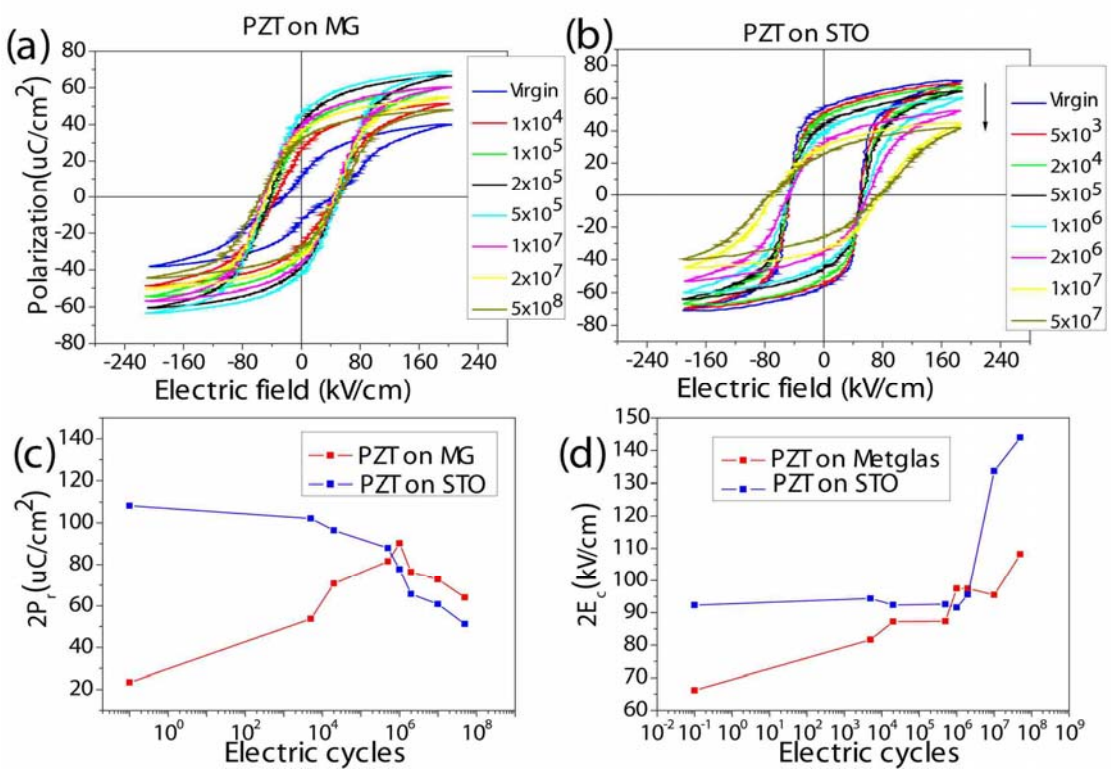

Figure 6.6. Polarization evolution with number of ac electric cycles for PZT layers on MG (a) and STO (b); (c) remnant polarization as a function of N; and (d) coercive field change as a function of N.

Figure 6.6(d) shows the coercive field (E_c) as a function of N. Square-shaped P-E loops were found for PZT on STO (see Figure 6.6b), which became increasingly relaxed with increasing N. This resulted in a significant increase of E_c from 95

kV/cm to 134 kV/cm with increasing N between 1 and 1×10^7 cycles. The PZT thin films on MG exhibited more stable and lower values of E_c, whose increase with N was delayed reaching 109 kV/cm only after $N=5\times10^8$. Based on these changing tendencies for both P_r and E_c, one can reasonably conclude that epitaxial PZT thin films experience a compressive strain from the substrate, thus exhibiting their highest ferroelectric properties during the initial state. Such compression may result in enhanced fatigue. Conversely, PZT thin films on MG may experience less clamping from the substrate (see shift of 111 peaks in Figure 6.5c), which may in turn result in reduced fatigue, smaller E_c, and larger P_r for a given N.

Figure 6.7(a) shows a typical piezoelectric coefficient (d_{33}) measurement for PZT thin films on MG foils and STO substrates. The value of d_{33} for PZT on MG reached 110 pm/V, whereas that of PZT on STO was only 58 pm/V. Piezoelectric thin films usually exhibit significantly-reduced piezoelectric responses, compared to bulk materials due to rigid clamping effects from substrates. This constraint from the substrate may prevent expansion and contraction of the piezoelectric thin films under an applied electric field, reducing both d_{31} and d_{33} values. Figure 6.7(b) shows the piezoelectric phase response with a phase variation of ≈180° for both PZT-MG and PZT-STO heterostructures. Results indicate that complete switching of polarization was achieved under an applied electric field.

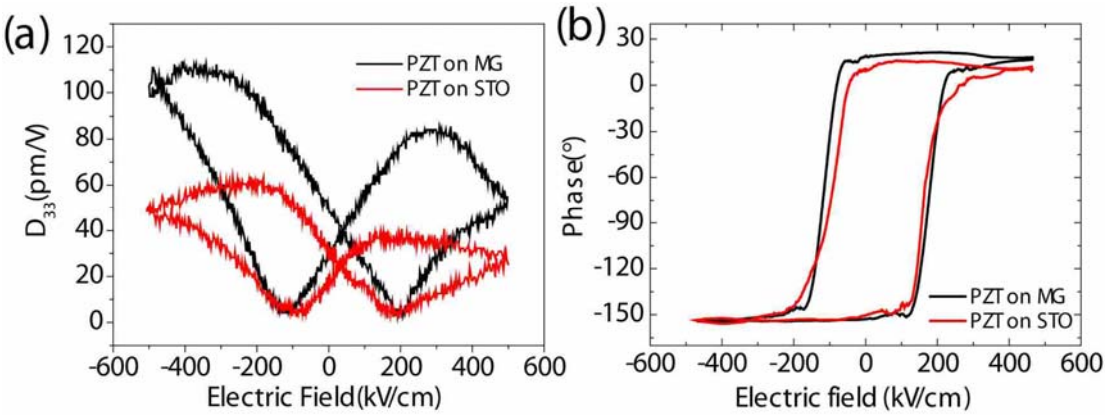

Figure 6.7. (a) Comparison of piezoelectric coefficient of PZT thin films on MG and STO; and (b) piezoelectric response phase change.

Ten years ago, theoretical analysis predicted a 62% reduction in d_{33} for constrained PZT layers compared to unconstrained ones.[154] The PZT-STO epitaxial heterostructures in this study had a thickness ratio of 2:500. Thus, the substrate was able to effectively constrain the movement of the thin films, resulting in a reduced piezoelectric response. By contrast, the PZT-MG monolithic structure had film-substrate thickness ratios of 2:25, which were 20 times larger than the analogous ratio for PZT-STO. This larger thickness ratio may result in reduced clamping effects. Thus, we can have a piezoelectric coefficient d_{33} for PZT-MG that is two times larger than PZT-STO.

Figure 6.8 shows the magnetization hysteresis loops of MG foil after different annealing and strain treatments. The Metglas foils displayed in-plane anisotropic piezomagnetism, high piezomagnetic coefficients and huge magnetic permeabilities ($\mu_r > 40{,}000$). Thus, MG-PZT-based bilayer structures have the highest magnetoelectric coupling coefficient.[56] Annealed MG at certain temperatures under a given dc magnetic bias can display enhanced piezomagnetism. Figure 6.8(a) shows the strain effect from the PZT layer on the magnetic response of the MG layer. The

as-received MG foil showed soft magnetic response with a very small coercive field and enormous magnetic permeability. After high temperature treatment, which is necessary in the PLD deposition process, one can observe an increase in both the coercive (H_c) and saturation (H_s) magnetic fields. Figure 6.8(b) displays an enlagement of the M-H loops for MG with and without a PZT layer on top. Single MG layers had values of H_c≈25 Oe and H_s≈480 Oe, whereas MG-PZT exhibited much larger values of H_c≈35 Oe and H_s≈780 Oe. These larger values are due to elastic strain from the interface between PZT and MG.

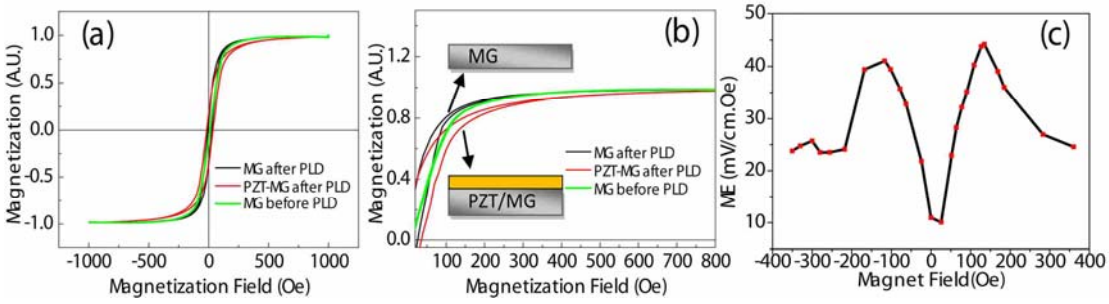

Figure 6.8. (a) M-H loops of MG foils with and without PZT; and (b) enlarged image of (a).

6.2.3 Summary

In summary, for this portion of the study we directly deposited PZT on MG monolithic ME heterostructure with enhanced ferroelectric and piezoelectric properties compared with those of PZT on STO. Results confirmed that PZT on MG had reduced fatigue and much larger d_{33} values (110 pm/V) due to larger film-substrate thickness ratios and reduced clamping effects. Meanwhile, PZT on STO exhibited more severe fatigue and reduced piezoelectric responses (58 pm/V) due to larger compressive strains. Given the fact that d_{33} ≈ 400 pm/V for bulk PZT, our results indicate that higher d_{33} values might be obtained by tuning the thin film-substrate thickness ratio and by appropriate selection of substrates with low

stiffness. Finally, the PZT layer dramatically changed the magnetic response of the bottom MG foils due to elastic strain effects, thereby confirming elastic strain coupling between the ferroelectric and ferromagnetic phases.

6.3 BTO on FeGa

6.3.1 Introduction

The magnetostriction of $Fe_{81}Ga_{19}$ alloys has been shown to be highly dependent on structure and composition.[155] Moreover, research indicates that the magnetostriction of $Fe_{81}Ga_{19}$ alloys is highest in the metastable disordered bcc phase (a=2.91Å).[156] There is a large lattice mismatch between $Fe_{81}Ga_{19}$ and perovskite BTO (a=3.994 Å, c=4.038 Å). However, the difference in atomic spacing along the <110> $Fe_{81}Ga_{19}$ direction and the <100> BTO direction is only about 2%. Thus, if growth of $Fe_{81}Ga_{19}$ is carried out at deposition temperatures greater than 575 ^{o}C using a non-equilibrium deposition process, then it may be possible to achieve (101) oriented BTO thin films on (100) oriented $Fe_{81}Ga_{19}$ substrates. In this case, the growth relationship would be BTO(100)||$Fe_{81}Ga_{19}$(110), and BTO(101)||$Fe_{81}Ga_{19}$(100).

6.3.2 Deposition of BTO on $Fe_{81}Ga_{19}$

We deposited BTO thin films on single-crystal $Fe_{81}Ga_{19}$ substrates by the PLD technique at 650 ^{o}C. During the first 10 minutes of deposition a vacuum condition was used, after which an oxygen pressure of 75 mTorr was applied for 1 hour. After deposition, the mirror-like surface of the alloy substrate was well-preserved, indicating that oxidation of the substrate has been prevented by the initial deposition under high vacuum conditions. XRD and SEM were used to determine crystallization and nanostructure results for the BTO phase. Figure 6.9(a) shows a XRD line scan for the sample before and after BTO deposition. The black curve indicates the (110) peak of

the $Fe_{81}Ga_{19}$ single-crystal substrate; note, however, the lack of other $Fe_{81}Ga_{19}$ peaks in both cases. After BTO deposition, the BTO thin film had an intense (111) peak, but much weaker (110) and (100) peaks. This outcome indicates that the BTO thin films developed a (111) texture, but were not highly oriented. Additionally, a strong $Fe_{81}Ga_{19}$(110) peak can be seen, which indicates that oxidization and phase change could be prevented during the high-temperature deposition process. Figure 6.9(b) shows the SEM top view of the BTO thin films, which displays uniform, nano-sized, triangle and polygonal BTO grains densely-aligned with each other. The presence of an ordered nanostructure indicates well-crystallized BTO nanocrystals with good ferroelectric and piezoelectric properties.

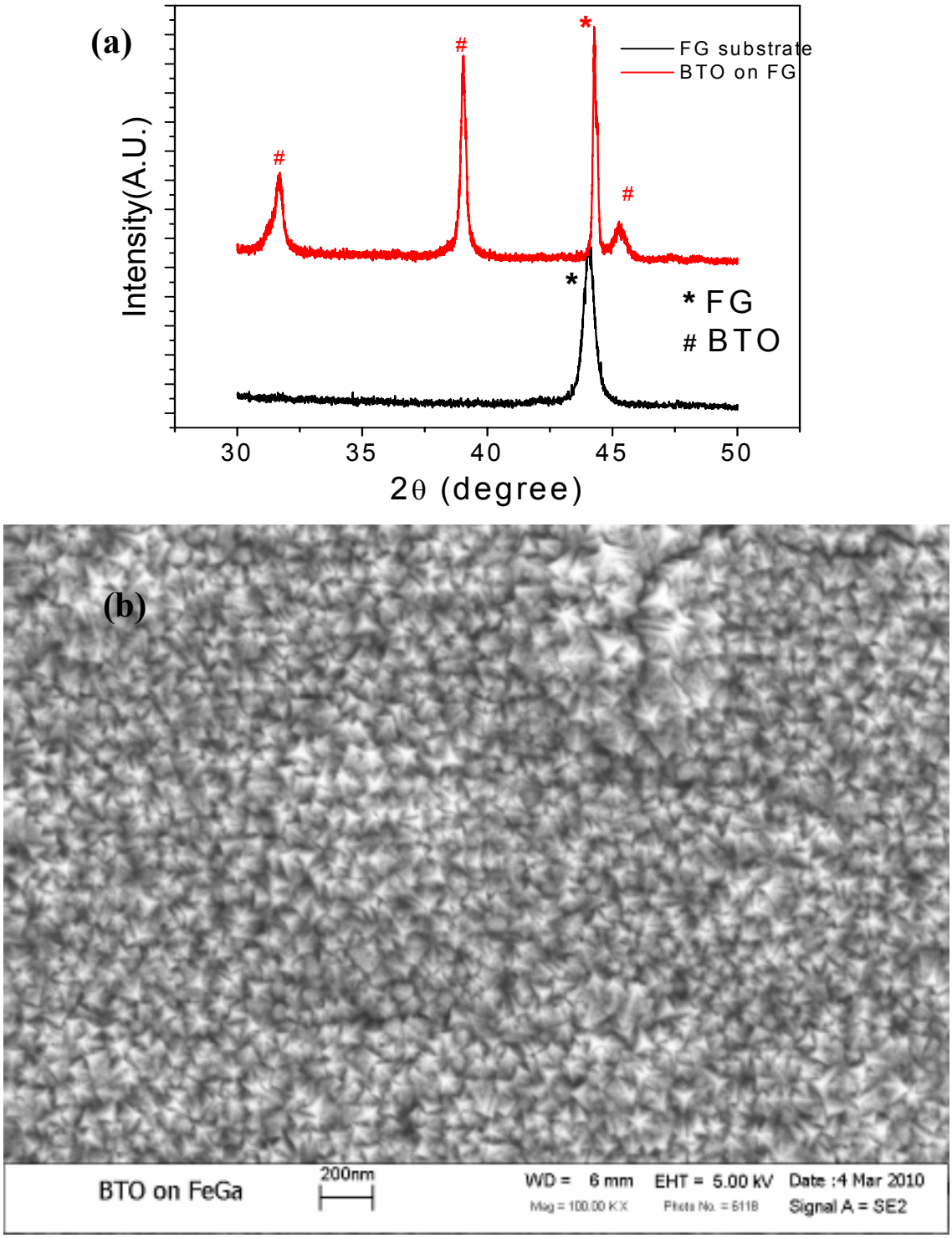

Figure 6.9. (a) XRD of $Fe_{81}Ga_{19}$ substrate and BTO/$Fe_{81}Ga_{19}$, and (b) top-view SEM result.

6.3.3 Ferroelectric and piezoelectric properties of BTO film

Figure 6.10(a) displays ferroelectric property results for the BTO ferroelectric thin films on $Fe_{81}Ga_{19}$. A well-defined ferroelectric hysteresis loop shows a P_s of ~40μC/cm^2 and a P_r of about 18 μC/cm^2. Both P_r and P_s are much larger compared with BTO thin films on Metglas. The coercive field was about 220kV/cm, which was also much larger than coercive field results for BTO thin films on Metglas. This finding indicates that the BTO thin films experienced much larger strain effects on $Fe_{81}Ga_{19}$ single-crystal substrates than that on amorphous Metglas substrates. Piezoelectric property results (see Figure 6.10(b)) show a well-defined butterfly shape with a saturation out-of-plane piezoelectric coefficient value (D_{33}) of ~ 15 pm/V, which is a little larger than BTO on Metglas. In summary, we were able to obtain BTO thin films on a $Fe_{81}Ga_{19}$ substrate with good ferroelectric and piezoelectric properties.

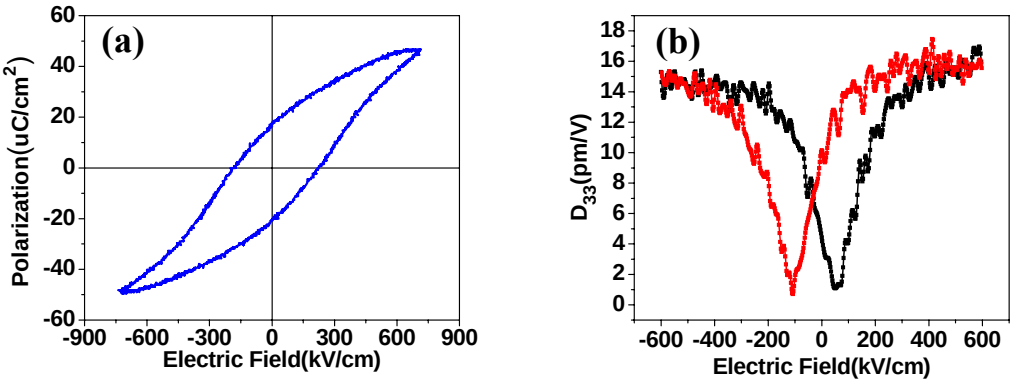

Figure 6.10. Ferroelectric hysteresis loop (a) and piezoelectric D_{33} hysteresis loop (b) of BTO on $Fe_{81}Ga_{19}$.

6.3.4 Ferromagnetic and magnetostrictive properties characterization of $Fe_{81}Ga_{19}$

For this research phase, VSM and strain gauge methods were used to measure the ferromagnetic and magnetostrictive properties of the $Fe_{81}Ga_{19}$ substrate, respectively.

Figure 6.11(a) shows a typical M-H loop of $Fe_{81}Ga_{19}$ in the in-plane direction after a high-temperature deposition process, which indicates the saturation magnetic field to be about 2000 Oe. Also, since $Fe_{81}Ga_{19}$ is a soft magnetic material, the coercive field was very small. Figure 6.11(b) indicates magnetostriction results measured by the strain gauge method. At a dc magnetic field of about 500 Oe, the magnetostriction reached a value of about 70 ppm, which is close to the value measured prior to PLD. Also, the calculated piezomagnetic value of 0.32 ppm/Oe was found to be comparable with Metglas.

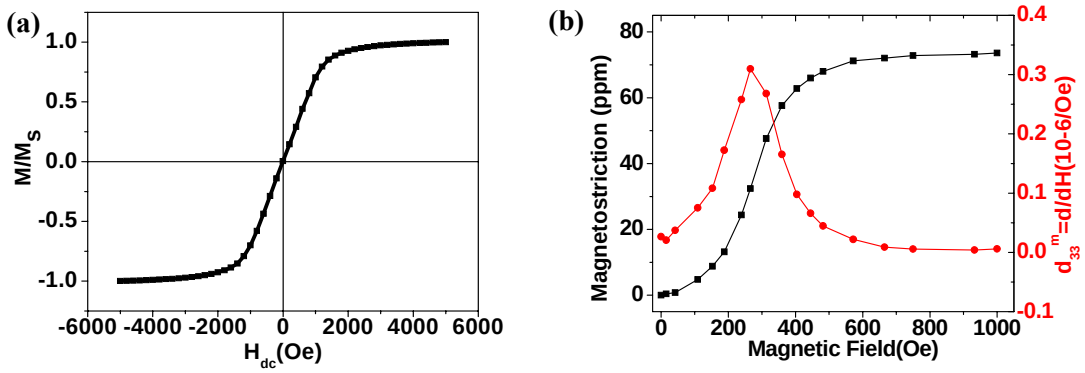

Figure 6.11. (a) Normalized magnetization vs applied magnetic field curve of $Fe_{81}Ga_{19}$ with BTO on top. (b) Magnetostrictive and piezomagnetic properties of BTO/$Fe_{81}Ga_{19}$.

6.3.5 Summary

In summary, we successfully deposited well-crystallized ferroelectric BTO thin films on both Metglas and $Fe_{81}Ga_{19}$ substrates; the measured values of D_{33} were 11 pm/V and 15 pm/V, respectively. Good ferromagnetic and magnetostrictive properties were found after the high-temperature BTO deposition process. The relationship between the Au-buffer layer and the BTO thin film was also studied. Materials comprised of ferroelectric thin films on ferromagnetic substrates may enable the

coupling of two different ferroic order parameters, which might in turn be useful for application in multifunctional devices. The approach could faciliate the growth of various functional oxide thin films on functional amorphous or crystalline alloy materials, and accordingly may allow for different coupling effects.

6.4 Future work

Given the fact that Metglas has enormous magnetic permeability (μ_r>10000), its magnetization saturates at very low DC magnetic biases. Although its magnetostriction is not very high (~40 ppm), the maximum in its piezomagnetic coefficient is 4x larger than that of Terfenol-D. Additionally, it is very thin (25 μm) and flexible, and thus is easier to integrate in small electrical devices, especially in comparison to ferrites. Although magnetostriction will decrease after high-temperature treatment, it is possible to bond a new piece with an existing one. Nonetheless, the total thickness should be still less than 60 μm. By contrast, the normal substrates in use today are typically on the order of 500 μm. Therefore, the magnetoelectric properites of textured piezoelectric films on MG have important implications for the development of magnetic devices that can be integrated into commercial integrated systems. A more detailed investigation of these possible applications is beyond the scope of this study.

Chapter 7 Self-assembled Multifunctional Thin Films

Two-phase hetero-nanostructures represent an important new class of materials that hold great promise for multifunctional device applications due to the ability to couple desirable properties from each component phase.[35, 53] First, hetero-nanostructure systems could offer significant advantages over single-component systems. For example, in $BiFeO_3$ (BFO)-Sm_2O_3 (SmO) vertically-aligned self-assembled thin films, the strain from the SmO component greatly enhances the dielectric property of the BFO one, resulting in much higher resistance.[49] In addition, $BaTiO_3$ (BTO)-SmO two-phase thin films have an enhanced phase stability due to the strain from the SmO nanopillars embedded in the BTO matrix.[157] Second, these two-phase hetero-nanostructures offer the possibility of achieving multifunctionality. For example, coupling the ferroelectric and ferromagnetic properties of $BaTiO_3$-$CoFe_2O_4$ facilitates the exchange between electric and magnetic fluxes. Such magnetoelectric coupling has potential importance for magnetic sensors and electric field-controlled magnetic memory devices.[62, 150] The magnitude of the coupling between the two component phases is proportional to the interfacial area between them, where the elastic strain acts as a coupling mechanism. Vertically-aligned heterostructures have much larger interfacial area compared to traditional multilayer structures, and in addition suffer less substrate clamping. Thus, we expect much larger coupling effects and higher multifunctionality for vertically-aligned nanostructures.

First, this chapter reviews the growth of ferroelectric/semiconductor nano-heterostructures due to their potential application in multifunctional devices.[158,

[159] $NaNbO_3$ exhibits good ferroelectric properties in thin film form, and Nb_2O_5 is a widely used n-type semiconductor. Recent research has shown that $NaNbO_3$- Nb_2O_5 (NNO-NO) composite structures have a phase configuration of NNO nanoplates embedded with NO nanotubes.[160] However, this complex composite structure occurs only in powder form, and thus is difficult to integrate on a substrate. To overcome this limitation, we used PLD for the growth of NNO-NO layers that spontaneously phase separated into vertically-aligned heterostructural layers on the substrate. Such layers provide ease of characterization, and the potential to be integrated with semiconductor technologies. Additionally, various self-assembled structures with different properties have been investigated that may produce novel coupling effects.

7.1 Phase separation and crystal structure configuration in the NNO-NO vertically-aligned heterostructures

For this study phase, we designed an oxide target with a composition ratio of 66at%NNO-34at%NO. The ablation target was made by mixing and grinding $NaCO_3$ and Nb_2O_5 powders in their relevant ratios. The targets were pressed and sintered for 4h at 1000°C. During sintering, the target was contained within a closed crucible to reduce the evaporation of sodium. Since conditions for growth of NNO on $LaAlO_3$ (LAO) are well established,[161] LAO was chosen as the substrate. We deposited NNO-NO composite epitaxial thin films using pulsed laser deposition (KrF excimer laser, λ=248 nm) on (001) oriented LAO single-crystal substrates with $SrRuO_3$ (SRO) thin film with a thickness of 50 nm as the bottom electrode. Three different deposition temperatures of 650°C, 700°C, and 750°C were used. The laser was focused to a spot size of about 2 mm^2, and was incident to the surface of the target using an energy density of 2 $J \cdot cm^2$. The distance between the substrate and target was 6 cm, and the

base vacuum of the chamber was 10^{-6} Torr. During film deposition, the oxygen pressure was maintained at 75mTorr.

Figure 7.1(a) shows a schematic of the phase distribution of an NNO-NO self-assembled structure on LAO. The NNO component formed as nanorods embedded in an NO matrix. NNO has a complex sequence of temperature-induced phase transitions and the thin-film form often shows different phase configurations compared with bulk materials. Here, the NNO component has a pseudo-cubic perovskite structure with a crystal lattice parameter a=3.91 Å, as well as a modest lattice mismatch with the cubic LAO substrate (a=3.82Å). Therefore, the growth of NNO films on a LAO substrate follows a layer-on-layer growth mechanism. The NO phase is orthorhombic with crystal lattice parameters of (a_0,b_0,c_0)= (6.168 Å, 29.312 Å, 3.936 Å), where b_0= 8×3.664.[160] Thus, the NO phase can grow on LAO substrates with the following lattice heterostructural configurations: (001)NO||(100)LAO and (010)NO||(010)LAO in the in-plane direction, and (100)NO||(001)LAO in the out-of-plane direction. Evidence of such a growth condition for NO on LAO was found by XRD line scans, which exhibited a diffraction peak near 2θ=28.2° corresponding to the (200) plane of the NO thin film. Figure 7.1(b) compares the XRD line scans for NNO, NO, and two phase NNO-NO epitaxial thin films on LAO. The middle (red) curve is the line scan for a pure NNO layer on LAO. Two sharp peaks located at 2θ=22.7° and 46.38° were apparent near that of LAO substrate peaks, which correspond to the (001) and (002) peaks of NNO, respectively. The top (blue) curve is the line scan for a pure NO layer. One sharp diffraction peak was observed at 2θ=28.2° corresponding to the (200) peak of NO. The bottom (black) profile is the XRD line scan for the NNO-NO composite thin film. Additionally, diffraction peaks

from both the NNO and NO component phases can be seen. Clearly, NNO and NO form spontaneously separated phases when grown on LAO.

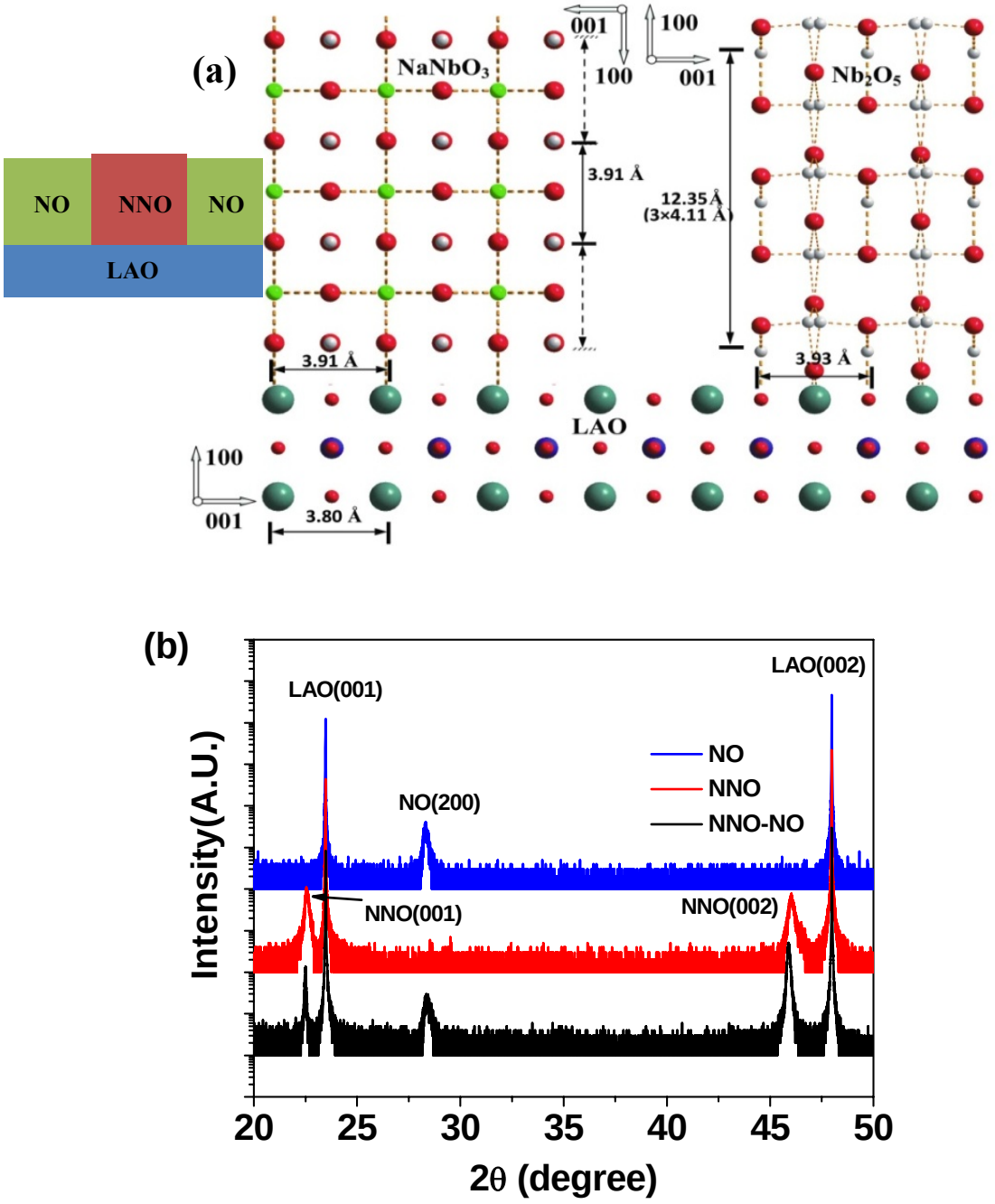

Figure 7.1. (a) Schematic of a NNO-NO self-assembled thin film on a LAO substrate; (b) XRD line scans comparing the NNO-NO composite thin films with pure NNO and NO ones on LAO substrates.

Figure 7.2 shows SEM images of NNO-NO heterostructures grown at different temperatures. Since sodium suffers from evaporation during high-temperature deposition, the resulting thin films grown at different temperatures had different NNO/NO ratios. Again, we utlized three different deposition temperatures (650°C, 700°C, and 750°C). Parts (a), (b) and (c) of this figure show the morphological evolution as the deposition temperature was increased. It is obvious that the thin films deposited at lower temperatures contained a considerably higher number of NNO nanorods, whereas the ones prepared at higher temperature had fewer and more isolated NNO nanorods—presumably due to the volatilization of sodium. Elemental analysis confirmed that the NNO/NO volume ratio changed from 2:1 to 1:2 as the deposition temperature was increased from 650°C to 750°C, as shown Figure 7.2(e), which confirms this sodium volatilization. In addition, we determined the average size of the NNO nanorods by analysis of the SEM images. Figure 7.2(f) shows that the average diameter of the nanorods varied by about 10nm between the various deposition temperatures. As described in a prior study Zheng et al.[34] used diffusion rate versus temperature relationships to analyze the diameter change in self-assembled thin films. However, in our NNO-NO thin films, the diameter of the pillars was not monotonically increasing as a function of temperature. The thin films probably had larger diameters due to abundant Na elements at lower deposition temperatures ($D_{650°C}>D_{700°C}>D_{700°C}$). Figure 7.2(d) provides a cross-sectional SEM image of the NNO-NO thin films deposited at 700 °C, which confirms that the NNO nanorods stand vertically on the substrate with a uniform diameter of about 90 nm.

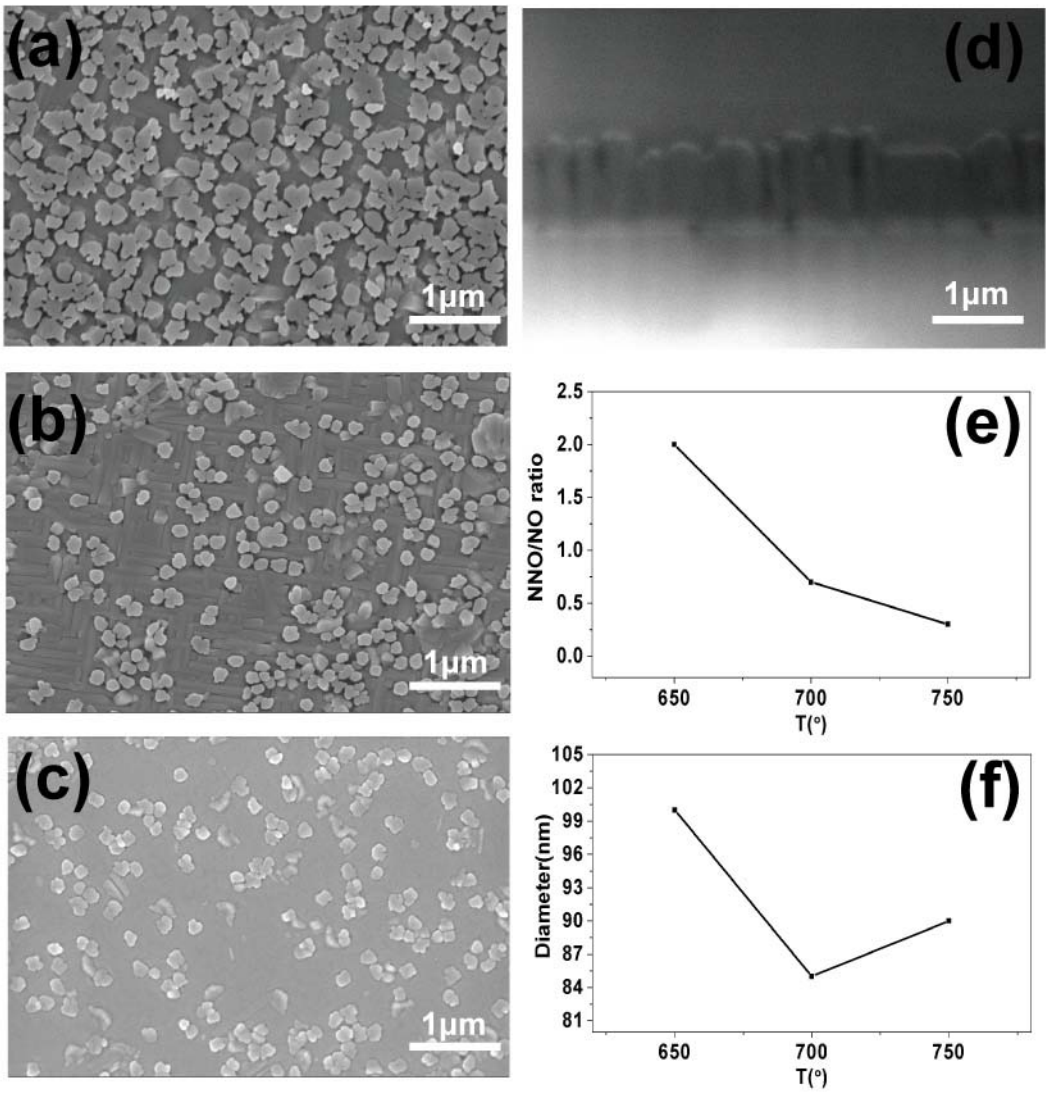

Figure 7.2. (a)-(c) Top-view SEM images of NNO-NO thin films grown at different temperatures; (d) cross-sectional SEM of NNO-NO deposited at 700 °C; (e) NNO/NO volume ratio as a function of deposition temperature; and (f) diameter of the NNO nanorods as a function of deposition temperature.

7.2 Piezoelectricity and conductivity characterization

Figure 7.3 shows PFM images and PFM-D_{33} measurements for a NNO-NO composite thin film deposited at 700 °C. Part (a) of this figure shows the topography of the thin film, where the NNO nanorods stand out from the relatively smoother NO matrix. A line profile of the topography is shown in Part (b). The altitude difference

between the nanorods and the matrix area was close to 50 nm. Part (c) of Figure 7.3 depicts the PFM response of the NNO-NO thin film—specifically, the NNO nanorods experienced much stronger piezoelectric response than the NO matrix, resulting in the clear color contrast in the image. The precise piezoelectric coefficient was obtained by applying an AC voltage of 3000 mV through the conducting PFM tip. The NNO-NO phase distribution was determined by PFM image, which enabled us to move the tip to specific positions to measure the piezoelectric response of both NNO and NO. The NNO phase was piezoelectric; in constrast, the NO phase was semiconducting. Figure 7.3(d) confirms a well-defined D_{33} butterfly shape for the NNO component with a piezoelectric coefficient of D_{33}=12 pm/V. Conversely, no obvious piezoelectric response could be detected in the NO matrix area.

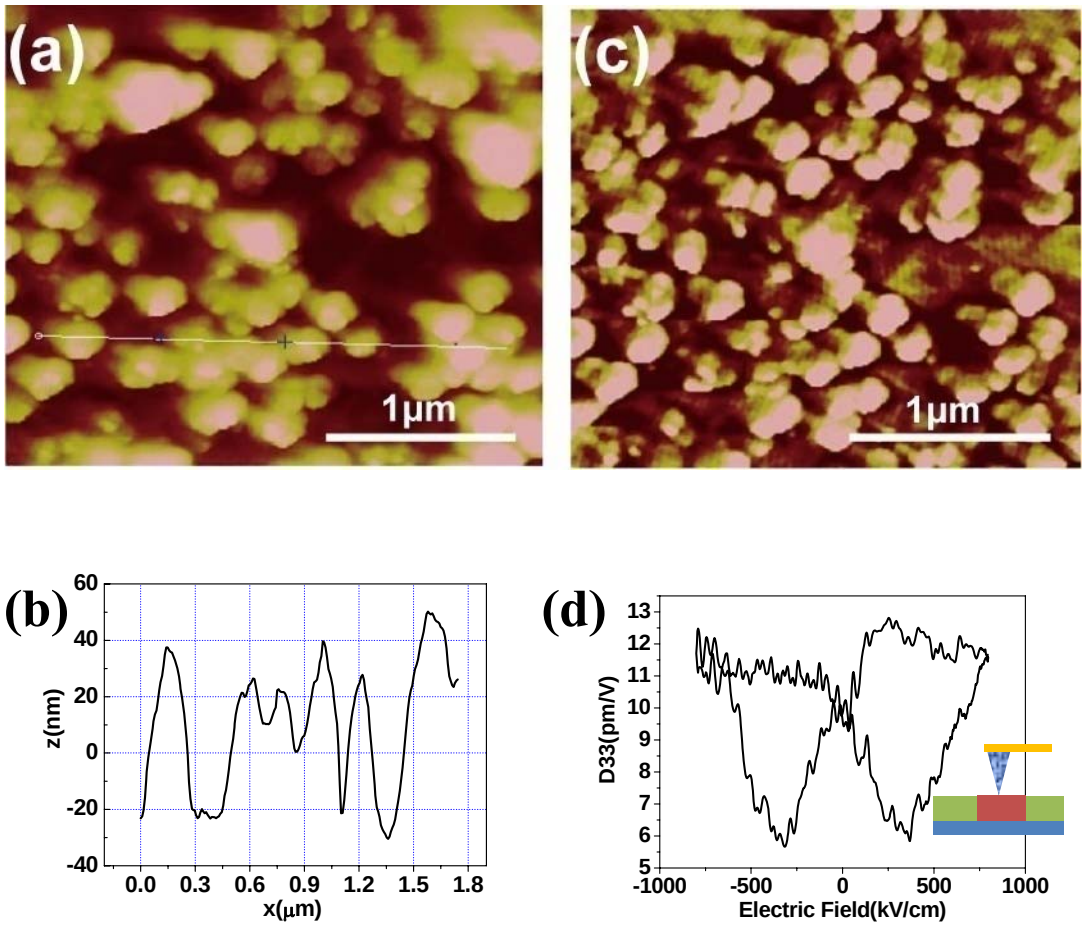

Figure 7.3. (a) Topographic AFM image of NNO-NO a self-assemble thin film (scale-bar:30nm); (b) line profile of the height in selected area in (a); (c) PFM image of NNO-NO thin films taken from the same area, showing distinct piezoelectric responses in the NNO and NO areas; and (d) D_{33} measurements of the NNO component regions.

Figure 7.4 illustrates the rectifying behavior of the NNO-NO thin films with SRO as the bottom electrode. Part (a) of this figure shows the modified Sawyer Tower circuit used to measure the rectified conducting properties of the NNO-NO/SRO heterostructure. An Au square pattern with a side of 50 μm was prepared by sputtering,

which served as the top electrode. Reference capacitor C_r= 10 nf was used to collect the charge through the sample. A triangular wave V_s was introduced from the signal generator. Part (b) shows the voltage on C_r as a function of the triangular signal with a frequency of 1 Hz, which confirms the diode rectifying effect—namely that the NNO-NO/SRO heterostructure allowed electric charges to flow in one direction, but not in the opposite direction. Therefore, we could only detect triangular response V_c on the reference capacitor when V_s was positive. Part (c) of Figure 7.4 shows the current-voltage (I-V) characterization of the Au/NNO-NO/SRO under a DC bias voltage. A turn-on voltage of 4 V and a forward current of 110 μA were observed at 6 V. Au has a work function of 5.1 eV, while that of n type semiconductor NO is 3.4 eV.[162] Thus, electrons have to overcome the Schottky barrier in order to move from NO to Au. In contrast to the disordered interface between Au and NO, SRO is a good heteroepitaxial metallic oxide for its eligible lattice mismatch with NNO-NO thin film. Although SRO has a larger work function (5.2eV) than NO,[163, 164] the diffusion between SRO and NNO-NO prevents formation of a Schottky connection. SRO is a n-type connector based on Hall measurement,[165] so the NO/SRO could form a n-n+ heterojunction, which has a built-in electric field moving from NO to SRO. In this way the NO/SRO heterojunction only allows electrons to move from SRO to NO when the external electric field is larger than the n-n^+ barrier. The turn-on voltage is the summation of the Au/NO Schottky barrier and the NO/SRO n-n^+ barrier.

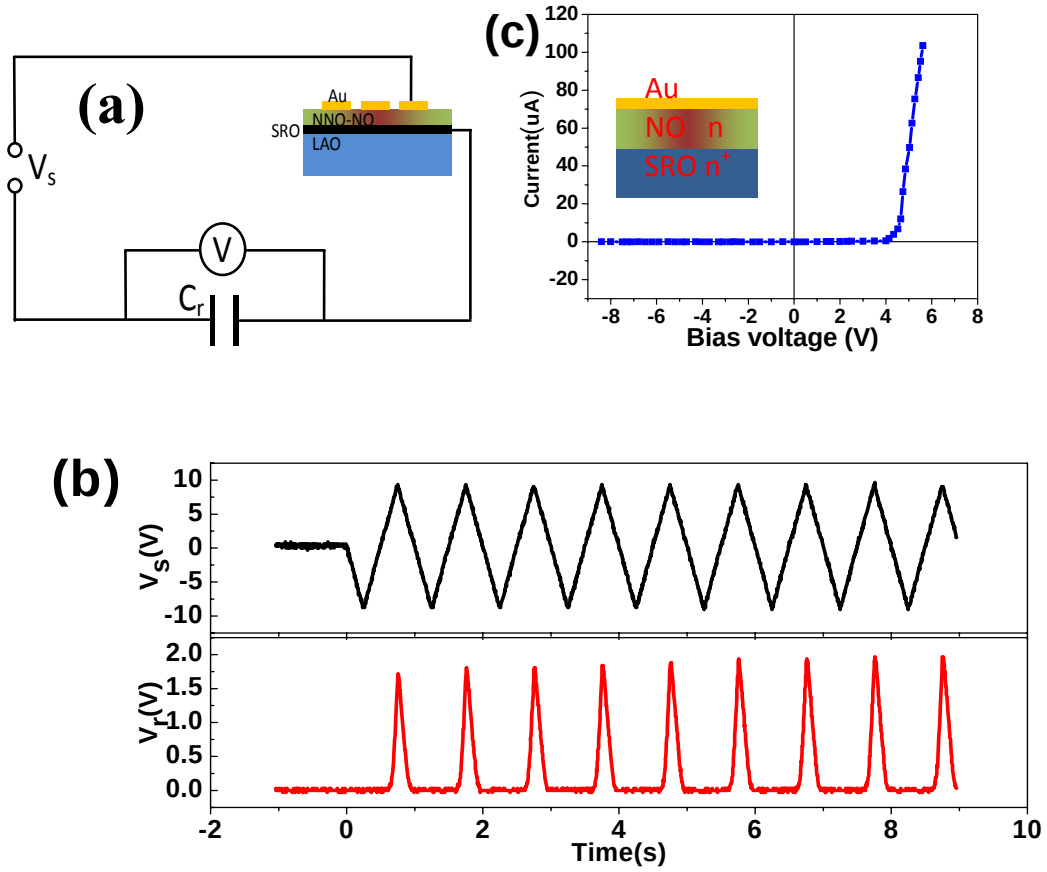

Figure 7.4. (a) Modified Sawer-Tower measurement circuit; (b) Triangular wave signal and the corresponding response on the reference capacitor; and (c) current-voltage measurement of Au/NNO-NO/ SRO heterostructures.

In summary, we deposited NNO-NO (piezoelectric-semiconductor) self-assembled heterostructures on LAO single-crystal substrates with a controllable NNO nanorod dispersion density. The NNO nanorods displayed good piezoelectric properties of D_{33}=12 pm/V, which were measured via PFM characterization. I-V measurement showed a good rectifying behavior due to the formation of a Au/NO Schottky barrier and a NO/SRO n-n^+ heterojunction barrier. Our results confirmed that NNO-NO self-assembled epitaxial layers have dual properties in both their

piezoelectric and semiconductor component phases, and thus show potential for application in multifunctional devices.

7.3 Exploration of novel multifunctional self-assembled structures

The successful growth of self-assembled structures is a complex thermodynamic problem. Many factors should be considered when designing self-assembled structures, which include the crystal structure of the thin film and substrate phases, lattice mismatch between the separating phases and the substrate, and the surface energy of the substrate compared with the thin film phases. Although we have attempted to generate many different self-assembled materials, it is very difficult to make functional materials capable of merging together with separated phases. In most cases, many different phases could form apart the source phases.

This study involved the use of various composite targets with different phase configurations. Even though some of them showed separated nanostructures in the SEM images, no clear phase separation in correspondance with the separate source phases could be identified from XRD results. For selection of appropriate materials and self-organization of these materials, four steps are essential in order to obtain desirable structures and properties.

1. Deposit thin film with common deposition properties and confirm via XRD and SEM that the source materials are truly phase separated.
2. Select the self-assembled materials that show clear phase separation and use terminated smooth substrates to deposit thin films at different conditions with differeing thicknesses to improve the thin film quality and periodicity of the nanostructures.
3. Measure the intrinsic properties of each source phase.

4. Measure all possible interaction properties to determine coupling effect between the source phases.

Chapter 8 Summary and Future Work

This dissertation reports the results of a systematic study of the magnetoelectric coupling that occurred between ferromagnetic and ferroelectric components through interface elastic strain transformation.

First, detailed characterizations were performed on piezoelectric PMN-PT single crystals of differing concentrations. Drastic crystal lattice parameter changes can be triggered by ferroelectric phase transformation, which can be controlled by the application of an electric field. As a result, significant strain levels can be produced in piezoelectric single-crystal substrates and then transferred to the epitaxial ferromagnetic thin films on top. Dramatic changes in magnetic anisotropy were systematically studied where magnetic easy axis can be rotated by an electric field.

Second, we investigated the formation of self-assembled BFO-CFO composite thin films, wherein different architectures can be obtained via selection of substrate orientation. What makes this system interesting is the fact that BFO is multiferroic, possessing both ferroelectric and antiferromagnetic properties; in contrast, CFO is ferromagnetic with enormous magnetostriction properties. The magnetic response within a CFO component can be controlled by both magnetic shape and strain anisotropy. By engineering the architecture of these components, we were able to prepare CFO nanostructures with different feature shapes and varying aspect ratios. In this way, both the quantitative value and orientation of the magnetic easy axis can be accurately controlled. Next, we deposited BFO-CFO self-assembled films on piezoelectric substrates to investigate the magnetoelectric coupling effect. Both quantitative magnetization and magnetic force microscopy measurements showed an

effective control of the magnetic response in CFO by applying an electric field to the piezoelectric substrates.

Finally, we explored novel self-assembled NNO-NO heterostructures with coexisting ferroelectric and semiconductive components. Resulting morphology and crystalline characterizations illustrated the obvious separation of the NNO and NO phases. An interesting current-rectifying behavior was also observed with undefined working principles.

Further work is suggested in three areas:

1. A more detailed study of ferroelastic domain evolution under the application of an electric field for various ferroelectric single crystals, such as PMN-PT, PZN-PT, BTO, etc., is recommended. By controlling ferroelastic strain modulation, we can control the magnetic strain anisotropy in the ferromagnetic film on top. Moreover, ferromagnetic materials with different magnetic properties should be investigated for fabrication of devices requiring specific magnetic responses. For example, microwave devices usually require low loss and effective tuning of ferromagnetic resonance. In contrast, magnetic recording devices prefer magnetic hysteresis loop with large remanent magnetization and a proper magnetic coercive field.

2. A subsequent study involving the deposition of BFO-CFO self-assembled film on differently-oriented PMN-PT single-crystals should be conducted. BFO-CFO systems with a variety of architectures have been prepared on differently-oriented STO substrates, showing configurable magnetic easy axis—and therefore potential for incorporation in a variety of industrial applications. We have only shown magnetoelectric coupling in BFO-CFO on <001> oriented tetragonal PMN-PT single crystals. A follow-up study should investigate BFO-CFO on differently-oriented PMN-PT single crystals with a variety of ferroelectric phase

configurations. Moreover, both the self-assembled film component and the piezoelectric substrate component can be changed with similar materials, e.g. BTO-CFO on BTO, PTO-CFO on PMN-PT, etc.

3. Finally, an exploration of novel self-assembled composite thin films is recommended. The current approach for the formation of self-assembled heterostructures is somewhat generic. Therefore, future studies should attempt to create similar nanostructures from other spinel-perovskite systems, such as $PbTiO_3$-$CoFe_2O_4$, $BaTiO_3$-$NiFe_2O_4$, $BaTiO_3$-$NiCo_2O_4$, etc. Moreover, self-assembled structures can be formed from crystal structures other than from the spinel-perovskite system—e.g., $NaNbO_3$-Nb_2O_5, $CoFe_2O_4$-ZnO.

In closing, the current work suggests a variety of research scenarios—both in the nanostructure formation of complex oxides and in the characterization of nanostructures with tunable properties. Based on the specific characteristics of each component, we can study the electrical, magnetic, and optical properties of the self-assembled films, and more importantly, the possible coupling effects that may hold promise for multifunctional applications.

Appendix A. Fragile O-phase stability around morphotropic phase boundary: How to choose PMN-PT substrates with volatile and nonvolatile electric field induced strain

In my experiments concerning the ME effect in MCFO thin films on <011>-oriented PMN-PT substrates, very different magnetization squareness changes were found for MCFO films on PMN-PT substrates whose compositions are quite close to each other.[1] It is well known that electric field along <011> direction can induce a rhombohedral→orthorhombic (R→O) phase transformation.[2] The stability of the field-induced O-phase determines the retainability of the field-induced strains.

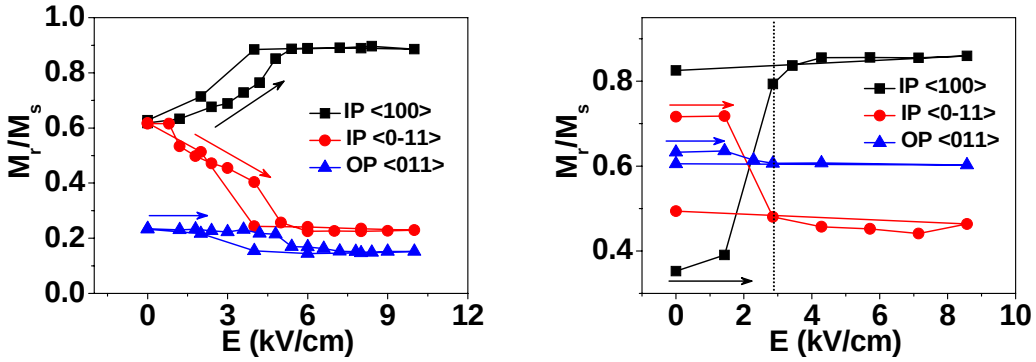

Figure A.1 Electric field dependent magnetization squareness of MCFO thin films on PMN-29.5PT (a) and PMN-30PT (b).

Figure A.1 shows the field-dependent magnetization squareness of MCFO thin films on PMN-29.5PT and PMN-30PT. An electric-field induced R→O phase transformation has been widely reported for <011> PMN-PT.[1-5] Accordlingly, tensile srains are found along both out-of-plane (OP) <011> and in-plane (IP) <0-11> directions, whereas compressive strains are observed along IP <100>. Therefore, with increasing applied external field, the magnetization squareness (M_r/M_s) increases

along the IP <100> direction and decreases along both the IP <0-11> and OP <011> ones. However, the field-induced strain is volatile for PMN-29.5PT, whereas that for PMN-30PT is nonvolatile.

To determine a method by which to better identify the field-induced O-phase stability, I selected eight pieces of <011> PMN-PT substrates and explored the relationship between their compositions and various properties. The growth source materials are designed to be PMN-30PT. However, due to the temperature gradient and thermodynamic fluctuation problems, there is usually composition fluctuation in PMN-PT single crystals. We compared the Curie temperture (T_c) of the first four PMN-PT substrates with the last four ones, the difference was around 2.7°C. This indicates a 0.5at% variation of the PTO concentration across the wafer from which the crystals were sliced.[6] Therefore, I denote the first four PMN-PT substrates to be PMN-29.5PT and the last four PMN-PT substrates to be PMN-30PT.

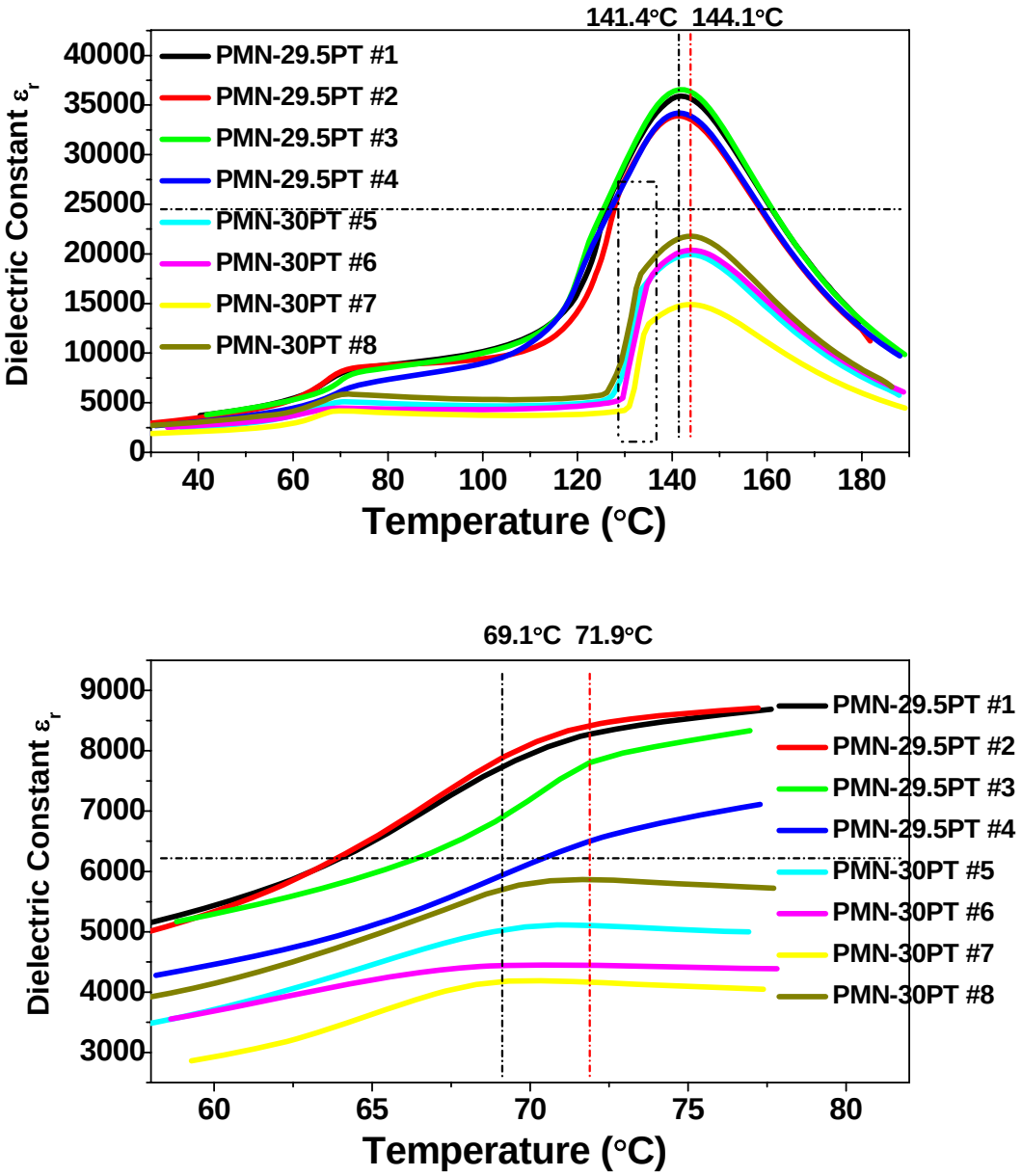

Figure A.2 (a) Dielectric constant as a function of temperature (ε_r-T) in zero field cooling process. (b) ε_r-T around the rhombohedral to tetragonal phase transformation temperature (T_{rt}).

Figure A.2 (a) shows the ε_r-T curves of the eight selected PMN-PT substrates. The first four PMN-29.5PT substrates had a Curie temperature (T_c) of around 141.4°C,

whereas the last four PMN-30PT substrates had a Curie temperature of 144.1°C. One can see the value of the rhombohedral to tetragonal phase transformation temperature (T_{rt}) for PMN-29.5PT was ~71.9°C, whereas that for PMN-30PT was ~69.1°C. This is in accordance with the well-known phase diagram of (1-*x*)PMN-*x*PT, where T_c increases as the value of *x* increases and where T_{rt} decreases as *x* increases.[7] One should note that the four PMN-30PT samples show a drop in ε_r at about 132°C, indicating a growth of microscopic ferroelectric domains.[8] On the contrary, the ε_r-T curves for the PMN-29.5PT single crystals was more smooth. Therefore, it is reasonable to conclude that the formation of longer range ordering in PMN-30PT crystals favors the formation of a field-induced metastable O-phase, whereas the O-phase in PMN-29.5PT is unstable after removal of *E*.

I also compared their piezoelectric (D33) and relative dielectric (εr) constants after the eight selected substrates were poled, as summarized in Table I.

Table A.1 Piezoelectric coefficients (D_{33}) and relative dielectric constant (ε_r) of <011> PMN-PT with metastable and unstable O-phase after poling.

PMN-PT No.	D_{33} pC/N	ε_r	Group No.
#1	1185	3200	Group-I
#2	1320	3342	
#3	1299	3096	
#4	1401	3233	
#5	322	875	Group-II
#6	328	958	
#7	342	976	
#8	364	987	

It is clear in this table that the first four listed PMN-29.5PT substrates (Group-I) had higher values of D_{33} (>1100pC/N) and larger ε_r (>3000) after electric field poling. The composition of PMN-30PT is near the edge of the morphotropic phase boundary (MPB) where the phase configuration is very sensitive to the external electric field. A poling electric field (10kV/cm) along <011> can then induce a metastable O-phase which is maintained after removal of the field. Therefore, we can obtain a monodomain O-phase condition in PMN-30PT,[3,5,9,10] which has smaller values of D_{33} (<400pC/N) and ε_r (<1000).

However, PMN-29.5PT is far from the MPB region. Therefore, the field-induced O-phase relaxs back after removal of the external field. Thus, the poled PMN-29.5PT remains in a polydomain condition, which exhibits larger D_{33} and ε_r values.

I estimated the composition of the (1-*x*)PMN-*x*PT single crystals with the combination of the source material stoichiometry ratio and an experimental formular of $x=(T_c+10)/5$. However, this is not a very precise quantitative method to determine the compositions, and therefore predicts the stability of the field-induced O-phase in a specific <011> PMN-PT substrate. A more accurate manner in which to identify the stability is to combine the experimental values of T_c, D_{33} and ε_r for identical smaller crystals sliced from the wafer. First, the value of T_c should be within 135-145°C which means that the composition is near PMN-30PT. Second, the value of D_{33} and ε_r should be measured after poling. If D_{33} <400 pC/N and ε_r <1000, then the PMN-PT substrate is in a metastable O-phase with a nonvolatile field-induced strain. Whereas, if D_{33} >1100 pC/N and ε_r >3000, then the PMN-PT substrate will relax to the R-phase and thus have a volatile field-induced strain. In this way, one can select the proper PMN-PT substrates with desirable strain types based on the specific function to be designed.

I have deposited ferromagnetic MCFO thin films on four PMN-30PT and three PMN-29.5PT substrates with proper field-induced strain conditions that have been examined by the method mentioned above. For all the MCFO/PMN-PT heterostructures, I have repeated the measurement of the electric field modulation of the magnetization for four times. The four MCFO/PMN-30PT samples always showed a nonvolatile field-modulation of the magnetization, whereas the three MCFO/PMN-29.5PT ones always showed a volatile field-modulation of the magnetization. Defect dipoles have previously been utilized to tune the stability of the polarization reorientation in $BaTiO_3$ single crystals.[11] I also tried to study such defect effect in our PMN-PT substrates. However, the results showed that both the high temperature annealing (800°C) and quenching (350→20°C) processes could not

change the stability condition of the field-induced O-phase.

[1] Z. Wang, Y. Wang, W. Ge, J. Li, and D. Viehland, Applied Physics Letters **103,** 132909 (2013).
[2] Y. Lu, D. Y. Jeong, Z. Y. Cheng, Q. M. Zhang, H. S. Luo, Z. W. Yin, and D. Viehland, Applied Physics Letters **78,** 3109 (2001).
[3] M. Shanthi, S. M. Chia, and L. C. Lim, Applied Physics Letters **87,** 202902 (2005).
[4] M. Shanthi and L. C. Lim, Applied Physics Letters **95,** 102901 (2009).
[5] Y. P. Guo, H. S. Luo, T. H. He, H. Q. Xu, and Z. W. Yin, Jpn. J. Appl. Phys. **41,** 1451 (2002).
[6] M. Davis, Thesis, Swiss Federal Institute of Technology, 2006.
[7] B. Noheda, D. E. Cox, G. Shirane, J. Gao, and Z. G. Ye, Phys. Rev. B **66,** 054104 (2002).
[8] X. Yao, Z. Chen, and L. E. Cross, Journal of Applied Physics **54,** 3399 (1983).
[9] J. Peng, H. S. Luo, D. Lin, H. Q. Xu, T. H. He, and W. Q. Jin, Applied Physics Letters **85,** 6221 (2004).
[10] M. Shanthi, K. H. Hoe, C. Y. H. Lim, and L. C. Lim, Applied Physics Letters **86,** 262908 (2005).
[11] X. B. Ren, Nature Materials **3,** 91 (2004).

PUBLICATIONS

Journal papers:

1. Wang, ZG; Li, YX; Viswan, R; Hu, BL; Harris, VG; Li, JF; Viehland, D, *ACS Nano*, 7(4), 3447 (2013).

2. Wang, ZG; Wang, YJ; Ge, WW; Li, JF; Viehland, D, *Applied Physics Letters,* 103, 132909(2013).

3. Wang, ZG; Li, YX; Viswan, R; Chen, B; Li, JF; Viehland, D, *Applied Physics Letters,* 101, 132902(2012).

4. Wang, ZG; Viswan, R; Chen, B; Li, JF; Viehland, D, *Journal of Applied Physics,* 111, 034108(2012).

5. Wang, ZG; Viswan, R; Hu, BL; Harris, VG; Li, JF; Viehland, D, *Physica. Status Solidi RRL*, 6(2), 89(2012).

6. Wang, ZG; Viswan, R; Hu, BL; Harris, VG; Li, JF; Viehland, D, *Physica. Status Solidi RRL*, 6(2), 92(2012).

7. Wang, ZG; Yang, YD; Viswan, R; Li, JF; Viehland, D, *Applied Physics Letters,* 99, 043110(2011).

8. Wang, ZG; Yan, L; Yang, YD; Li, JF; Das, J; Geiler, AL, Yang, A; Chen, YJ; Harris, VG; Viehland, D, *Journal of Applied Physics,* 109, 034102(2011).

9. Wang, ZG; Yang, YD; Viswan, R; Li, JF; Viehland, D, *Applied Physics Letters,* 99, 043110(2011).

10. Yang, YD; Wang, ZG; Viswan, R; Li, JF; Viehland, D, *Journal of Nanomaterials,* 756319(2010). (corresponding author)

Book chapter:

1. Wang, ZG; Yang, YD; Viswan, R; Li, JF; and Viehland, D, 'Control of crystallization and ferroelectric properties of BaTiO3 thin films on alloy substrates' Ferroelectrics, 2011, InTech.

REFERENCES

[1] J. Wang, et al., Science **299**, 1719 (2003).
[2] P. Curie, J. Phys. **3**, 393 (1894).
[3] I. E. Dzyaloshinshii, Zh. Eksp. Teor. Fiz. **37**, 881 (1959).
[4] N. A. Hill, J. Phys. Chem. B **104**, 6694 (2000).
[5] N. Hur, S. Park, P. A. Sharma, J. S. Ahn, S. Guha, and S. W. Cheong, Nature **429**, 392 (2004).
[6] T. Kimura, T. Goto, H. Shintani, K. Ishizaka, T. Arima, and Y. Tokura, Nature **426**, 55 (2003).
[7] G. T. Rado and V. J. Folen, Phys. Rev. Lett. **7**, 310 (1961).
[8] D. N. Astrov, Zh. Transl. Soviet. Phys. **11**, 708 (1960).
[9] C. Ederer and N. A. Spaldin, Curr. Opin. Solid State Mater. Sci. **9**, 128 (2005).
[10] J. P. Rivera and H. Schmid, J. Appl. Phys. **70**, 6410 (1991).
[11] H. Wiegelmann, A. A. Stepanov, I. M. Vitebsky, A. G. M. Jansen, and P. Wyder, Phys. Rev. B **49**, 10039 (1994).
[12] A. M. Kadomtseva, A. K. Zvezdin, Y. F. Popov, A. P. Pyatakov, and G. P. Vorob'ev, Jetp Letters **79**, 571 (2004).
[13] Z. J. Huang, Y. Cao, Y. Y. Sun, Y. Y. Xue, and C. W. Chu, Phys. Rev. B **56**, 2623 (1997).
[14] Y. Yang, J. M. Liu, H. B. Huang, W. Q. Zou, P. Bao, and Z. G. Liu, Phys. Rev. B **70**, 132101 (2004).
[15] M. I. Bichurin, V. M. Petrov, Y. V. Kiliba, and G. Srinivasan, Physical Review B **66**, 134404 (2002).
[16] G. Srinivasan, in *Annual Review of Materials Research, Vol 40*, edited by D. R. Clarke, M. Ruhle and F. Zok, 2010), Vol. 40, p. 153.
[17] S. Dong, J. Zhai, F. Bai, J. F. Li, and D. Viehland, Appl. Phys. Lett. **87**, 062502 (2005).
[18] S. X. Dong, J. F. Li, and D. Viehland, Appl. Phys. Lett. **85**, 5305 (2004).
[19] S. X. Dong, J. R. Cheng, J. F. Li, and D. Viehland, Appl. Phys. Lett. **83**, 4812 (2003).
[20] S. X. Dong, J. F. Li, and D. Viehland, Appl. Phys. Lett. **83**, 2265 (2003).
[21] M. Liu, X. Li, J. Lou, S. Zheng, K. Du, and N. X. Sun, J. Appl. Phys. **102**, 083911 (2007).
[22] J. G. Wan, X. W. Wang, Y. J. Wu, M. Zeng, Y. Wang, H. Jiang, W. Q. Zhou, G. H. Wang, and J. M. Liu, Appl. Phys. Lett. **86**, 122501 (2005).
[23] X. L. Zhong, J. B. Wang, M. Liao, G. J. Huang, S. H. Xie, Y. C. Zhou, Y. Qiao, and J. P. He, Appl. Phys. Lett. **90**, 152903 (2007).
[24] H. Ryu, et al., Appl. Phys. Lett. **89**, 102907 (2006).
[25] S. Ren and M. Wuttig, Appl. Phys. Lett. **92**, 083502 (2008).
[26] K. S. Chang, et al., Appl. Phys. Lett. **84**, 3091 (2004).
[27] C. Deng, Y. Zhang, J. Ma, Y. Lin, and C.-W. Nana, J. Appl. Phys. **102**, 074114 (2007).
[28] M. Murakami, et al., Appl. Phys. Lett. **87**, 112901 (2005).
[29] S. Ryu, J. H. Park, and H. M. Jang, Appl. Phys. Lett. **91**, 142910 (2007).

[30] M. Ziese, A. Bollero, I. Panagiotopoulos, and N. Moutis, Appl. Phys. Lett. **88**, 212502 (2006).
[31] H.-C. He, J. Wang, B.-P. Zhou, and C.-W. Nan, Adv. Funct. Mater. **17**, 1333 (2007).
[32] H.-C. He, J.-P. Zhou, J. Wang, and C.-W. Nan, Appl. Phys. Lett. **89**, 052904 (2006).
[33] H. Zheng, Q. Zhan, F. Zavaliche, M. Sherburne, F. Straub, M. P. Cruz, L.-Q. Chen, U. Dahmen, and R. Ramesh, Nano Lett. **6**, 1401 (2006).
[34] H. Zheng, F. Straub, Q. Zhan, P.-L. Yang, W.-K. Hsieh, F. Zavaliche, Y.-H. Chu, U. Dahmen, and R. Ramesh, Adv. Mater. **18**, 2747 (2006).
[35] F. Zavaliche, T. Zhao, H. Zheng, F. Straub, M. P. Cruz, P. L. Yang, D. Hao, and R. Ramesh, Nano Lett. **7**, 1586 (2007).
[36] F. Zavaliche, et al., Nano Letters **5**, 1793 (2005).
[37] I. Levin, J. Li, J. Slutsker, and A. L. Roytburd, Adv. Mater. **18**, 2044 (2006).
[38] J. Slutsker, Z. Tan, A. L. Roytburd, and I. Levin, J. Mater. Res. **22**, 2087 (2007).
[39] Y.-H. Chu, et al., Nat. Mater. **7**, 478 (2008).
[40] S. M. Wu, S. A. Cybart, P. Yu, M. D. Rossell, J. X. Zhang, R. Ramesh, and R. C. Dynes, Nat. Mater. **9**, 756 (2010).
[41] V. Laukhin, et al., Phys. Rev. Lett. **97**, 227201 (2006).
[42] J.-M. Hu, G. Sheng, J. X. Zhang, C. W. Nan, and L. Q. Chen, Appl. Phys. Lett. **98**, 112505 (2011).
[43] W. Eerenstein, M. Wiora, J. L. Prieto, J. F. Scott, and N. D. Mathur, Nat. Mater. **6**, 348 (2007).
[44] C.-W. Nan, G. Liu, Y. Lin, and H. Chen, Phys. Rev. Lett. **94**, 197203 (2005).
[45] E. Bousquet, M. Dawber, N. Stucki, C. Lichtensteiger, P. Hermet, S. Gariglio, J.-M. Triscone, and P. Ghosez, Nature **452**, 732 (2008).
[46] G. Logvenov, A. Gozar, and I. Bozovic, Science **326**, 699 (2009).
[47] H. Yamada, Y. Ogawa, Y. Ishii, H. Sato, M. Kawasaki, H. Akoh, and Y. Tokura, Science **305**, 646 (2004).
[48] A. Ohtomo and H. Y. Hwang, Nature **427**, 423 (2004).
[49] J. L. MaCmanus-Driscoll, P. Zerrer, H. Wang, H. Yang, J. Yoon, A. Fouchet, R. Yu, M. G. Blamire, and Q. Jia, Nat. Mater. **7**, 314 (2008).
[50] S. M. O'Malley, et al., Physical Review B **78**, 165424 (2008).
[51] R. Ramesh and N. A. Spaldin, Nat. Mater. **6**, 21 (2007).
[52] J. Das, Y.-Y. Song, N. Mo, P. Krivosik, and C. E. Patton, Adv. Mater. **21**, 2045 (2009).
[53] H. Zheng, et al., Science **303**, 661 (2004).
[54] S. Dong, J. Zhai, J. Li, and D. Viehland, Appl. Phys. Lett. **89**, 252904 (2006).
[55] J. Zhai, J. Li, D. Viehland, and M. I. Bichurin, J. Appl. Phys. **101**, 014102 (2007).
[56] J. Zhai, Z. Xing, S. Dong, J. Li, and D. Viehland, J. Am. Ceram. Soc. **91**, 351 (2008).
[57] N. A. Pertsev, Phys. Rev. B **78**, 212102 (2008).
[58] J.-M. Hu and C. W. Nan, Phys. Rev. B **80**, 224416 (2009).
[59] T. Wu, A. Bur, K. Wong, J. L. Hockel, C.-J. Hsu, H. K. D. Kim, K. L. Wang, and G. P. Carman, J. Appl. Phys. **109**, 07D732 (2011).
[60] J. M. Hu, Z. Li, L. Q. Chen, and C. W. Nan, Adv. Mater. **24**, 2869 (2012).
[61] Z. Wang, Y. Yang, R. Viswan, J. Li, and D. Viehland, Appl. Phys. Lett. **99**, 043110 (2011).
[62] Z. Wang, R. Viswan, B. Hu, J.-F. Li, V. G. Harris, and D. Viehland, J. Appl. Phys. **111**, 034108 (2012).

[63] M. Liu, et al., Adv. Funct. Mater. **19**, 1826 (2009).
[64] J. Lou, M. Liu, D. Reed, Y. Ren, and N. X. Sun, Adv. Mater. **21**, 4711 (2009).
[65] J.-M. Hu, Z. Li, L.-Q. Chen, and C.-W. Nan, Nat. Commun. **2**, 553 (2011).
[66] X. B. Ren, Nat. Mater. **3**, 91 (2004).
[67] S. E. Park and T. R. Shrout, J. Appl. Phys. **82**, 1804 (1997).
[68] C. Thiele, K. Dorr, S. Fahler, L. Schultz, D. C. Meyer, A. A. Levin, and P. Paufler, Appl. Phys. Lett. **87**, 262502 (2005).
[69] J. J. Yang, Y. G. Zhao, H. F. Tian, L. B. Luo, H. Y. Zhang, Y. J. He, and H. S. Luo, Appl. Phys. Lett. **94**, 212504 (2009).
[70] J. A. Paulsen, A. P. Ring, C. C. H. Lo, J. E. Snyder, and D. C. Jiles, J. Appl. Phys. **97**, 044502 (2005).
[71] C. H. Kim, Y. Myung, Y. J. Cho, H. S. Kim, S.-H. Park, J. Park, J.-Y. Kim, and B. Kim, J. Phys. Chem. C **113**, 7085 (2009).
[72] H. X. Fu and R. E. Cohen, Nature **403**, 281 (2000).
[73] F. Li, S. J. Zhang, Z. Xu, X. Y. Wei, and T. R. Shrout, Adv. Funct. Mater. **21**, 2118 (2011).
[74] B. Noheda, D. E. Cox, G. Shirane, J. Gao, and Z. G. Ye, Phys. Rev. B **66**, 054104 (2002).
[75] M. Shanthi and L. C. Lim, Appl. Phys. Lett. **95**, 102901 (2009).
[76] L. H. Luo, H. X. Wang, Y. X. Tang, X. Y. Zhao, Z. Y. Feng, D. Lin, and H. S. Luo, J. Appl. Phys. **99**, 024104 (2006).
[77] Y. P. Guo, H. S. Luo, T. H. He, H. Q. Xu, and Z. W. Yin, Jpn. J. Appl. Phys. **41**, 1451 (2002).
[78] Y. Lu, D. Y. Jeong, Z. Y. Cheng, Q. M. Zhang, H. S. Luo, Z. W. Yin, and D. Viehland, Appl. Phys. Lett. **78**, 3109 (2001).
[79] S. Zhang, N. P. Sherlock, R. J. Meyer, Jr., and T. R. Shrout, Appl. Phys. Lett. **94**, 162906 (2009).
[80] J. Peng, H. S. Luo, D. Lin, H. Q. Xu, T. H. He, and W. Q. Jin, Appl. Phys. Lett. **85**, 6221 (2004).
[81] D. Viehland, J. F. Li, and A. Amin, J. Appl. Phys. **92**, 3985 (2002).
[82] Z. Wang, Y. Li, R. Viswan, B. Hu, V. G. Harris, J. Li, and D. Viehland, ACS Nano **7**, 3447 (2013).
[83] X. Gao, L. Liu, B. Birajdar, M. Ziese, W. Lee, M. Alexe, and D. Hesse, Adv. Funct. Mater. **19**, 3450 (2009).
[84] D.-H. Kim, D. E. Nikles, D. T. Johnson, and C. S. Brazel, Journal of Magnetism and Magnetic Materials **320**, 2390 (2008).
[85] S. D. Bader, Rev. Mod. Phys. **78**, 1 (2006).
[86] S. H. Sun, H. Zeng, D. B. Robinson, S. Raoux, P. M. Rice, S. X. Wang, and G. X. Li, J. Am. Chem. Soc. **126**, 273 (2004).
[87] P. Oswald, O. Clement, C. Chambon, E. SchoumanClaeys, and G. Frija, Magnetic Resonance Imaging **15**, 1025 (1997).
[88] K. Raj and R. Moskowitz, J. Magn. Magn. Mater. **85**, 233 (1990).
[89] A. Hutlova, D. Niznansky, J. L. Rehspringer, C. Estournes, and M. Kurmoo, Adv. Mater. **15**, 1622 (2003).
[90] L. Zhu, S. Nie, K. Meng, D. Pan, J. Zhao, and H. Zheng, Adv. Mater. **24**, 4547 (2012).
[91] M. H. Kryder, E. C. Gage, T. W. McDaniel, W. A. Challener, R. E. Rottmayer, G. Ju, Y.-T. Hsia, and M. F. Erden, Proc. IEEE **96**, 1810 (2008).
[92] W. A. Challener, et al., Nature Photon. **3**, 220 (2009).
[93] L. J. Swartzendruber, G. E. Hicho, H. D. Chopra, S. D. Leigh, G. Adam, and E.

Tsory, J. Appl. Phys. **81**, 4263 (1997).
[94] J. Wang, J. Ma, Z. Li, Y. Shen, Y. Lin, and C. W. Nan, J. Appl. Phys. **110**, 043919 (2011).
[95] R. F. L. Evans, R. W. Chantrell, U. Nowak, A. Lyberatos, and H. J. Richter, Appl. Phys. Lett. **100**, 102402 (2012).
[96] B. X. Xu, Z. J. Liu, R. Ji, Y. T. Toh, J. F. Hu, J. M. Li, J. Zhang, K. D. Ye, and C. W. Chia, J. Appl. Phys. **111**, 07B701 (2012).
[97] A. E. Renault, H. Dammak, G. Calvarin, P. Gaucher, and M. P. Thi, J. Appl. Phys. **97**, 044105 (2005).
[98] D. J. Franzbach, Y. J. Gu, L. Q. Chen, and K. G. Webber, Appl. Phys. Lett. **101**, 232904 (2012).
[99] Z. Wang, Y. Wang, W. Ge, J. Li, and D. Viehland, Appl. Phys. Lett. **103**, 132909 (2013).
[100] D. Viehland and J. F. Li, J. Appl. Phys. **92**, 7690 (2002).
[101] Y. Kadota and T. Morita, Jpn. J. Appl. Phys. **51**, 09LE08 (2012).
[102] Y. Kadota, H. Hosaka, and T. Morita, J. Korean Phys. Soc. **57**, 902 (2010).
[103] A. Benayad, G. Sebald, L. Lebrun, B. Guiffard, S. Pruvost, D. Guyomar, and L. Beylat, Mater. Res. Bull. **41**, 1069 (2006).
[104] Z. Wang, et al., J. Appl. Phys. **109**, 034102 (2011).
[105] J. Y. Li and D. Liu, J. Mech. Phys. Solids **52**, 1719 (2004).
[106] G. Catalan, et al., Nat. Mater. **10**, 963 (2011).
[107] F. M. Bai, J. F. Li, and D. Viehland, J. Appl. Phys. **97**, 054103 (2005).
[108] G. Xu, G. Shirane, J. R. D. Copley, and P. M. Gehring, Phys. Rev. B **69**, 064112 (2004).
[109] M. Liu, O. Obi, Z. Cai, J. Lou, G. Yang, K. S. Ziemer, and N. X. Sun, J. Appl. Phys. **107**, 073916 (2010).
[110] S. Gepraegs, A. Brandlmaier, M. Opel, R. Gross, and S. T. B. Goennenwein, Appl. Phys. Lett. **96**, 142509 (2010).
[111] M. Liu, O. Obi, J. Lou, S. Li, X. Xing, G. Yang, and N. X. Sun, J. Appl. Phys. **109**, 07D913 (2011).
[112] T. Wu, A. Bur, P. Zhao, K. P. Mohanchandra, K. Wong, K. L. Wang, C. S. Lynch, and G. P. Carman, Appl. Phys. Lett. **98**, 012504 (2011).
[113] S. Sahoo, S. Polisetty, C. G. Duan, S. S. Jaswal, E. Y. Tsymbal, and C. Binek, Phys. Rev. B **76**, 092108 (2007).
[114] C. Thiele, K. Dörr, O. Bilani, J. Rödel, and L. Schultz, Physical Review B **75**, 054408 (2007).
[115] L. J. McGilly, A. Schilling, and J. M. Gregg, Nano Letters **10**, 4200 (2010).
[116] D. Y. He, L. J. Qiao, A. A. Volinsky, Y. Bai, and L. Q. Guo, Physical Review B **84**, 024101 (2011).
[117] K. Shikada, M. Ohtake, F. Kirino, and M. Futamoto, J. Appl. Phys. **105**, 07C303 (2009).
[118] H. Zheng, J. Kreisel, Y.-H. Chu, R. Ramesh, and L. Salamanca-Riba, Appl. Phys. Lett. **90**, 113113 (2007).
[119] R. Fischer, T. Schrefl, H. Kronmuller, and J. Fidler, Journal of Magnetism and Magnetic Materials **153**, 35 (1996).
[120] J. I. Park, N. J. Kang, Y. W. Jun, S. J. Oh, H. C. Ri, and J. Cheon, ChemPhysChem **3**, 543 (2002).
[121] Y. W. Jun, et al., Journal of the American Chemical Society **127**, 5732 (2005).
[122] L. Yan, F. Bai, J. Li, and D. Viehland, Journal of the American Ceramic Society **92**, 17 (2009).

[123] B. D. Cullity and C. D. Graham, in *Introduction to Magnetic Materials, 2nd Edition* (Wiley-IEEE Press, 2008).
[124] G. Herzer, IEEE Trans. Magn. **26**, 1397 (1990).
[125] H. Kronmüller, R. Fischer, M. Seeger, and A. Zern, J. Phys. D-Appl. Phys. **29**, 2274 (1996).
[126] R. Grössinger and M. Dahlgren, Physica B **246**, 213 (1998).
[127] R. L. White, R. M. H. New, and R. F. W. Pease, IEEE Trans. Magn. **33**, 990 (1997).
[128] Z. Wang, R. Viswan, B. Hu, V. G. Harris, J.-F. Li, and D. Viehland, Phys. Status Solidi RRL **6**, 92 (2012).
[129] Y. Suzuki, H. Y. Hwang, S. W. Cheong, and R. B. vanDover, Appl. Phys. Lett. **71**, 140 (1997).
[130] T. K. Nath, R. A. Rao, D. Lavric, C. B. Eom, L. Wu, and F. Tsui, Appl. Phys. Lett. **74**, 1615 (1999).
[131] L. Ranno, A. Llobet, R. Tiron, and E. Favre-Nicolin, Appl. Surf. Sci. **188**, 170 (2002).
[132] M. Angeloni, G. Balestrino, N. G. Boggio, P. G. Medaglia, P. Orgiani, and A. Tebano, J. Appl. Phys. **96**, 6387 (2004).
[133] H. L. Liu, M. X. Kuo, J. L. Her, K. S. Lu, S. M. Weng, L. M. Wang, S. L. Cheng, and J. G. Lin, J. Appl. Phys. **97**, 113528 (2005).
[134] C. M. Xiong, J. R. Sun, and B. G. Shen, Solid State Commun. **134**, 465 (2005).
[135] I. C. Infante, D. Hrabovský, V. Laukhin, F. Sánchez, and J. Fontcuberta, J. Appl. Phys. **99**, 08C503 (2006).
[136] S. E. E. Park and W. Hackenberger, Curr. Opin. Solid State Mater. Sci. **6**, 11 (2002).
[137] S. X. Dong, J. Y. Zhai, Z. P. Xing, J. F. Li, and D. Viehland, Appl. Phys. Lett. **86**, 102901 (2005).
[138] Z. Xing, J. Zhai, J. Gao, J. Li, and D. Viehland, IEEE Electron Device Letters **30**, 445 (2009).
[139] J. Das, J. Gao, Z. Xing, J. F. Li, and D. Viehland, Appl. Phys. Lett. **95**, 092501 (2009).
[140] P. Zhao, Z. Zhao, D. Hunter, R. Suchoski, C. Gao, S. Mathews, M. Wuttig, and I. Takeuchi, Appl. Phys. Lett. **94**, 243507 (2009).
[141] T. Brintlinger, et al., Nano Lett. **10**, 1219 (2010).
[142] A. E. Clark, M. Wun-Fogle, J. B. Restorff, T. A. Lograsso, and J. R. Cullen, IEEE Trans. Magn. **37**, 2678 (2001).
[143] M. B. Moffett, A. E. Clark, M. Wunfogle, J. Linberg, J. P. Teter, and E. A. McLaughlin, J. Acoust. Soc. Am. **89**, 1448 (1991).
[144] C. C. Wong, H. I. Smith, and C. V. Thompson, Appl. Phys. Lett. **48**, 335 (1986).
[145] J. Schwarzkopf and R. Fornari, Prog. Cryst. Growth Charact. Mater. **52**, 159 (2006).
[146] Y. W. Cho, S. K. Choi, and G. V. Rao, Appl. Phys. Lett. **86**, 202905 (2005).
[147] B. Dkhil, E. Defay, and J. Guillan, Appl. Phys. Lett. **90**, 022908 (2007).
[148] W. Pompe, X. Gong, Z. Suo, and J. S. Speck, J. Appl. Phys. **74**, 6012 (1993).
[149] Y. Yang, J. Yao, J. Li, J. Das, and D. Viehland, Thin Solid Films **518**, 5806 (2010).
[150] L. Yan, Z. Xing, Z. Wang, T. Wang, G. Lei, J. Li, and D. Viehland, Appl. Phys. Lett. **94**, 192902 (2009).
[151] X. J. Lou, J. Appl. Phys. **105**, 024101 (2009).
[152] S. M. Yang, T. H. Kim, J.-G. Yoon, and T. W. Noh, Adv. Funct. Mater. **22**, 2310

(2012).
153 T. Kala, Phase Transitions **36**, 65 (1991).
154 R. N. Torah, S. P. Beeby, and N. M. White, J. Phys. D-Appl. Phys. **37**, 1074 (2004).
155 N. Srisukhumbowornchai and S. Guruswamy, J. Appl. Phys. **92**, 5371 (2002).
156 W. Pompe, X. Gong, Z. Suo, and J. S. Speck, J. Appl. Phys. **74**, 6012 (1993).
157 S. A. Harrington, et al., Nat. Nanotechnol. **6**, 491 (2011).
158 M. Alexe, G. Kastner, D. Hesse, and U. Gosele, Appl. Phys. Lett. **70**, 3416 (1997).
159 T. Mokari, C. G. Sztrum, A. Salant, E. Rabani, and U. Banin, Nat. Mater. **4**, 855 (2005).
160 C. Yan, L. Nikolova, A. Dadvand, C. Harnagea, A. Sarkissian, D. F. Perepichka, D. Xue, and F. Rosei, Adv. Mater. **22**, 1741 (2010).
161 M. Tyunina and J. Levoska, Appl. Phys. Lett. **95**, 102903 (2009).
162 J. Sikula, J. Hlavka, V. Sedlakova, and L. Grmela, Proc. 24th Annu. Capacitor Resistor Technol. Symp., 141 (2004).
163 X. Fang and T. Kobayashi, Appl. Phys. A Mater. Sci. **69**, S587 (1999).
164 Y. Hikita, Y. Kozuka, T. Susaki, H. Takagi, and H. Y. Hwang, Appl. Phys. Lett. **90**, 143507 (2007).
165 C. H. Ahn, R. H. Hammond, T. H. Geballe, M. R. Beasley, J. M. Triscone, M. Decroux, O. Fischer, L. Antognazza, and K. Char, Appl. Phys. Lett. **70**, 206 (1997).